PRESERVATION OF TRANSPORT PROPERTIES TRENDS:

COMPUTATIONAL ROCK PHYSICS APPROACH

A DISSERTATION

SUBMITTED TO THE DEPARTMENT OF GEOPHYSICS

AND THE COMMITTEE ON GRADUATE STUDIES

OF STANFORD UNIVERSITY

IN PARTIAL FULFILLMENT OF THE REQUIREMENTS

FOR THE DEGREE OF

DOCTOR OF PHILOSOPHY

Richa

August 2010

Abstract

In recent years, computational rock physics has gained reliability in predicting the properties of rocks, mostly due to the use of advanced imaging and computing techniques. We believe that now computational rock physics can be used to produce useful data and understand relations among rock properties, similar to lab and log data. Computational rock physics is a rapidly evolving field and as such requires careful quantitative analysis of the components of this technology: resolution, digital sample size, thresholding of the image, as well as the effects of the scale of the computational simulation.

Here we address these issues by utilizing various mathematical and statistical techniques. We begin with the traditional concepts of representative elementary volume (REV), finest resolution, optimal thresholding; and establish the transport properties trends at these conventional settings and utilize them as the base case. We then examine the transport properties trends, specifically, porosity-permeability and porosity-formation factor, in the conditions that are not optimal by traditional standards. Particularly, we explore the transport properties trends for the sample sizes

smaller than the REV, for resolutions coarser than the technically achievable resolution and for the binary images obtained using thresholds far from their optimal threshold.

We find that in these unconventional situations, the computed values of, e.g., porosity, permeability, and formation factor, diverges from those computed on optimally produced digital rock as well as from laboratory results. However, the trends between rock properties computed on these non-optimally generated samples often form trends that favorably match laboratory trends and, as a result, are of practical value. These results imply that, we can obtain physically meaningful trend from these non-optimally generated samples. This means that we can produce the transport properties trends using a small fragment of rock instead of multiple physical samples required for producing these trends using traditional laboratory methods.

However, our analysis is not exhaustive. For example, our range of sample sizes varies only from core scale to micro-pore structure. Also, the samples used in this study are fairly homogeneous sandstones. It will be interesting to extend this study beyond the scales studied here and for more varied samples. However, these analyses are beyond the scope of this thesis.

Acknowledgements

all through my PhD, listening to my complaints and frustrations, and also believing in me.

Last but not least, I deeply thank my family, my parents, Dr. Ram Phal Ram and Sudha Rani; my brother Neeraj, my sister-in-law Chanda and my nephew Sparsh Kushwaha for all their unconditional emotional support and encouragement. The inspiration to pursue a PhD was given to me by my father while the constant push to chase that dream came from my brother. They taught me how to hit the ground running and never give up. My mother's perfectionist and never-stop-learning attitude inspired me to seek knowledge and that curiosity has helped me all through my research career. This accomplishment would not be possible without my family's support.

Table of Contents

List of Figures

List of Tables

Chapter 1
Introduction

"The use of simulation is an activity that is as natural as a child who role plays with toy objects. To understand reality and all of its complexity, we must build artificial objects and dynamically act out roles with them. Computer simulation is the electronic equivalent of this type of role playing." - Fishwick

1.1 BACKGROUND

Transport properties of porous media, including the transport of electrical current and viscous fluid, are a subject of wide interest in science and technology. A detailed knowledge of the transport properties of fluids through porous media is critical for the successful design, preparation, and application of adsorbents and membranes in many industrial as well as for environmental processes that cover a very broad range of specialties: geology, engineering, chemistry, and physics. (Wernert et al., 2010). They are also extremely useful properties in geophysics, especially in pollution migration, CO_2 sequestration, ground water management, nuclear repositories, hydrothermal systems and petroleum reservoirs.

Historically, the research in the field of transport properties has been focused on relating these properties to a wide range of rock properties, such as porosity (Carman, 1937; Archie 1942; Berg, 1970, Bloch, 1991), grain size or grain size distribution (Krumbein and Monk, 1942; Chilingar, 1964; Berg 1970; Beard and Weyl, 1973; van Baaren, 1979; Iverson and Satchwell, 1989), mineralogical composition (Marion et al., 1989; Ahmed et al., 1991), clay content (Baptist and Sweeney, 1954; Waxman and Smits, 1968; Clavier, Coates and Dumanoir, 1977; Sen and Goode, 1988; Revil and Glover, 1998), salinities (Baptist and Sweeney, 1954; Keller 1966, Chang et al.., 1983), temperature (Keller and Frischknecht,1966; Matthess, 1982; Hem, 1985; Sorensen and Glass, 1987; Clesceri et al., 1998;) and surface area of the grain space (Carman, 1937; Johnson et al., 1987; Sheng and Zhou, 1988; Schwartz and Banvar, 1989). Several investigators related these transport properties to the statistical properties of pore or grain (Prager, 1961; Berryman and Blair, 1986; Rubinstein and Torquato, 1989; Adler et al., 1990) while others related them to geometrical attributes of the pore space in thin sections (Koplik et al., 1984; Doyen, 1988; McCresh et al., 1988). Lastly, capillary pressure data has been related to transport properties (Payatakes et al., 1973; Dullien, 1979; Swanson, 1981; Thomeer, 1983; Katz and Thompson, 1986; Constantinides and Payatakes, 1989). The transport properties relationships with different rock properties mentioned here were derived either empirically or by replacing the actual system with some sort of model, such as a system of interconnected capillaries (permeability) or a network of resistor (electrical conductivity). While this simplification provides an approximate trend and provides

an understanding of general properties trends, it ignores the complex geometry of porous media which limits the accuracy of these results.

1.2 COMPUTATIONAL ROCK PHYSICS

With recent development in technology, it is now possible to reconstruct a realistic 3D digital rock image with complex pore microstructure and mathematically calculate its transport properties. The absolute and relative permeability can be accurately calculated using numerical methods such as Lattice-Boltzmann and network modeling (Auzerais et al., 1996; Bakke and Oren, 1997; O'Connor and Fredrich, 1999; and Keehm, 2003). The electrical conductivity, on the other hand, can be calculated by using finite element method (Martyrs and Garboczi, 1992; Arns et al., 2001).

A 3D digital rock model can be reconstructed by three different methods: (a) Granular scale modeling, (b) 3D geostaitstical reconstruction of 2D thin-section or SEM images, and (c) CT-scan of a small rock fragment.

The first method, granular dynamic simulation involves simulating the grains in the reservoir and then mathematically subjecting them to different geological conditions such as compaction and diagenesis, (Cundall and Strack, 1979; Jin et al., 2004). The advantage of using a granular dynamic simulation is that we have complete control over the geological conditioning as well as the size and shape of the grains. This helps in making a correlation between rock properties and different geological conditioning. Even though numerically simulating the rock in such a way has its advantage, it still is not an exact replica of a real rock.

The second method involves using a thin section image to mathematically generate the 3D digital binary rock from 2D thin-section of the rock (Keehm, 2003; Kameda, 2005). This entails converting the colored 2D thin section image into 2D binary image and then employing geostatistical simulation to convert this 2D binary image to 3D binary image. This method can provide a way for acquiring a 3D pore structure for the rocks when we do not have any core sample. The third method, involves CT-scanning a small fragment of rock to produce gray scale 3D intensity image (Dunsmuir et al., 1991, Spanne et al., 1994 and Coker et al., 1996) which reflects the density of the sample. This gray scale 3D image is converted to 3D binary image using image classification methods. The third method of CT-scanning the small fragment of rock provides the most accurate representation of the pore microstructure among all the three methods.

In this thesis, we explore different classification methods for converting the thin-section images to binary image but the primary focus of this work is on the 3D digital rocks obtained from the 3D CT-scan of rock samples Although a 3D digital rock obtained using the 3D CT-scan of the rock sample provides an accurate representation of the pore microstructure model, these models are only a few mm in size, while the smallest scale of measurements in Geophysics are laboratory measurements that uses a core plug which is at least few cm in length. A comparison of the trends obtained at the micro-scale using digital rock physics methods to laboratory measurements was performed by Keehm (2003), Kameda (2005), Kameda et al. (2006), Dvorkin (2009), Dvorkin and Nur (2009), and Dvorkin et al. (2009). They found them to correlate fairly well.

In this thesis, we expand their work by first defining the traditional representative elementary volume (REV) (Bear, 1988; Keehm, 2003) and calculating the transport properties at this scale. We then progressively reduce the sample size further until there is no pore connectivity in the sample. We calculate the transport properties at each step. We compare the transport properties trends hence obtained to the laboratory measured trends as well as the theoretical relations and found them in good agreement.

In this dissertation, we also explore the change in the transport properties trends with threshold used to create 3D binary image from 3D gray scale CT-scan data of sandstones and the resolution of the binary image. With change in threshold, the transport properties trends remain stable. Moreover, we find that the change in the geometry of the binary images with change in threshold closely resembles diagenetic quartz overgrowth for the selected sandstone samples. The change in resolution, on the hand, changes the surface area of the samples. This results in change in permeability of the sample, while porosity remains constant. We also observe a slight change in electrical formation factor as we change the resolution. However, all these changes, both in permeability and formation factor, are small and remain within the scatter of the data.

1.3 CHAPTER DESCRIPTION

The following is a brief description of each chapter in this dissertation.

Chapter 2 compares five different image classification methods for classifying the thin-section images to obtain the binary image and porosity. The image

classifications discussed in this chapter are fairly subjective. Hence, we also discuss different sources of errors involved.

Chapter 3 compares five different image classification methods for classifying CT-scan images to obtain 3D binary cube. It also describes various data samples, and their image preprocessing, that are used in Chapter 4, 5 and 6.

Chapter 4 explores the effect of change in sample size as it decreases below traditional REV on the transport properties, in particular their trends. It also discusses a method to decrease the variability in the case of smallest sample size in order to produce a tighter trend that matches laboratory trend.

Chapter 5 examines the effect of threshold used for the image classification on the transport properties and their trends. We also compare the change in the geometry of the binary images obtained at different thresholds to the thin-sections of sandstone samples as well as some theoretical work on diagenetic geometry (Keehm, 2003).

Chapter 6 examines the effect of resolution of binary image on the transport properties and their trends.

Chapter 2

Comparing Classification Techniques for Thin-Section Images

2.1 ABSTRACT

Porosity and binary images of colored thin-section images, used for geostatistically simulating 3D digital rock, can be obtained by using classification methods that classify image pixels into pore pixels and grain pixels. We compare four different classification methods on three different thin-section images. The classification of thin-section images involves identifying blue colored pore pixels (due to blue epoxy) in the image. As colors are quantitatively defined using color-spaces, we employ two different color-spaces, RGB and HSV, to define the blue color pixels for these classification methods. The four classification methods are evaluated based on two criteria: (a) porosity matching, which involves comparing the porosities calculated by classification methods to the porosity obtained from the Glagolev-Chayes point-counting method, and (b) classification error which involves selecting a

few known grain and pore pixels from thin-section and evaluating if they were correctly classified by the classification methods. Using the above two criteria, examining a thin-section in the RGB color-space, in general, gives better results than doing this in the HSV color-space. The discriminant analysis method performs better than the other methods. However, the performance of the different types of discriminant analysis methods varies from sample to sample. The diag-quadratic discriminant analysis gives the best result even though it does not always give the least error for all three samples but it is the only method that gives low error in all the cases. Since the type of discriminant analysis method with least error varies from sample to sample, therefore we recommend that in order to obtain the binary image and porosity from a thin-section image, we should apply all the discriminant analysis method to the sample and evaluate their performance on the basis of second criterion. The second criterion is easier to implement than the first one, which is fairly operator dependent and ambiguous. By using the second criterion we experience fewer errors than by using the first one. All the methods examined here, except multi-component thresholding are fairly subjective and operator dependent. Hence, we also discuss the possible sources of error associated with each method.

2.2 INTRODUCTION

In this chapter we examine different image classification techniques for converting a colored thin-section image to a binary image of pores and grains and possible sources of errors associated with them. The classification of a colored thin-section image is a crucial step in statistically generating a realistic 3D binary digital

rock volume from thin-section images (Keehm, 2003), which in turn affects the rock properties computed on the 3D digital binary rock thus obtained. A classification procedure provides us with two critical pieces of information that are used as input for statistical conversion of 2D image to 3D volume: 2D porosity and the binary training image.

The thin-sections are often prepared by epoxy impregnation, which gives the pore space a blue color (Figure 2.1). To convert a colored thin-section image to a binary image, it is necessary to pick out the blue-colored pore pixels in the colored thin-section image. Since the color is such a crucial element here, we explore different color-spaces, which are an abstract mathematical model describing the way colors can be represented as components of numbers. In this chapter, we work with RGB and HSV color-spaces. The RGB color model (Jain, 1989; Gonzalez and Woods, 1992) is an additive color model that defines color in terms of combination of primaries (red, green, and blue), whereas the HSV color-space defines a color in terms of hue (tint of color), saturation (amount of grayness), and value (brightness).
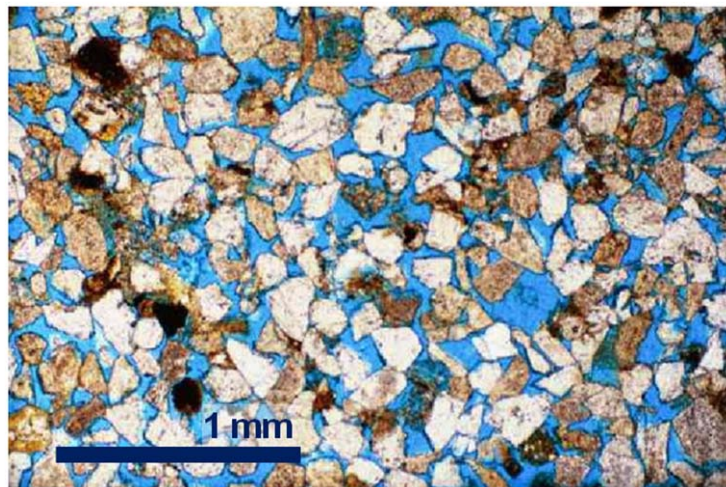
Figure 2.1. Colored thin-section of a rock. The blue color in the image represents the pore space.

In this chapter, we compare RGB and HSV to investigate four classification techniques divided into two groups: threshold-based classification and cluster-based classification.

The threshold based classification for colored images is not straightforward. We can convert the colored image to an intensity image and then obtain a threshold for this intensity image. However, in this case, we do not use all the available information. Instead, if we optimally threshold the histograms of each component in a color-space (e.g. R, G, and B components; or H, S, and V components) and combine the results to obtain a binary image, we can obtain a reasonable classification. We call this method multiple component thresholding.

The cluster based classification involves classifying the pixels into pores and grains using cluster analysis. Cluster-based classification is further divided into two subgroups: (a) supervised learning techniques which utilize training data to classify the groups and (b) unsupervised learning techniques which do not need any training data. Within the supervised learning techniques category, we explore five different types of discriminant analysis method (Hastie, 2001; Krzanowski 1988; Seber, 1984) and a feed-forward back propagating neural network (Bishop, 1995), while in the unsupervised learning technique we examine the K-means cluster analysis (Hastie, 2001; Seber, 1984).

We compare these classification techniques, threshold-based classification and different cluster analysis techniques, using two criteria. The first criterion is to match a physically measured porosity to the digitally derived value (porosity error). The Glagolev-Chayes point-counting method (Galehouse, 1971) is used to obtain the

porosity of the thin-section. Then Van der Plas and Tobi (1965) analysis is used to obtain a 95% confidence interval. If the porosity obtained from the classification technique falls in this range, we consider the technique to be acceptable.

The second criterion involves *a priori* classifying a few pixels in the thin-section image as pore or grain pixels based on visual examination of the image and then comparing these pre-classified pixels to the classification obtained from different classification techniques. The classification error of the classification technique is defined as the number of pixels classified incorrectly.

Overall, using the RGB color-space gives better results than using the HSV color-space. Discriminant analysis methods perform better than other methods but the results for different types of discriminant analysis method vary from sample to sample. The results of all the other methods also vary from sample to sample. This can be attributed to the fact that all the methods except multi-component thresholding are subjective and require operator input. These sources of error and their effect on the output associated with each method are also discussed in this chapter.

The rest of the chapter is structured as follows. In section 2.3, we detail the four classification methods under examination. In section 2.4, we present the results comparing different classification techniques based on the two criteria described above for different thin-sections. In section 2.5, we discuss the possible sources of errors for the classification methods. In section 2.6, we present our conclusions. Finally, Appendix A provides the details of the implementation of the Glagolev-Chayes point-counting method for the various thin-sections used in this chapter.

2.3 CLASSIFICATION METHODS

We use three different thin-section images in our analysis (Figure 2.2) to analyze four different classification methods.
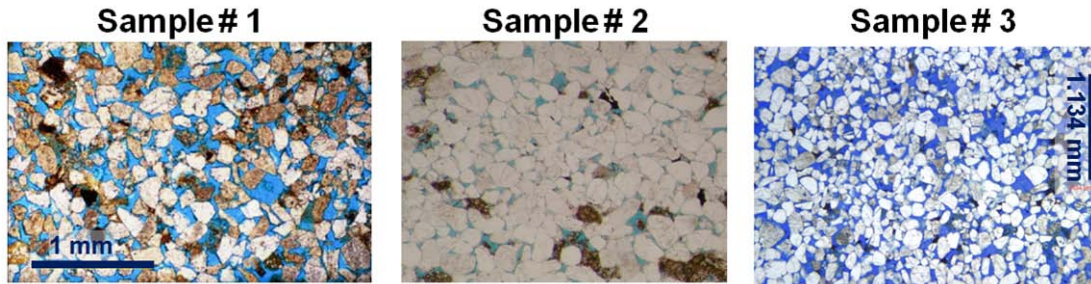
Figure 2.2. The three thin-section images used for comparing classification techniques. Sample 1 is the same as the thin-section shown in Figure 2.1

As discussed earlier, the four classification methods are divided into two groups: threshold based classification and cluster based classification. The following section describes the methods in detail.

2.3.1 Threshold-based classification

As discussed in section 2.2, the colors in an image are expressed using components of the color model, e.g. R, G, and B components; or H, S, and V components. Hence, we have three histograms associated with a colored thin-section image, one corresponding to each component, in a particular color-space. Figures 2.3 and 2.4 show the intensity image of the three R, G, and B components; and H, S, and V components for a colored thin-section (Sample 1) and the corresponding intensity histograms of each component.
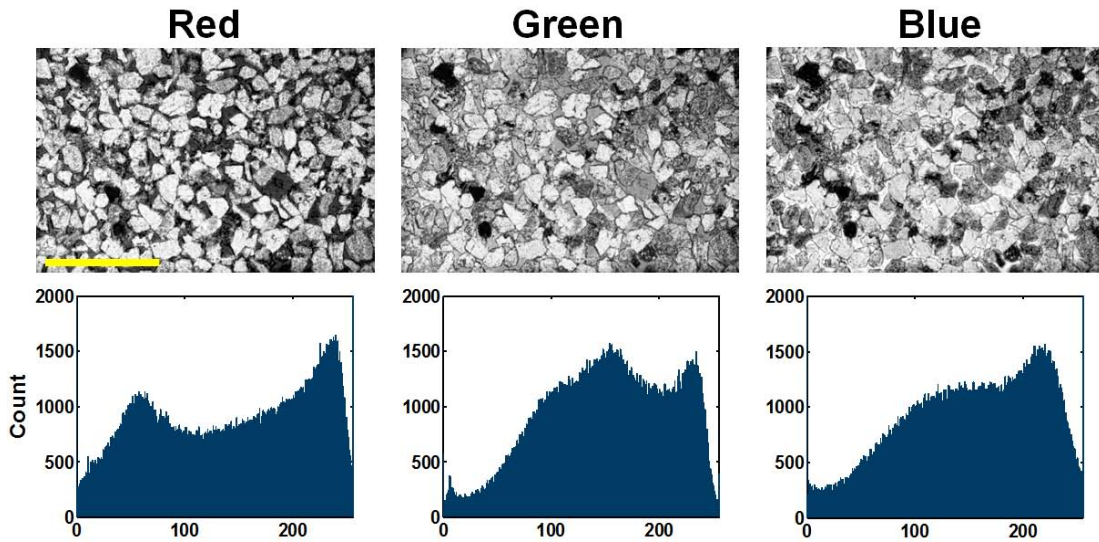
Red **Green** **Blue**

Figure 2.3. The red, green, and blue components of the colored RGB image for Sample 1 with corresponding histograms.

Hue **Saturation** **Value**
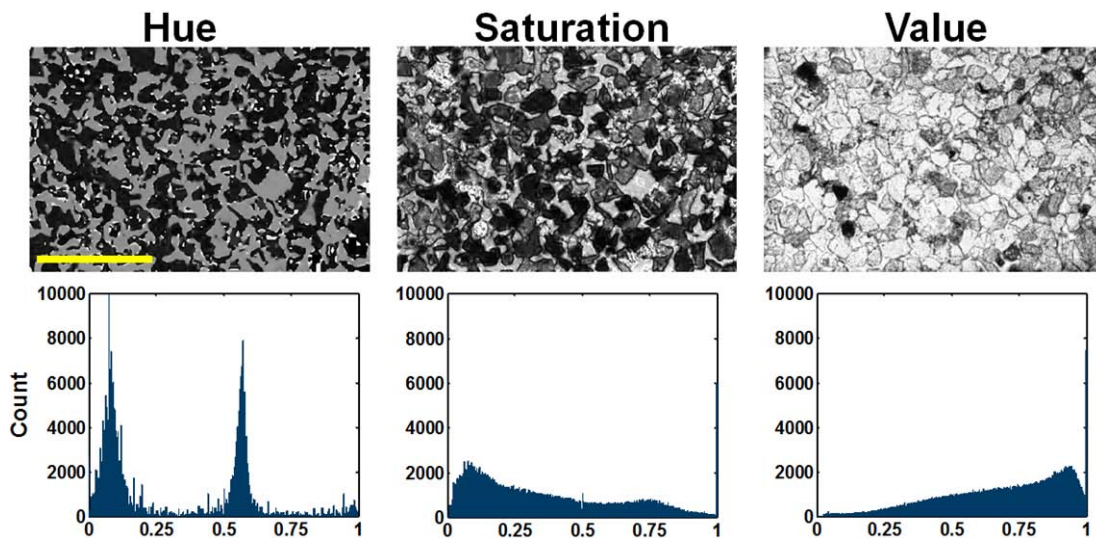
Figure 2.4. The hue, saturation, and value components of the colored HSV image for Sample 1 with the corresponding histograms.

In order to segment the colored thin-section image, we classify the intensity of the three components of a color-space into two groups, pores and grains. We then combine all these classifications, by identifying a pixel as pore only if it is classified

13

as pore in all the three components of the selected color-space. All the other pixels are classified as grains. This is termed as multi-component thresholding.

For classifying the component intensity images into pores and grains, we use Otsu's (1979) method to obtain the threshold for the histogram of every component except for the hue component. The hue component in the HSV color-space quantifies the shade of the color. For the blue color the general hue range is from 0.5 to 0.75. However, the tint or the hue of the blue color changes from sample to sample (Figure 2.2). Hence, a subjective decision was made for the hue component for every sample. This decision becomes very important in samples like Sample 2 where the blue color is not really blue but cyan and hence, the peak of the pore pixels in the hue is slightly shifted (Figure 2.5). The range of the hue chosen for the three samples is shown in Table 2.1.
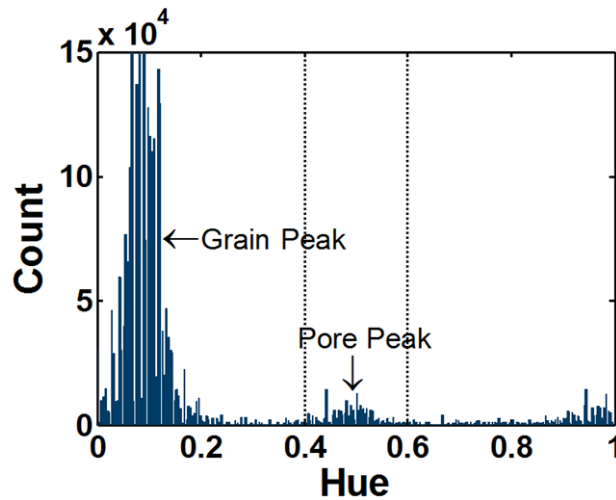
Figure 2.5. The hue histogram of Sample 2 showing the peak of the pore pixels between 0.4 and 0.6 (cyan range) instead of between 0.5 and 0.75 (blue range).

Table 2.1. The range of the hue component used to identify the pore pixels for the three samples.

Sample	Hue Range
Sample 1	0.50 – 0.625
Sample 2	0.425 – 0.575
Sample 3	0.60 – 0.70

2.3.2 Cluster based classification

The cluster analysis techniques assign similar observations into subsets or clusters. We use these techniques to classify pixels of the thin-section image into pores and different grain clusters. For each thin-section we first identify the number of different types of grains and pore clusters (e.g., for Sample 1 we identified six different types of grain clusters -- Figure 2.6). We can now supply either training data that include the attributes of different clusters (supervised learning technique) or the number of clusters into clusters we wish to divide our image (unsupervised learning technique).

2.3.2.1 Supervised Learning Techniques

The supervised learning techniques require training data in order to train the algorithm. Small regions of thin-section image corresponding to pore and different grains are selected to create the training data (Figure 2.6). These regions define the pore and grain clusters in the RGB and HSV color-space. Note that the number of clusters identified using RGB and HSV color-spaces are different as different sets of components see the image differently. Table 2.2 shows the number of clusters identified for each sample.

Table 2.2. The number of clusters identified in each sample for both the color-spaces.

Sample	RGB color-space	HSV color-space
1	7	4
2	5	5
3	6	6

We compared two different methods, discriminant analysis and neural network, for classifying the pore and grain pixels.
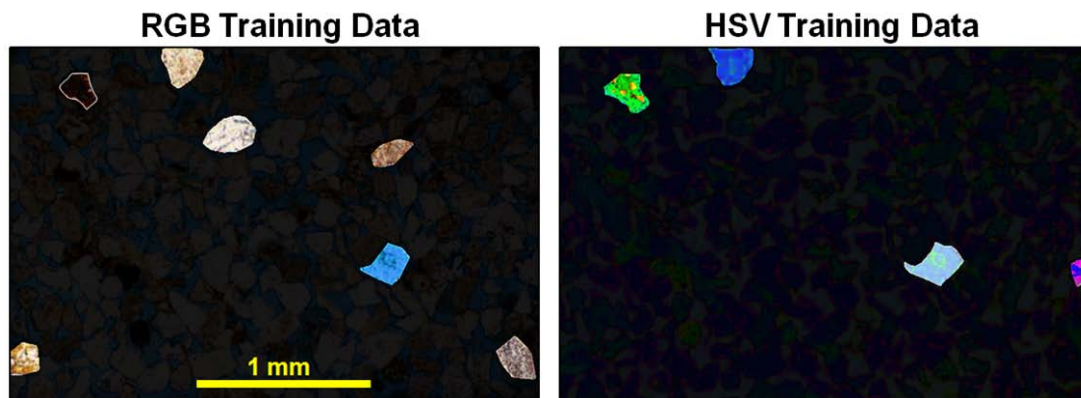
Figure 2.6. The training data for Sample 1 in RGB and HSV color-spaces.

Discriminant Analysis: Statistical discriminant analysis is a technique for classifying a set of observations into predefined clusters based on the multivariate attributes of the observations (Hastie, 2001; Krzanowski 1988; Seber, 1984). Simply put, discriminant analysis method assumes that the attributes of observation (R, G, and B; or H, S, and V) form a vector space, and it draws the boundary between different clusters by considering either first statistical moment (linear) or first two statistical moments (quadratic) of the cluster. Based on the statistical moments used to classify the cluster and how the covariance matrix is estimated, the discriminant analysis method can be divided into five different categories: linear, diag-linear, quadratic,

diag-quadratic, and Mahalanobis. Appendix B presents the covariance matrices for all the samples.

Linear discriminant analysis (L) involves estimating the means for each cluster and a pooled estimate of the covariance in multivariate attribute space. In other words, the distribution of various clusters of pores and grains in the attribute space is assumed to have same shape, while its mean varies from one cluster to the other. Discriminant methods implicitly assume Gaussian distributions, but may be applied to data with non-Gaussian distributions. Even when data are not perfectly Gaussian, discriminant methods have consistently performed amongst the top ten statistical classification methods (Hastie, 2001).

Diag-linear (also known as linear naïve Bayes classifier) discriminant analysis (DL) is essentially same as the linear discriminant analysis method. However, it assumes that different attributes of a cluster are independent of each other, i.e., the value of one attribute, say a red component, does not have any bearing on the value of another attribute, say a green component. This means that the covariances of the attributes are zero, which also means that only the diagonal elements (variance) of the pooled estimate of covariance matrix are non-zero.

The quadratic discriminant analysis method (Q), on the other hand, fits a Gaussian distribution with covariance estimates stratified by group. This implies that the distribution for all the different clusters of grains and pore have a different shape, as well as a different mean in the attribute space.

Diag-quadratic (also known as quadratic naïve Bayes classifier) discriminant analysis method (DQ) is the same as the quadratic discriminant analysis except it

assumes that different attributes of a cluster are independent of each other. Hence, each covariance matrix estimated for different clusters has zero non-diagonal elements.

The Mahalanobis method (M) uses Mahalanobis distances with stratified covariance estimates. The Mahalanobis distance is the distance between two N dimensional points scaled by the statistical variation in each component of the point. For example, if $\bar{x}$ and $\bar{y}$ are two points from the same distribution which has covariance matrix C, then the Mahalanobis distance is given by

$$\bar{r}(\bar{x}, \bar{y}) = \sqrt{(\bar{x} - \bar{y})' C^{-1} (\bar{x} - \bar{y})} \tag{2.1}$$

Neural Network: A neural network is a mathematical model or computational model used for various applications like regression analysis, classification and data processing. It consists of a set of highly interconnected entities, called nodes or neurons which process a weighted set of inputs to produce an output. The weights for input are dynamically calculated during the iterative learning process (also called training the net) in which the observations of training data are passed one at a time to the network. For example, when a neural network is used for classification, it processes observations one at a time, by comparing neural network's classification of the observation (which in the beginning is arbitrary) with the known classification of the observation. The errors from the initial classification of the previous observations are fed back into the network at the successive iteration step and the weights of the input neurons are adjusted to minimize the error.

There are many types of neural network algorithm available, e.g., feed-forward

neural network, radial basis function network, Kohonen self organizing network, recurrent networks, stochastic neural networks and modular neural networks (Rojas, 1996). We exploit only the feed forward algorithm in this study since it is the simplest type of neural network. In this network the information moves in only one direction, forward. There are no cycles or loops in the network. It has a layered structure: one input layer, at least one hidden layer and one output layer.

A neural network can be trained using different algorithms, such as back-propagation algorithm, evolutionary computation methods, simulated annealing, expectation maximization (Rojas, 1996). We use the back propagation method to train our network. It is one of the most commonly used training algorithms. It is a supervised learning method which implements the gradient descent leaning rule, also known as delta rule.

To summarize, in this study we exploit a feed-forward, back-propagating neural network (Bishop, 1995). The feed-forward algorithm used here contains two hidden layers with three and n nodes (three is the number of the components of the color-space while n is the number of clusters we wish to classify our image into). The parameter n represents the number of grains and pores (clusters) as identified in the training data, and hence it may be different depending on the color-space used. For example, for Sample 1, for the RGB color-space, we identify six different types of grains and one pore or seven clusters, while for the HSV color-space we identify three different types of grains and one pore or four clusters (Figure 2.6).

The neural network is trained using the same training data as used for the discriminant analysis methods to classify the thin-section. However, different

instances of training give a slightly different classifier, and hence a slightly different output. In order to be statistically accurate, we obtain the classifications from 10 different classifiers obtained by different training instances. The mean and standard deviation of these 10 classification results are considered while discussing the neural networks.

2.3.2.2 Unsupervised Learning Technique

The K-mean clustering is an unsupervised learning technique for dividing *n*-objects into k clusters ($k < n$) based on their attributes. It assumes that the object's attributes form a vector space. The task is to divide the objects into k clusters such that some metric relative to the centroids of the clusters is minimized. Various metrics can be used, such as the maximum distance to the centroid for any object, the sum of the average distance to centroids over all clusters, the sum of variance over all the clusters, or the total distance between all objects and their centroids. Here we minimize the squared Euclidean distance measured in the attribute space. The number of clusters, k, was kept the same as that of the number of clusters identified for the training data in the supervised learning techniques. Hence, for Sample 1, in RGB color-space, we identify seven clusters while in HSV color-space, we identify four clusters.

2.4 RESULTS

All four classification techniques are used to obtain binary images of three thin-section images. We then calculate the porosity as the ratio of number of pore pixels to total pixels. We compare different classification methods using two criteria as

discussed in section 2.2.

2.4.1 First Criterion: Porosity Error

The first criterion evaluates the error associated with each sample by comparing the point-count measured porosity to the porosity of the thin-section samples obtained using each of the method discussed earlier in this chapter. Henceforth, this will be termed porosity error. Figure 2.7 shows the absolute error for each sample calculated using the following equation:

$$Error = \left(\phi_{Sim} - \phi_{PC}\right) \times 100 \tag{2.2}$$

where ϕ_{Sim} (in fraction) is the porosity of thin-section obtained by a classification method and ϕ_{PC} (in fraction) is the point-count porosity of the thin-section.

Figure 2.7 also shows the 95% confidence interval around the zero error which is calculated as $+2\sigma$ and -2σ (Van der Plas and Tobi, 1965) for each sample, where σ is the standard deviation associated with the point-count porosity. It is calculated using the following equation (Van der Plas and Tobi, 1965):

$$\sigma = \sqrt{\frac{p(100 - p)}{n}} \tag{2.3}$$

where p is the volume percent of a fraction and n is total number of points counted. If the error associated with the method lies within this interval, it is considered as an acceptable method for classification of the thin-section.

In general, we observe a negative porosity error for most of the methods. This implies that in most cases, porosity estimated by the classification methods is lower than the porosity estimated by point count method.

In particular, for the RGB color-space, the porosity errors of quadratic and diag-quadratic discriminant analysis method consistently lie within the confidence interval for all the samples. However, these two methods not necessarily give the least error for all samples. The method that gives least error varies from sample to sample, e.g., for Sample 1 diag-linear discriminant analysis method gives the least error, while for Sample 2 multi-component thresholding method gives the least error. For Sample 3, linear discriminant analysis method gives the least error. However, as quadratic and diag-quadratic discriminant analysis methods are consistent for all the three samples, we recommend them as the best methods for RGB color-space using the first criterion.

For HSV color-space, the K-means clustering method consistently falls within the confidence interval for all the samples. Again, like RGB, the method that gives the least error varies from sample to sample. For Sample 1, the diag-linear discriminant analysis method gives the least error, while for Sample 2 K-mean method gives the least method. For Sample 3, neural network gives the least error. Again, as K-means method is the only consistent method for this color-space, we recommend it as the best method for HSV color-space using the first criterion.

Comparing RGB and HSV color-spaces, we observe that, in general, RGB color-space give less error than the HSV color-space.

This criterion of comparing the porosity obtained using classification methods and the point count method is not perfect. The porosity calculated using point count method divides the pixels in two groups while the cluster analysis methods divide the pixels into 'n' different clusters, where $n>2$. If like cluster analysis methods, the

point count porosity is calculated using multiple groups instead of two groups, the variance associated with the point count porosity will increase, which means more classification methods will be in acceptable range. Hence, current analysis provides a conservative determination of acceptable methods.
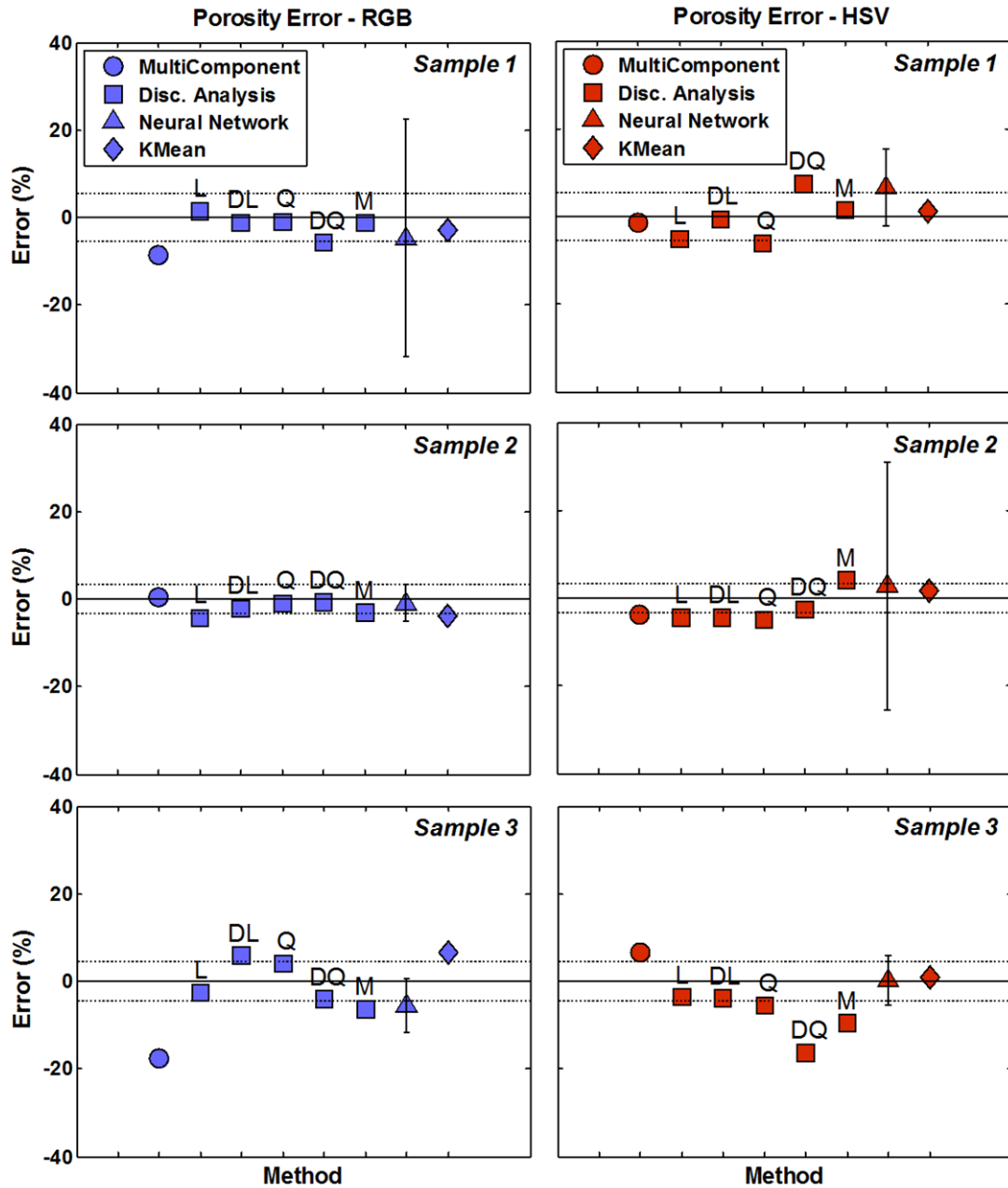
Figure 2.7. The error in porosity of thin-section as obtained using various methods when compared to the point-count porosity. The solid horizontal line in each case represents the 0% error. The two horizontal dashed lines represent the 95% confidence interval.

2.4.2 Second Criterion: Classification Errors

The second criterion for quantifying the efficiency of classification technique

involves pre-selecting 100 known pore pixels and 100 known grain pixels in the colored thin-section image and then noting the percentage of these points that are classified incorrectly. We call the percentage of incorrectly classified grain pixels the grain classification error, and the percentage of incorrectly classified pore pixels the pore classification error. For the three thin-section images under examination Figures 2.8 and 2.9 show the grain and pore classification errors in both color spaces, respectively.

In general, we observe that grain classification error is less than the pore classification error for most of the methods. This implies that more pore pixels are misclassified as grain than the grain pixels misclassified as pore. It means that calculated porosity will be smaller than the porosity of the thin-section. This is consistent with the negative porosity error we observe in Figure 2.7.

In particular, for RGB color-space, the diag-quadratic discriminant analysis method appears to be the best. It does not give the least error in all the cases, but the error associated with this method remains in the lower range for all the three samples. For Sample 1, diag-linear discriminant analysis gives the least error, while for Sample 2, diag-linear, quadratic, and diag-quadratic discriminant analysis methods perform equally well. For Sample 3, the diag-quadratic method shows the least error.

For HSV color-space, none of the method gives small error for all the three samples. For Sample 1, multi-component thresholding method gives the least errors`, while for Sample 2, k-mean cluster analysis gives the least errors. For Sample 3, the quadratic discriminant analysis shows the least classification errors.

Overall, the diag-quadratic method in RGB color-space gives the best result for

the three different samples amongst the methods examined here.
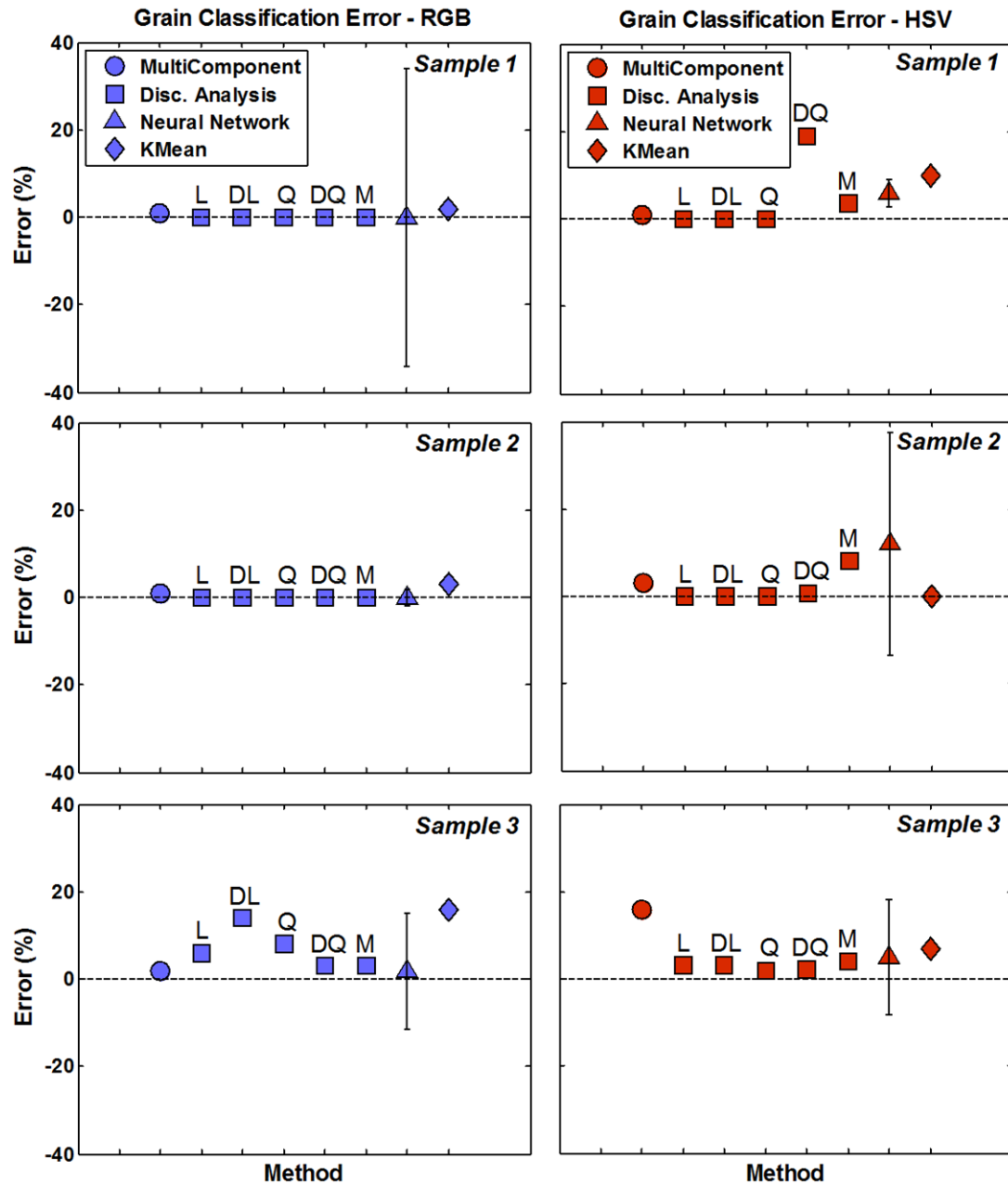
Figure 2.8. The grain classification error in the three samples for different methods and different color-spaces.
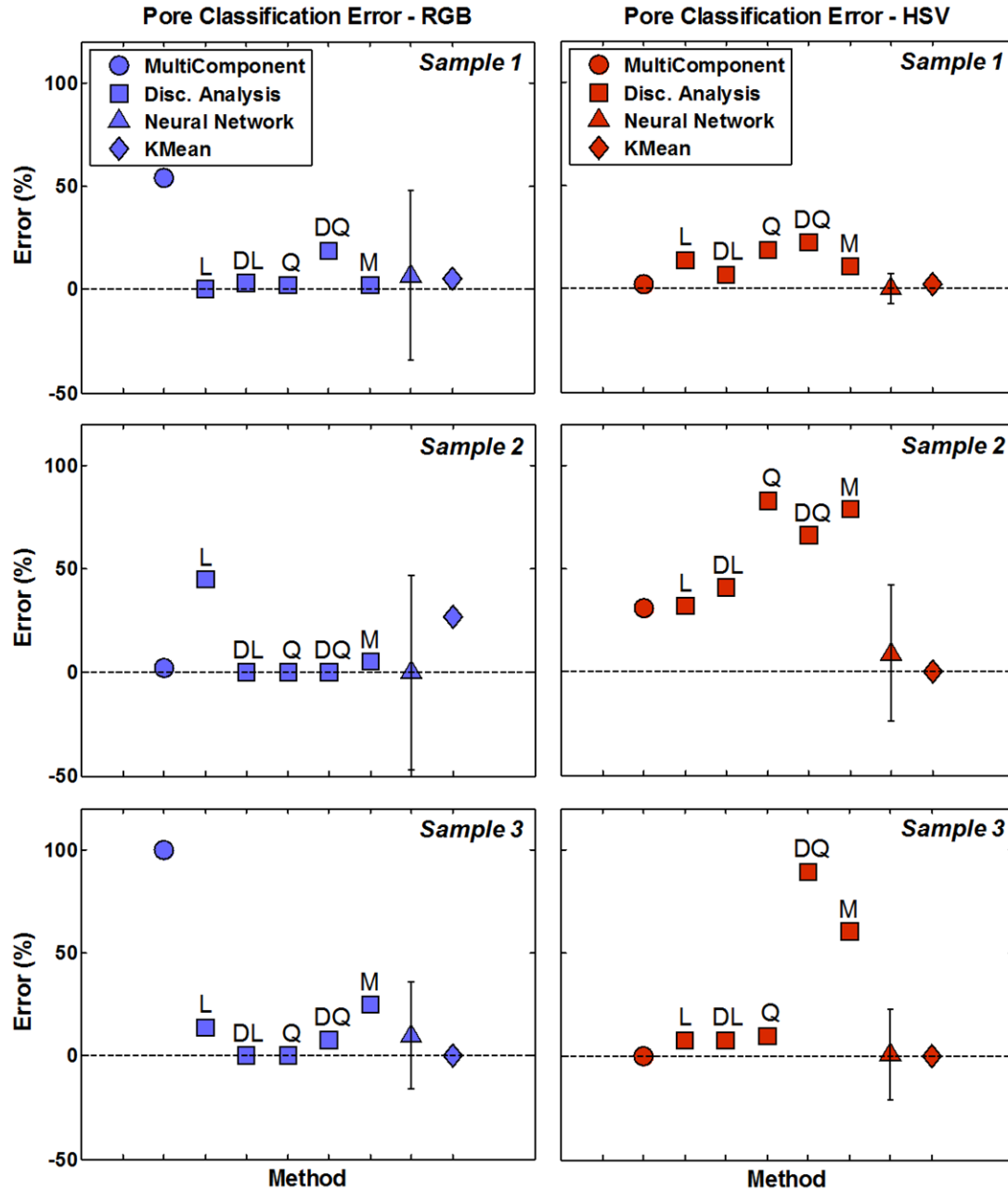
Figure 2.9. The pore classification error in the three samples for different methods and different color-spaces.

2.5 DISCUSSION

The methods we examined for the estimation of porosity from the thin-section in

this chapter are fairly subjective. This section discusses the possible sources of error associated with all the methods examined in this study. As most of the errors discussed here are subjective and usually operator dependent, it is not possible to quantify these errors, however understanding the possible sources of error will enable the operator to minimize them.

The multi-component thresholding methods are the only automatic methods discussed in this chapter. However, as discussed earlier in section 2.3.1, this method is not entirely automatic for HSV color-space. It requires a subjective decision from the user for the hue component, especially if pore pixels have a different tint of blue than usual. This can be a source of error for this method.

Furthermore, this method fails to consider all three components of a color-space together. It calculates the threshold for individual components and then combines them. It ignores the distribution of pores and grains in the multivariate space and instead considers the distribution in single variable space. This forms another source of error for this method.

The supervised learning techniques semi-automatically obtain the porosity of the thin-section. The main source of error in this case is the training data supplied, which is obtained by visual examination of thin-section. Figure 2.10 shows the change in the results of Sample 1 in RGB color-space with the change in the training data supplied for the discriminant analysis methods. It only shows the change in the porosity error and pore classification error for the discriminant analysis methods since the grain classification error remains constant at zero in both the cases, and hence is not shown in the figure. We observe a shift in the porosity error as well as pore-

classification error when we change the training data.

Apart from the errors due to training data supplied, the neural network simulations, as mentioned in section 2.3, return a different result for different training instances. The standard deviation associated with these results is fairly large and hence, makes neural network an unreliable method for classification. Moreover, the mean of these results gives a fairly large error for both the criteria when compared to other methods and hence, is not a reliable method for the classifications.
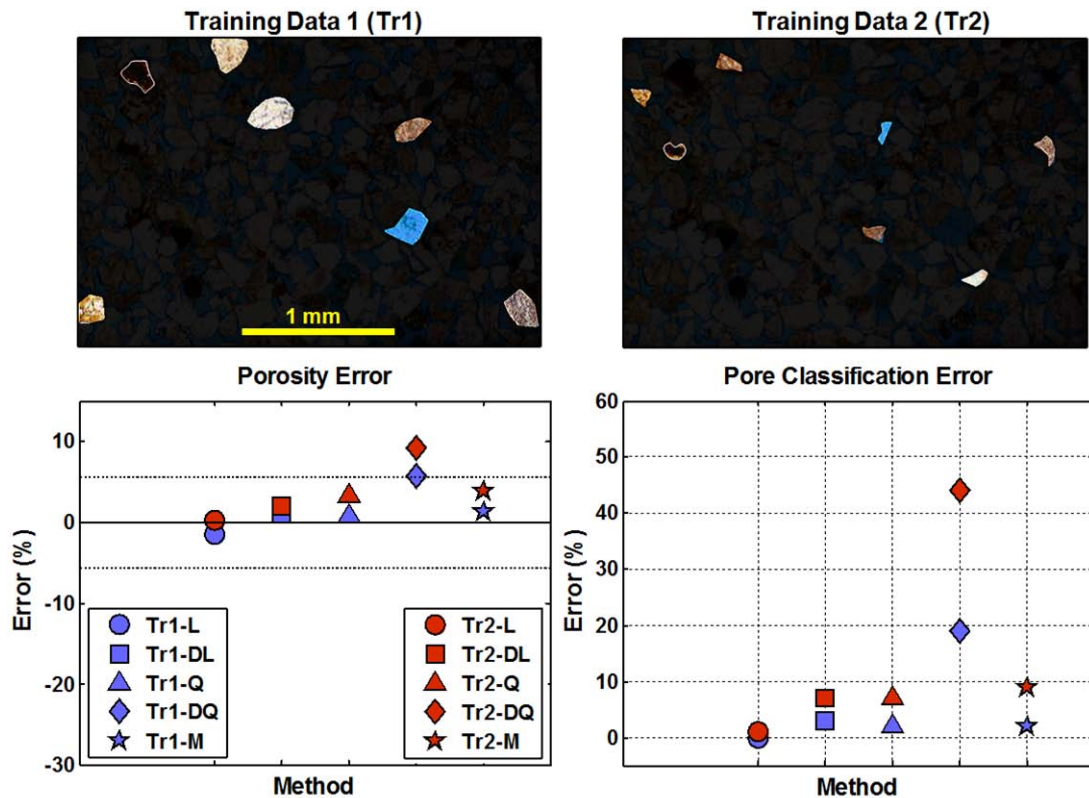
Figure 2.10. The effect of different training data on the porosity error and pore classification error calculated from the segmented images obtained using discriminant analysis methods for Sample 1 in RGB color-space. Both porosity error and pore classification error show a shift in the results with change in the training data.

For the unsupervised learning technique the main source of error is the number of

clusters supplied, which is again obtained by visual examination. Figure 2.11 shows the effect of change in number of clusters supplied to k-mean cluster analysis on the three errors (porosity error, grain classification error and pore classification error) for Sample 1 in RGB color-space. The change in number of clusters affects the classification process. We observe that errors are highest for the two-cluster case but decreases rapidly as we increase the number of clusters. However, the errors again increase slightly after showing a minimum error when number of clusters is four.
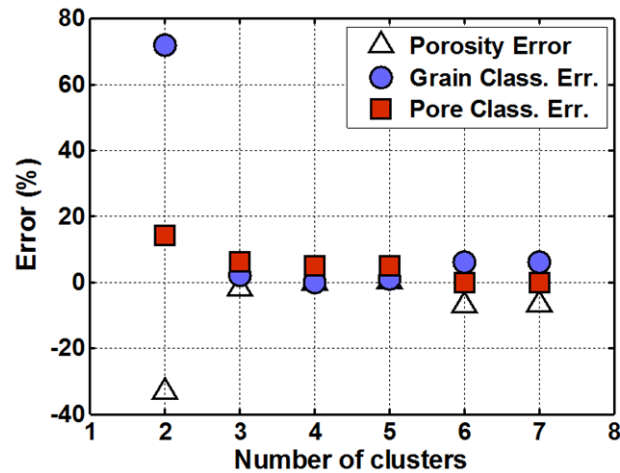
Figure 2.11. The change in the different errors for Sample 1 in RGB color-space as we change the number of clusters supplied to k-mean cluster analysis. All the errors decrease as we increase the number of clusters from two to four, after which it again starts increasing slightly. The final number of clusters (seven for Sample 1) is the same as the number of clusters supplied to the training data of supervised learning techniques.

2.6 CONCLUSIONS

In general RGB color-space gives better results than HSV color-space. Hence, we recommend using the RGB color-space for image classification of thin-section images. Discriminant analysis method performs better than the other methods

examined here. However, the performance of the different types of discriminant analysis method varied from sample to sample. Hence, we recommend all types of discriminant analysis method should be examined while converting colored thin-section to binary image and their performance should be evaluated based on the second criterion that involves selecting the grain and pore pixels from the thin section and evaluating if they are classified correctly using the classification methods under examination.

APPENDIX A: POINT COUNT METHOD

The Glagolev-Chayes point-counting method is used to obtain the porosity of the thin-section. The counting intervals, hence the grid used for point counting varied between different images. The counting intervals (grid spacing) for each were chosen after visual examination of the largest grain size in each image (Table 2.3). In few cases, the numbers of points counted were fewer than 200 points. In those cases, the thin-section image was rotated 180° and counted a second time as suggested by Livingood (2009).

Table 2.3. Point-counting parameters for the three thin-section images.

Image	Counting Interval (pixels)	Number of points
Sample 1	50×50	192
Sample 2	130×130	192
Sample 3	75×75	285

The errors associated with estimating a volume fraction using point counting method have been explored widely in the literature. In this study we include the random error associated with the point-count method due to counting as discussed by Van der Plas and Tobi (1965). Halley (1978) detailed errors associated with the estimation of porosity in thin-section in particular. According to him, there are two main sources of error in this case: (a) inclusion of submicroscopic porosity in solids and (b) edge effects caused due to the finite thickness of thin-section. The error due to submicroscopic porosity can be decreased by *a priori* knowledge of the pore size distribution in the rock under examination. The error due edge effect can be minimized by reducing the thickness of sample under examination. However, the error due to the edge effect increases substantially when (a) the grain size decreases, (b) the edge roughness increases, and (c) grain packing becomes tighter due to presence of small grains. Hence point count method can't be used to reliably estimate the porosity of a thin-section of tightly packed small grains. The operator error associated with the point-count method is usually negligible compared to other errors (Solomon, 1963).

APPENDIX B: COVARIANCE MATRICES

Table 2.4. Covariance matrix for Sample 1: RGB color space.

	R	G	B
R	0.0850	0.0541	0.0308
G	0.0541	0.0532	0.0497
B	0.0308	0.0497	0.0640

Table 2.5. Covariance matrix for Sample 1: HSV color space.

	H	S	V
H	0.0705	0.0155	-0.0025
S	0.0155	0.0739	-0.0218
V	-0.0025	-0.0218	0.0522

Table 2.6. Covariance matrix for Sample 2: RGB color space.

	R	G	B
R	0.0147	0.0129	0.0117
G	0.0129	0.0133	0.0123
B	0.0117	0.0123	0.0126

Table 2.7. Covariance matrix for Sample 2: HSV color space.

	H	S	V
H	0.0443	0.0029	-0.0099
S	0.0029	0.0109	-0.0072
V	-0.0099	-0.0072	0.0116

Table 2.8. Covariance matrix for Sample 3: RGB color space.

	R	G	B
R	0.0704	0.0608	0.0203
G	0.0608	0.0551	0.0206
B	0.0203	0.0206	0.0170

Table 2.9. Covariance matrix for Sample 3: HSV color space.

	H	S	V
H	0.0230	0.0145	-0.0052
S	0.0145	0.0665	-0.0125
V	-0.0052	-0.0125	0.0164

Chapter 3

Comparing Classification Techniques for CT-scan Data

3.1 ABSTRACT

Gray-scale density images obtained by CT scans of rock samples can be converted into binary images of grains and pores using classification techniques. The classification technique is applied to each 2D slice of a 3D gray-scale image to produce 2D binary sections. We analyze five different classification techniques for CT scan images of two packs of loose sand and a sample of the Fontainebleau sandstone. The classification error of each method is quantified by applying it to randomly selected CT-scan slices to find whether the method correctly classifies pixels as a grain or a pore where we are certain that it is the grain or the pore. The porosity obtained for 3D binary digital rock by applying the classification techniques is also compared to the laboratory measured core plug porosity. The discriminant analysis gives the worst results for the samples compared using both the criteria

explained earlier in this abstract. The quality of the results obtained using Rosenfeld's method fluctuates depending on the sample and the criteria and, hence, is not a reliable method. Riddler's and K-mean methods give fairly good results; however, Otsu's method gives the best results for the samples compared using both the criteria.

3.2 INTRODUCTION

In this chapter we compare different classification techniques for the gray scale CT-scan image (or intensity image) in order to identify the pore space and obtain a binary image. The 3D CT-scan image is a set of closely spaced consecutive 2D slices. For simplicity, we concentrate on a few randomly selected 2D CT-scan images instead of all the 2D slices in the 3D set. The classification of the CT scan images is a crucial step since it may strongly affect the rock properties computed on the 3D digital binary rock thus obtained. Although there are other classification methods (e.g., watershed and edge detection methods), here, we concentrate on simpler classification techniques: classification by thresholding and classification by cluster analysis.

Once we identify the optimal classification method, we can use it on all the 2D images in the 3D set to obtain a 3D binary image of pores and grains.

The intensity in the raw CT-scan images corresponds to the X-ray attenuation, which in turn reflects the density and atomic number of the material (Figure 3.1). This is why dense minerals, such as pyrite and dolomite, appear bright, quartz appears darker, and the pores appear almost black. The challenge in classification is to draw

appropriate and realistic sharp boundaries between grains and pores in a raw image where these boundaries are usually smeared.
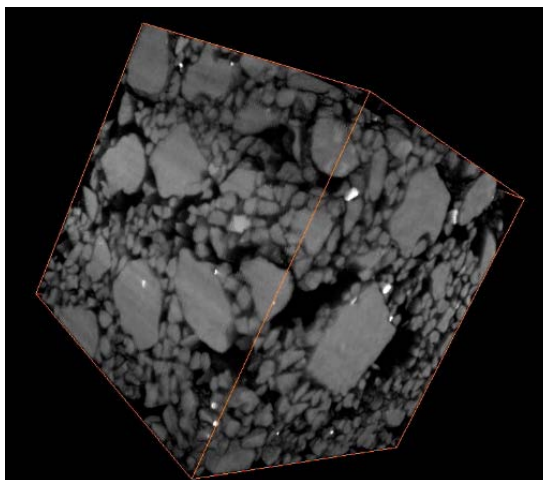
Figure 3.1. 3D rendering of raw CT-scan cubic image of unconsolidated sand (courtesy Ingrain).

There are two possible criteria for selecting the optimal classification technique. One criterion is to match physically measured total porosity with the digitally derived value. As the samples under examination are fairly homogeneous, we can safely assume that these two porosity values should be close to each other. The digital porosity is computed as the ratio of the number of pore voxels to the total number of voxels in the image.

The second criterion is to *a priori* classify selected pixels in the image as pores or grains (by making a decision based on visual examination of the image) and then apply formal classification techniques to match this classification. The less the error of this matching the better the classification technique. This criterion is arguably valid but not entirely objective since the *a priori* classification is operator-dependent and can be ambiguous, especially at the transition bands between the grains and the

37

pores. However, the operator-based errors are usually small (Van der Plas and Tobi, 1965).

We use a combination of the two criteria to identify the optimal classification methods. Note that in case of the first criterion, the physical objects compared (core plug and 3D digital rock) are different, and hence we do not expect the porosities to match exactly, yet they should be close to each other. On the other hand, in the case of the second criterion, we compare the same physical object (the 2D slices), so we can expect the classifications to match closely.

We use these two criteria to compare the five classification techniques divided into two major groups: thresholding techniques and cluster analysis techniques. Unlike thin section image classification, the gray-scale CT-scan classification involves only one variable which makes it ideal for exploring different thresholding techniques. In the thresholding group we explore three techniques: (a) Rosenfeld's (Rosenfeld and Torre, 1983); (b) Riddler's iterative thresholding method (Riddler and Calvard, 1978) and (a) Otsu's (1979) method. In the cluster analysis group, we explore the following two techniques: (a) the K-mean clustering method (Hastie, 2001; Seber, 1984); and (b) the discriminant analysis method (Hastie, 2001; Krzanowski 1988; Seber, 1984).

Amongst the techniques compared here, we find that the Otsu's method is most accurate for all the samples. Riddler's and K-mean methods follow closely. Rosenfeld's method works well for one of the sample examined here but it gives large errors for the other samples. Discriminant analysis method does not give accurate results for any case examined here.

The rest of the chapter is organized as follows. In section 3.3, we describe the CT-scan samples and their pre-processing, which we will use in the rest of the thesis. In section 3.4, we describe the five different methods compared here. In section 3.5, we present our results comparing all the methods using the two criteria described above for the three samples. In section 3.6, we conclude the chapter with the recommendations to be followed in next three chapters.

3.3 DATA DESCRIPTION AND PRE-PROCESSING

In this thesis we work with the CT-scanned images of three different rocks. 3D Computational Tomography (CT) of rock core sample images the rock fragment and yields a set of 2D intensity images. The intensity of these images corresponds to the X-ray attenuation, which in turn reflects the density and atomic number of the material (Ketcham and Carlson, 2001).

In this section, we detail the rock samples used in this study as well as describe the necessary image pre-processing of the intensity image.

3.3.1 Data Description

We use two types of clastic sediment: (a) two reconstructed samples of loose sand —beach sand from Pomponio Beach, California (PB) and coastal dune eolian sand from San Gregorio, California (SG); and (b) one Fontainebleau (FB) sandstone sample. The first two samples were prepared by Kameda (2005) by mixing loose sand grains with epoxy, compacting these aggregates and letting the epoxy solidify.

The Fontainebleau sample was cut from a large fragment of Fontainebleau formation (France), which is an early Oligocene (36–27 Ma) unit, 50–80 m thick, of

fine-grained, well-sorted, quartz arenite (Cooper, 1994; Thiry et al., 1988). The Fontainebleau formation is a pure quartz formation which makes it ideal for experimentation and hence, it is an extensively studied formation. The formation has several laterally extensive quartz-cemented horizons which is responsible for a variable porosity ranging from 7% to 15%.
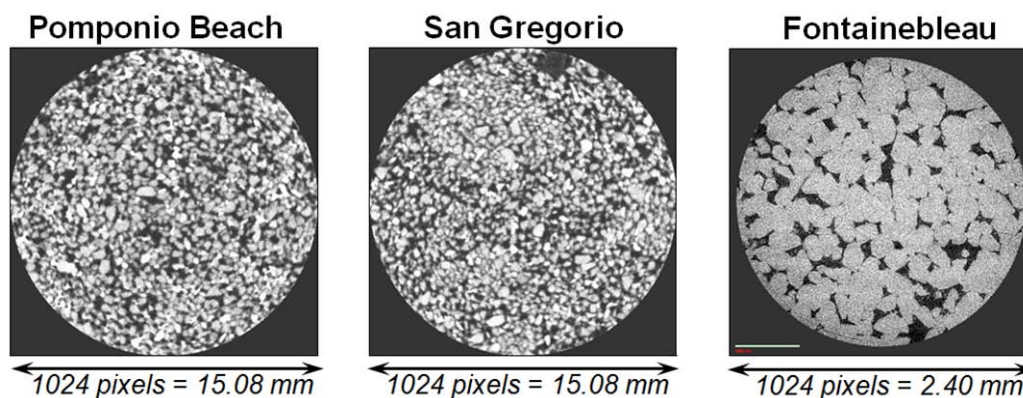
Figure 3.2. Selected 2D slices of the samples used in this thesis.

The PB and SG samples were scanned at University of Texas, Austin. The details about the CT-scan can be found in Kameda (2005). The FB sample was scanned at Ingrain. The details about the CT-scan can be found at their website (http://www.ingrainrocks.com/).

All three samples were CT-scanned at a resolution high enough to reveal the geometries of the pore space and mineral matrix. However, the resolution of the FB sample is different from the PB and SG samples as they were CT-scanned at different locations. Figure 3.2 shows selected 2D slices for all the three samples. Note this figure shows the circular slices of each sample. For all the analysis, we need a 3D digital rock cube and hence, from these circular slices, we extract the largest possible square. The resolutions, the size of largest square area extracted, and the number of

slices for each case are shown in Table 3.1. The size of the largest square and number of slices in turn define the size of the largest 3D digital rock we can obtain using the CT-scan data.

Table 3.1. The size of largest 3D digital rock obtained from CT-scan data and the resolution of CT-scan data for the three samples. The resolution is the size of one pixel in mm.

Sample	Resolution	Largest square size (pixels)	No. of slices
PB	0.01477 mm	725 by 725	522
SG	0.01460 mm	725 by 725	522
FB	0.00234 mm	600 by 600	800

Kameda (2005) measured the porosity, permeability, and grain size distribution of the core plugs of the PB and SG in the lab. Gomez (2009) measured the porosity, permeability, and electrical conductivity of the FB sample (core plug GW28 in Gomez, 2009). The grain size for the FB sands has been reported to be uniform at 250 microns (Bourbie and Zinszner, 1985). The laboratory measured parameters for the three core plugs are shown in Table 3.2.

Note the high porosity and permeability of the PB and SG samples. Since both the samples were artificially created from loose sands, they both are very near to the critical porosity state (~ 0.4).

Table 3.2. Laboratory measured grain size, porosity, permeability, and electrical formation factor as measured by different researchers for the three samples.

Sample	Mean grain size (microns)	Porosity (fraction)	Permeability (mD)	Electrical formation factor	Measured by
PB	437	0.34	58400	N/A	Kameda, 2005
SG	392	0.39	50000	N/A	Kameda, 2005
FB	250	0.18	896	17.32	Gomez, 2009; Bourbie and Zinszner, 1985

3.3.2 Image Pre-processing

The PB and SG samples do not require any image processing and are used as such in our study.

The FB images, on the other hand, have speckle noise which is a random, deterministic, interference pattern in an image (Figure 3.3). We need to remove the speckle noise from these images in order to obtain a 3D digital binary cube. The right panel of Figure 3.3 shows the resulting speckled binary image if we don't apply any noise reduction technique to remove the "salt and pepper" from the images**.**
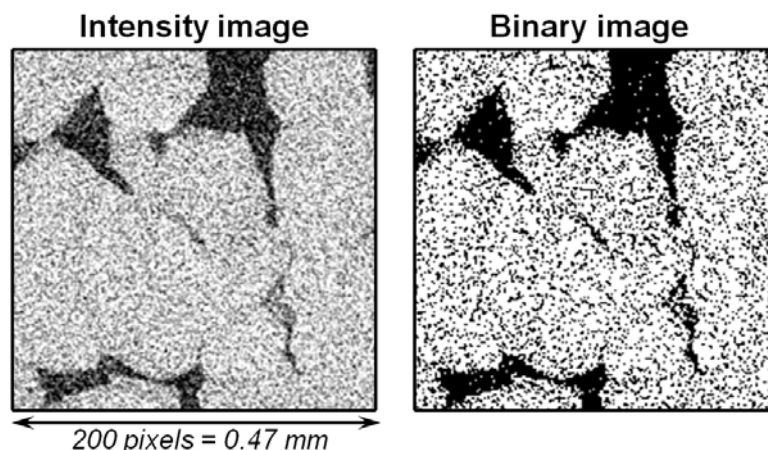
Figure 3.3. A small area (200 × 200 pixels) of a FB CT-scan slice (left) and converted binary image without any image processing.

We compare common adaptive filters to remove the speckle noise. Specifically, we apply the following 9-neighbor 2D adaptive filters: median filter (Marion, 1991), Frost filter (Frost et al., 1981) and Kuan filter (Kuan et al., 1987) to the image. The median filter calculates the median of all the neighboring entries (in this case, 9 neighbors) and assigns it to the pixel. The Frost filter is an adaptive Weiner filter that is based on multiplicative noise model. It uses local neighborhood to calculate the local statistics (local mean and variance) which in turn is used to calculate the weights. The Kuan filter is a local linear minimum mean square error (MMSE) filter based on multiplicative noise model. It updates the noisy pixel by estimating the minimum mean square error using the local neighborhood mean and variance. A detailed comparative study of different filters used for suppressing speckle noise is given by Sudha et al. (2009).

After applying these filters, we obtain binary images which are shown in Figure 3.4. For consistency, we use Otsu's method to convert the gray scale images to

binary images.

By visual inspection, we find that Kuan filter works best for these images. However, we still observe some speckles in the binary image. In order to remove these remaining speckles, we apply a 27-neighbor 3D median filter to the 3D binary image obtained after applying the Kuan filter. The final pre-processing steps and resulting images at every step is shown in Figure 3.5.
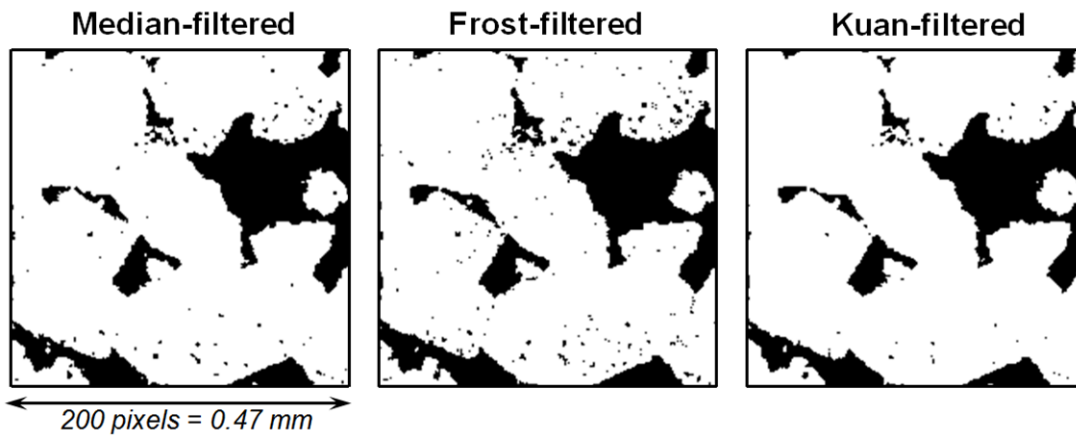
Figure 3.4. The comparison of binary images obtained after applying three different 9-neighbors 2D adaptive filters (Median, Frost, and Kuan) to the CT-scan image. By visual examination, the Kuan filter gives the best result.
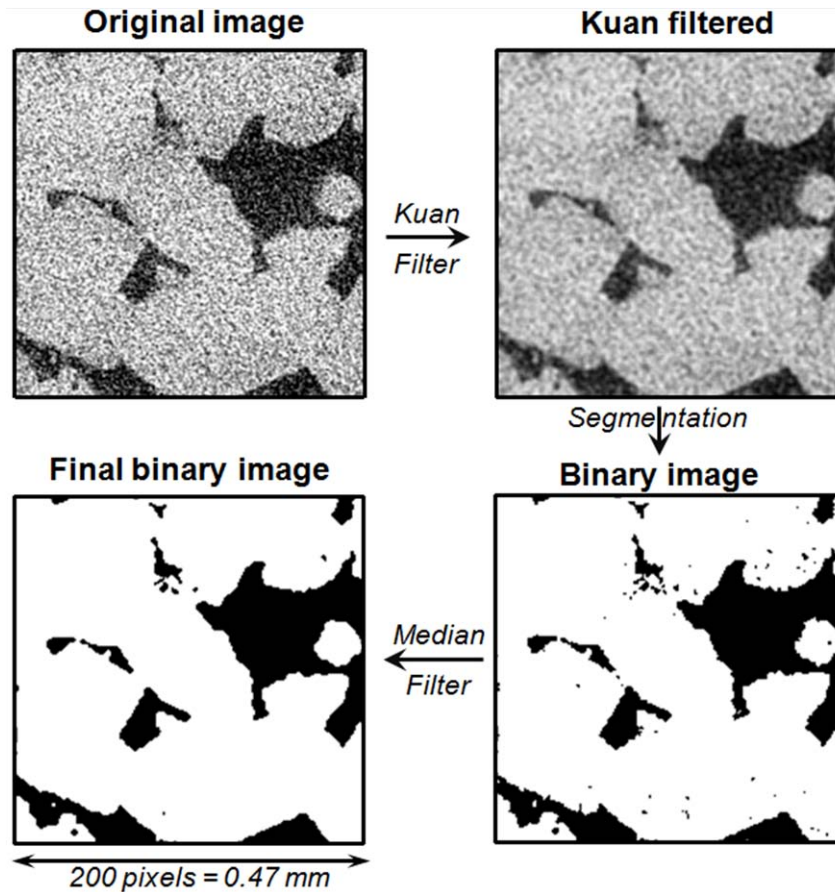
Figure 3.5. The steps of the image pre-processing for CT-scan images of the Fontainebleau sandstone. The original image is first filtered using 9-neighbors 2D adaptive Kuan filter to reduce the speckle noise in the image (top-right). It is then classified using an optimal classification scheme (bottom-right). The set of binary images thus obtained is combined to form a 3D binary rock which is then filtered using 27-neighbors 3D median filter (bottom-left).

3.4 CLASSIFICATION METHODS

We examine different classification methods to convert an intensity image into a binary image. As mentioned earlier in section 3.1, the classification schemes are divided into two groups: classification by thresholding and classification by cluster analysis.

3.4.1 Classification by thresholding

Classification by thresholding involves analyzing peaks, valleys, and curvatures of the histogram of pixel values in an intensity image. A histogram is a function $f(x)$ where x is the intensity value in the image and f is the count normalized by the total number of samples (Figure 3.6).

We explore three methods to find the optimal threshold by analyzing the histogram. The methods we focus on are Rosenfeld's convex hull method (Rosenfeld and Torre, 1983), Riddler's iterative thresholding method (Riddler and Calvard, 1978) and Otsu's method (1979).

Rosenfeld's method is based on the shape properties of the histogram. The algorithm calculates the convex hull of the histogram, which is defined as the smallest convex set containing the histogram (O'Rourke, 1994). The quick-hull algorithm (Barber et al., 1996) calculates the convex hull, $H(x)$, which is then used to obtain the concavity of the histogram. The difference between the convex hull and the original histogram $|H(x) - f(x)|$ defines the concavity of the histogram. The highest concavity point is used as the threshold. We modified this method slightly since the point of highest concavity in the CT-scans often lies either towards the beginning or towards the end of the histogram due to a sharp drop from the pore to grain peaks. Hence, we locate the two minima in the concavity curve and limit the search of the highest concavity point between these two minima (Figure 3.6). This highest concavity point between the two minima of concavity forms the threshold for Rosenfeld's method.
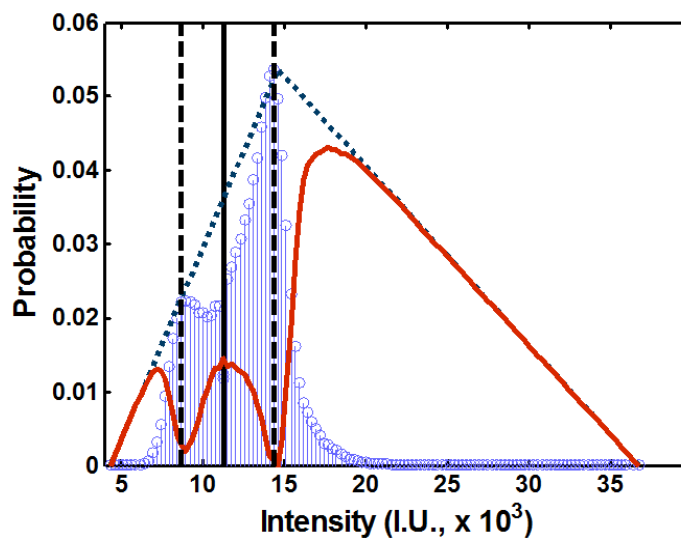
Figure 3.6.   Rosenfeld's method. The blue vertical lines correspond to the histogram with normalized count or probability of the intensity; the dashed vertical lines are two minima in the concavity curve (bold red curve) – the maximum concavity between the two minima determines the threshold (solid vertical line). The triangular shape (dotted lines) is the convex hull used to calculate the concavity as the difference between the convex hull and the histogram.

Riddler's iterative thresholding method is based on the assumption that a bimodal probability distribution function $f(x)$ is the sum of two Gaussian probability distribution models $f_1(x)$ and $f_2(x)$: $f(x) = f_1(x) + f_2(x)$. The initial threshold required to begin the iteration procedure is assumed to be the arithmetic mean of the intensities in the image. At the following iterations, the means of each Gaussian model are computed and their arithmetic average is assumed to be the next threshold. The threshold at every iteration step serves to break the original histogram into two parts and two new Gaussian models are fit to these two parts. Iterations terminate when the difference between the two successive thresholds is sufficiently small. In our analysis we terminate the iterations if the difference between two successive

47

thresholds is less than 10^{-10}.

Otsu's (1979) method minimizes the weighted sum of within-class variance of the two clusters to establish an optimum threshold. This minimization of within-class variance is equivalent to maximization of between-class scatter.

3.4.2 Classification using Cluster Analysis

Cluster-analysis methods separate pixels by sorting their intensity values into two clusters based on a different principle. The two principles utilized here are: the k-mean clustering method (Hastie, 2001; Seber, 1984) and the discriminant analysis method (Hastie, 2001; Krzanowski 1988; Seber, 1984).

The *K-mean clustering* is an unsupervised learning technique for dividing *n*-objects based on their attributes into k clusters ($k < n$), as explained in Chapter 2. In this chapter, we use the squared Euclidean distance measured in the attribute (intensity) space for $k = 2$.

The *statistical discriminant analysis method* is a supervised learning technique used to identify boundaries between different groups based on multivariate attributes of objects as detailed in Chapter 2. In order to do so, a training data set of intensity values of two groups is supplied. The criterion based on statistical moments of groups identified in training data is then used to categorize groups in the sample image. In our implementation, the training intensity data supplied for the discriminant analysis was obtained from a randomly selected slice for each sample, by declaring a selected area as grain and another one as pore. As our training data set has only one attribute, namely intensity, we only use linear statistical discriminant

analysis method for the present analysis. The other statistical discriminant analysis methods (diag-linear, quadratic, diag-quadratic and Mahalanobis) gave worse results than the linear discriminant analysis for the selected 2d slices and hence are not presented in the current discussion.

3.5 RESULTS

The five classification techniques were used to obtain binary images of 2D CT-scan slices. Figure 3.7 shows the result for a randomly selected PB 2D slice.
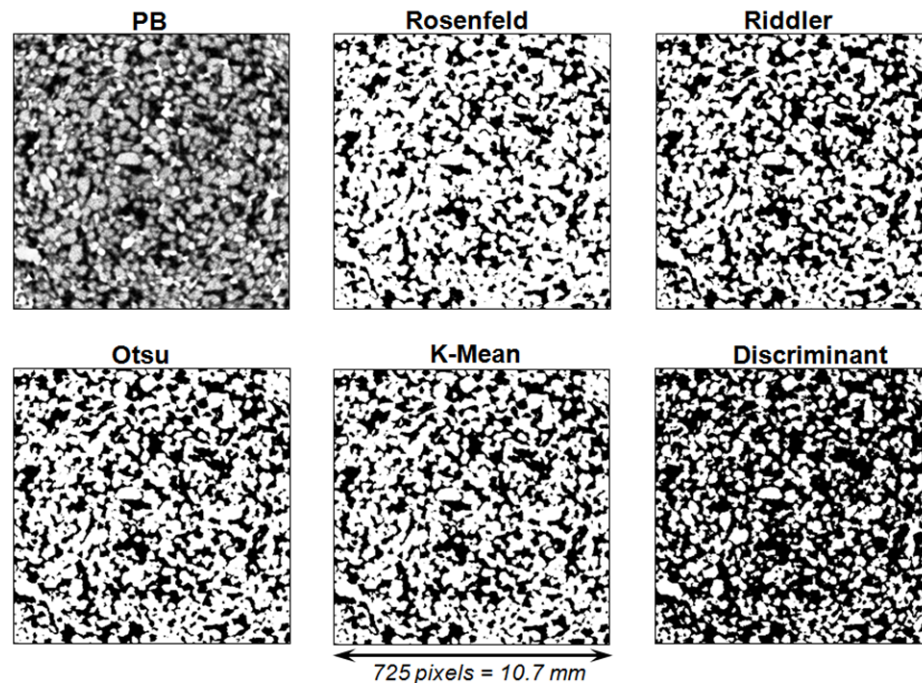
Figure 3.7. The original gray-scale image of the PB 279 (top left) and its classified images resulting from the five classification methods as marked on top of each image. Light pixels are grains while dark pixels are pores.

As discussed earlier in section 3.2, the first criterion to evaluate the error associated with each sample is by comparing the laboratory measured porosity to the porosity of the 3D digital rock obtained using each of the method discussed. Figure

3.8 shows the absolute error calculated using the following equation:

$$Error = |\phi_{Sim} - \phi_{Lab}| \times 100 \qquad (3.1)$$

where ϕ_{Sim} is the porosity of 3D digital rock obtained by a classification method and ϕ_{Lab} is the porosity of the core plug as measured in laboratory (Table 3.2).

According to this criterion, Riddler's, Otsu's, and K-mean methods give results close to each other. Otsu's method gives lowest error among all the methods except for the FB sample. However, the error in porosity obtained by Otsu's method for the FB sample is reasonably small (~2%). The errors in Riddler's and K-mean methods for all the samples are fairly low as well.

Rosenfeld's method gives a low error for the FB and PB sample (~2% and ~1%, respectively) however it gives a high error (~8%) for the SG sample. This high error in case of the SG is due to the oscillation in the one of the two peaks in the histogram for few of the SG intensity images (Figure 3.9). The concavity curve for these samples does not provide an optimal threshold, and hence we observe a high error for the SG sample. As the porosity calculated for the SG sample is higher than the laboratory measured porosity, we conjecture that the number of slices with erroneous high threshold is larger than the number of slices with erroneous low threshold.

For all the samples, the errors are highest for discriminant analysis method. This is predictable since we use the training data obtained from a single 2D slice to classify all the slices in the 3D CT-scan.

Hence according to this criterion, Otsu's, K-mean, and Riddler's methods, in that order, give the best results and form possible candidates for the optimal classification scheme.
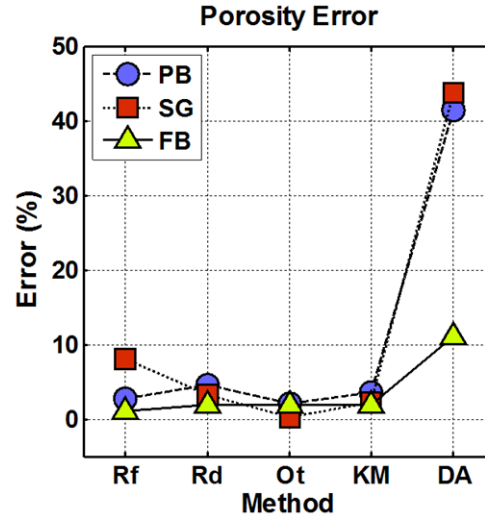
Figure 3.8. The error in porosity of 3D digital rock as obtained using various methods when compared to the laboratory measured porosity (Equation 3.1). The x-axis shows different methods where Rf – Rosenfeld's method; Rd – Riddler's method; Ot – Otsu's method; KM – Kmeans method; and DA – discriminant analysis method.
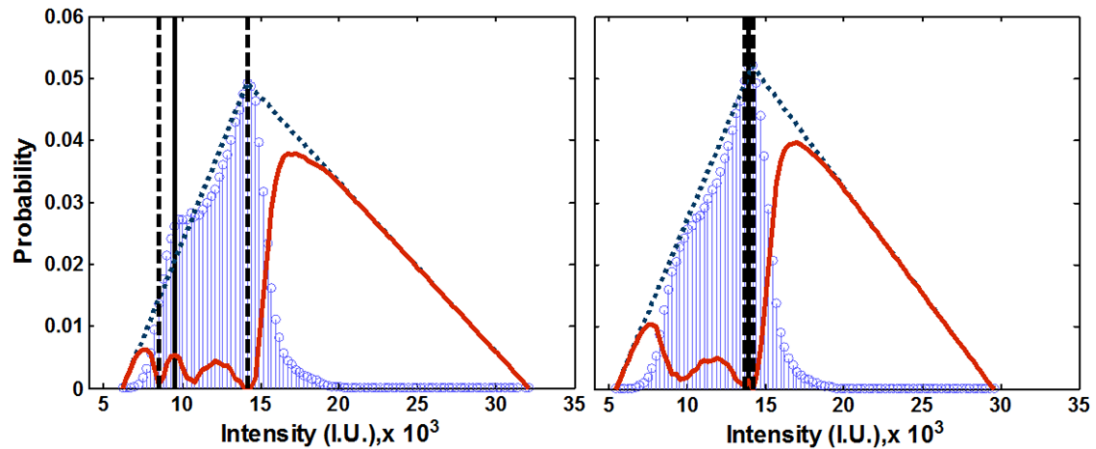
Figure 3.9. Rosenfeld's method does not work for a few SG 2D slices as seen in the two examples shown above. In the first case the calculated threshold is lower than expected due to the oscillation in low intensity peak (corresponding to pore), while in the second case, it is calculated higher due to a small oscillation in the high intensity peak (corresponding to grain). In the first case, the porosity calculated using the threshold will be lower than true porosity of the 2D slice while in the second case the porosity will be higher than expected. The legends for this figure are same as Figure 3.6.

The second criterion to quantify the efficiency of each classification technique uses 50 known grain and 50 known pore pixels in the randomly selected slices and then noting the percentage of these points that were classified incorrectly. The percentage of incorrectly classified grain pixels is henceforth called the grain classification error, whereas the percentage of pore pixels incorrectly classified is called the pore classification error. Figure 3.10 shows the classification error of different methods for the three 2D slices.

The pore classification error in each case for all the samples is 0%, while the grain classification error varies. This means that in some cases when grain classification error is not zero, the porosity of the 2D slice is slightly over-predicted.

Among all the methods, Otsu's method shows the least grain classification error for all the samples. In fact, it gives 0% error for the PB and SG samples while a 2% error for the FB sample. A 2% error implies that out of 50 grain pixels identified by the operator, only one was misclassified. This is an acceptable margin of error.

Riddler's and K-mean methods consistently give a 2% error for all the samples, while discriminant analysis gives the worst result for all the samples. Rosenfeld's method, on the other hand, shows a slightly higher error for the FB sample (~6%).
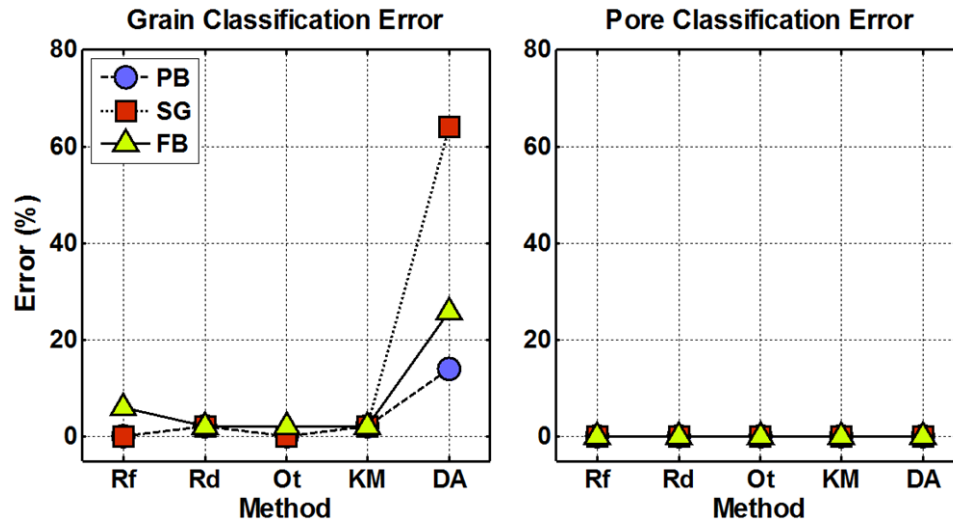
Figure 3.10. The grain and pore classification error in the randomly selected 2D slice of three samples. The x-axis show different methods where Rf – Rosenfeld's method; Rd – Riddler's method; Ot – Otsu's method; KM – Kmean method; and DA – discriminant analysis method.

Hence according to this criterion, Otsu's, k-mean, and Riddler's methods, in that order, give the best results and form possible candidates for the optimal classification scheme. As Otsu's method is the best method amongst the methods compared, it is the recommended method for classification of CT-scan images.

3.6 CONCLUSION

We compare five different classification techniques for three samples used in next three chapters. We identify Otsu's method as the best classification method for these three samples based on the two different criteria. We will use Otsu's method in Chapter 4 and 6 to convert the CT-scan images into 3D binary image.

Chapter 4

Sample Size and Transport Properties Trends

4.1 ABSTRACT

Representative elementary volume (REV) is often used for representing rock properties at large scale. In this paper we explore the change in the porosity-permeability, and porosity-formation factor trends as we change the scales of observation below the defined REV for the three digital rock samples described in Chapter 3. The objective is to identify the smallest scale at which the physical trends can be identified. The rock properties are obtained using numerical simulation of the digital rocks of varying sizes, from REV size, which is defined as ten times the autocorrelation range of the 3D binary image of the rock samples, to the smallest scale at which there are still connected pores present to allow the fluid flow and electrical conduction across the sample (~1.5 times of autocorrelation range of the binary rock sample). The rock property trends, porosity-permeability, and porosity-

formation factor, remain constant at all the subsample sizes and match laboratory measurements. However, the scatter in these trends increases as the subsample size decreases. At the smallest subsample size examined, the scatter becomes significant. This scatter can be reduced by using a moving porosity window average.

This study demonstrates that we can obtain meaningful rock property trends using the digital rocks at a scale much smaller than the REV sizes.

4.2 INTRODUCTION

Geophysical measurements span a large range of scale from seismic level, to log level, to core sample laboratory level, and finally to CT-scanned micro scale level. In order to deal with such large range of scale, geophysicists often refer to a representative elementary volume (REV). The REV is defined as the smallest volume over which a measurement can be made that will yield a value representative of the whole (Bear, 1988). In other words, the rock properties obtained at a scale smaller than the REV fluctuate considerably, while at a scale larger than the REV these fluctuations are significantly less. However, the concept of the REV does not shed light on how the physical trends between the rock properties change above and below the REV.

Kameda (2005), Kameda et al. (2006), Dvorkin (2009), Dvorkin and Nur (2009), and Dvorkin et al. (2009) explored the effect of scale on rock-property trends like porosity-permeability, porosity-formation factor, and porosity-elastic moduli. They compared the trends obtained at the micro-scale using digital rock physics methods to trends measured at laboratory measurements and found them to correlate fairly well.

However, they did not formally define the REV for these rocks and simply compared physical trends obtained at micro-scale to laboratory scale. This micro scale may or may not be above the REV for these rocks.

In this chapter, we extend their study by first defining the REV in terms of the autocorrelation range of the 3D binary image (Keehm, 2003). We next obtain physical trends, porosity-permeability and porosity-formation factor, at this scale using different rock property simulations: Lattice Boltzmann for permeability and FEM for electrical formation factor. We then obtain the rock properties trends for sample sizes below REV and compare them with the laboratory data as well as the theoretical relations. We find that the trends between these properties are fairly stable with respect to the size of the sample. However, the scatter around these trends increases as we decrease the subsample sizes. This becomes significant for the smallest sample size for the samples used in this study.

This scatter in the smallest sample size is reduced by employing a moving porosity window averaging. This involves computing power averages for the permeability and formation factor of all the subsamples whose porosity fall into the window and then plotting it versus the arithmetic averaged porosity of the subsamples in the window. We successfully obtain a tight trend using this method, when we use an arithmetic average for permeability and a harmonic average for formation factor for the three samples used in this study.

This result implies that, at least for the cases explored, we can experiment at the below-REV level and still obtain physically meaningful, stable, and usable results – trends between physical properties of sediment. The advantage of using smaller size

samples instead of the REV size sample is that at smaller scale, we span a larger portion of the trend using the same fragment of the rock, whereas the REV-sized samples are concentrated in a smaller portion of the trend. The smaller size samples are also computationally inexpensive and hence, are faster to process.

In this thesis we concentrate on porosity-permeability and porosity-formation factor trends. Formation factor-permeability trends is not considered here, since the theoretical relations between these two properties require some estimate of pore diameter of the physical sample, which is not available.

The rest of the chapter is structured as follows. In section 4.3, we first define REV in terms of autocorrelation range of 3D binary image. We then present the REVs for the three samples used in this study, as calculated by using their autocorrelation range. In section 4.4, we describe different computer simulation algorithms used to determine the porosity, absolute permeability, and electrical conductivity. In section 4.5, we present our results. In section 4.6, we discuss porosity window averaging as a method to reduce the scatter for the smallest sample, followed by our conclusions in section 4.7.

4.3 AUTOCORRELATION RANGE AND REV

Keehm (2003) gave a quantitative recipe for determining an REV of homogenous and isotropic rocks from a one-dimensional autocorrelation range computed in a 2D binary image of rock: $L > 10a$, where L is the linear size of an REV cube and a is the autocorrelation range. Since the rock samples used in this study (two artificial sandstone samples and a Fontainebleau sample as described in Chapter 3) are fairly

homogeneous and isotropic, we define the REV, in accordance to Keehm's result, as ten times the autocorrelation range of a 3D binary image of rock.

In order to determine the autocorrelation range *a*, the autocorrelation function *A(h)* is computed on the 2D binary images:

$$A(h) = \langle\, f(r)\, f(r+h)\rangle, \tag{4.1}$$

where *h* is the distance between two data points, one at location *r* and the other at *r+h*. This function can be one-, two-, or three-dimensional. Here we use the 1D autocorrelation function following the procedure described in Keehm (2003) but we compute it in all three directions. For each of these directions, we then compute the variogram *γ(h)* using

$$\gamma(h) = C(0)(1 - A(h)), \tag{4.2}$$

where *C*(0) is the covariance of the data. This function is then fit by an exponential form:

$$\gamma(h) = C(0)(1 - e^{-\frac{3h}{a}}). \tag{4.3}$$

The parameter *a* is the autocorrelation range – essentially the distance *h* at which the variogram levels out.

Typical variograms for the three samples, Pomponio Beach (PB), San Gregorio (SG), and Fontainebleau (FB) are shown in Figure 4.1. The resulting autocorrelation ranges are listed in Table 4.1, where *a* for each sample is averaged for all the directions. The scatter with respect to the direction is small which indicates that all three samples are isotropic and homogeneous with respect to *a*.
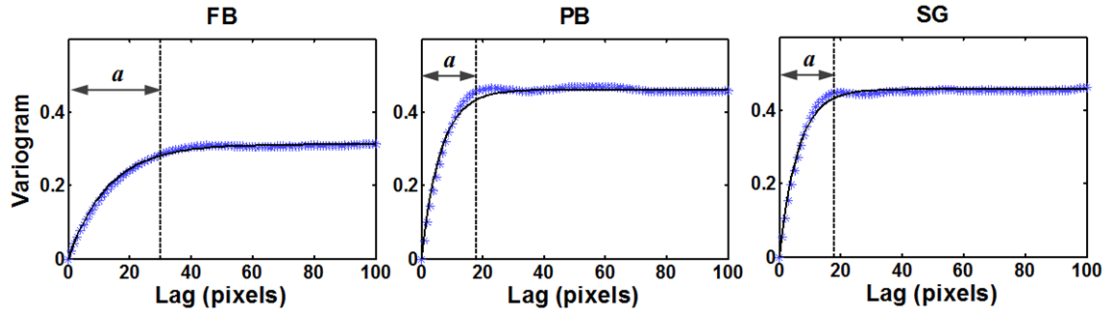
Figure 4.1. Typical variograms for the FB, SG, and PB plotted against the lag vector which is given in grid units. The autocorrelation range (*a*) is about 30, 15, and 17 grid units for the FB, SG, and PB, respectively.

Table 4.1. Autocorrelation ranges (*a*) and REV sizes of the samples under examination.

Rock	Mean *a* (pixels)	Std *a* (pixels)	Mean *a* (mm)	Std *a* (mm)	REV (pixels)	REV (mm)
PB	16.8	0.8	0.2481	0.0118	~ 170	~ 2.5
SG	14.9	0.6	0.2201	0.0089	~ 150	~ 2.2
FB	30	6	0.070088	0.014199	~ 300	~ 0.7

Based on Table 4.1, the REV sizes for the three samples (PB, SG, and FB) are about 170, 150, and 300 pixels, respectively, or 2.5, 2.2, and 0.7 mm.

We randomly select REV sized samples from a larger host 3D binary rock samples, which are produced from CT-scan images as described in Chapter 3, and calculate their porosity (ϕ), absolute permeability (k), and the electrical formation factor (F) using different computer simulations. We repeat these computations on a large number of subsamples smaller than REV, randomly selected from the same host 3D image. The smallest subsample size used in these experiments is about 1.5 times autocorrelation range because at scales smaller than this the connected pore space may disappear, resulting in zero permeability and conductivity. Figure 4.2 show a

typical 2D slice of each rock sample used in the present study with the 2D representation of the subsample sizes for which different physical properties were simulated.
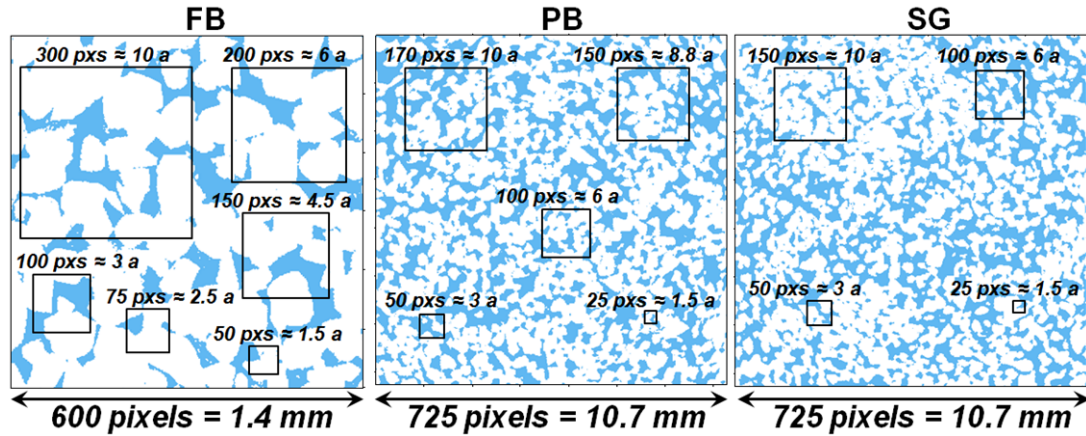
Figure 4.2. Selected segmented 2D slices of the samples used in this study. From left to right: the Fontainebleau, Pomponio Beach, and San Gregorio samples. The different squares in each slice represent the size of the subsamples for which ϕ, k, and F were computed. The subsample sizes are shown in pixels as well as relative to their mean autocorrelation range.

4.4 COMPUTING ROCK PROPERTIES

In this section we describe the simulations used for determining the rock properties porosity, permeability, and electrical conductivity.

The *porosity* of the 3D binary sample is simply the ratio of the number of the pore voxels to the total number of voxels.

The *absolute permeability* is determined using the lattice Boltzmann method (LBM), which simulates viscous fluid flow in the pore space. LBM models the fluid as consisting of fictitious particles (mass fractions), unlike traditional computational fluid dynamics methods which numerically solve the conservation equations of mass, momentum, and energy. These particles propagate and collide on a regular lattice. In

60

the collision, the mass fractions are modified in such a way that mass and momentum are conserved and correct the relation between strain rate tensor and stresses, as used in the Navier-Stokes equations. Arguably, the paramount feature of LBM is that it does not require any idealization of the pore space, but rather simulates viscous fluid dynamics in a real pore space that we obtain from segmenting the CT-scan images. The LBM code we use for fluid flow simulation was developed and described in detail by Keehm (2003). This simulation produces the total volumetric fluid flux through a sample in response to the applied pressure difference. The absolute permeability is the ratio of these two values normalized by the fluid's viscosity, the sample's length and its cross-sectional area.

The *electrical conductivity* at full water saturation and the corresponding formation factor are computed as a solution of the Laplace equation with charge-conservation boundary conditions using a conjugate gradient technique (Arns, et al., 2001). The three-dimensional voxel structure is first converted into a discretized conductive medium by assigning conductivity values to each voxel. A potential difference is applied diagonally across the sample and the system is relaxed using the conjugate gradient technique to evaluate the field. This method was implemented in the finite-element (FEM) code by Martys and Garboczi (1992). In our application of this FEM code, the mineral conductivity is set to zero, the water conductivity σ_w is 1 Siemens/m. The formation factor F is simply calculated as the ratio of the conductivity of water to that of the sample: $F = \sigma_t / \sigma_w$

4.5 RESULTS

As mentioned earlier in section 4.3, for each group of same-sized subsamples, we randomly select a certain number of subsamples depending upon their relative sizes. The numbers of subsamples randomly selected for each size group for the three samples are summarized in Table 4.2, 4.3, and 4.4.

Table 4.2. The number of subsamples in each group of same-sized subsamples for the Fontainebleau Sandstone sample. All these subsamples were randomly selected from a $600 \times 600 \times 800$ binary cube.

Subsample Size (Pixels)	Subsample Size (mm)	Subsample Size (autocorrelation range)	Number of subsamples
$300 \times 300 \times 300$	0.702×0.702×0.702	10 a	5
$200 \times 200 \times 200$	0.468×0.468×0.468	7.5 a	10
$150 \times 150 \times 150$	0.351×0.351×0.351	5 a	10
$100 \times 100 \times 100$	0.234×0.234×0.234	3 a	20
$75 \times 75 \times 75$	0.175×0.175×0.175	1.75 a	100
$50 \times 50 \times 50$	0.11×0.11×0.11	1.5 a	1000

Table 4.3. The number of subsamples in each group of same-sized subsamples for the Pomponio Beach sample. All these subsamples were randomly selected from a 625 ×625 ×522 binary cube.

Subsample Size (Pixels)	Subsample Size (mm)	Subsample Size (autocorrelation range)	Number of subsamples
170 ×170 ×170	2.5×2.5×2.5	10 *a*	10
150 ×150 ×150	2.2×2.2×2.2	8.8 *a*	10
100 ×100 ×100	1.5×1.5×1.5	6 *a*	25
50 ×50 ×50	0.74×0.74×0.74	3 *a*	100
25 ×25 ×25	0.37×0.37×0.37	1.5 *a*	1000

Table 4.4. The number of subsamples in each group of same-sized subsamples for the San Gregorio sample. All these subsamples were randomly selected from a 625 ×625 ×522 binary cube.

Subsample Size (Pixels)	Subsample Size (mm)	Subsample Size (autocorrelation range)	Number of subsamples
150 ×150 ×150	2.2×2.2×2.2	10 *a*	10
100 ×100 ×100	1.5×1.5×1.5	6 *a*	25
50 ×50 ×50	0.74×0.74×0.74	3 *a*	100
25 ×25 ×25	0.37×0.37×0.37	1.5 *a*	1000

By reducing the size of subsamples we drastically expand the porosity range these subsamples cover. This is illustrated in Figure 4.3, 4.4, and 4.5 where the mean porosities and their standard deviations are plotted for each group of the same-sized subsamples for each sample, respectively. In each case, the mean porosity of these groups oscillates around the laboratory value. At the same time, for all the samples

the variance increases with the decreasing subsample size.
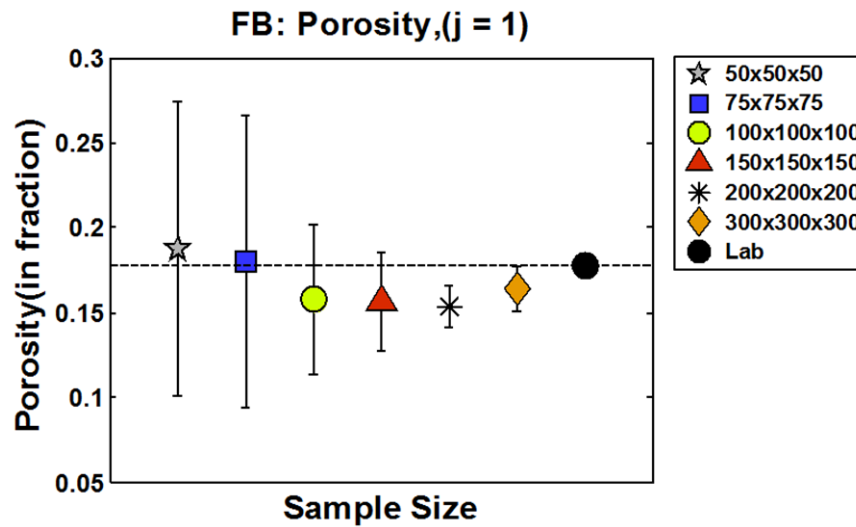
Figure 4.3. Porosity means and corresponding standard deviations (vertical bars) for six groups of the same-sized Fontainebleau subsamples. The symbol on the far right is from laboratory measurement on the actual physical sample.
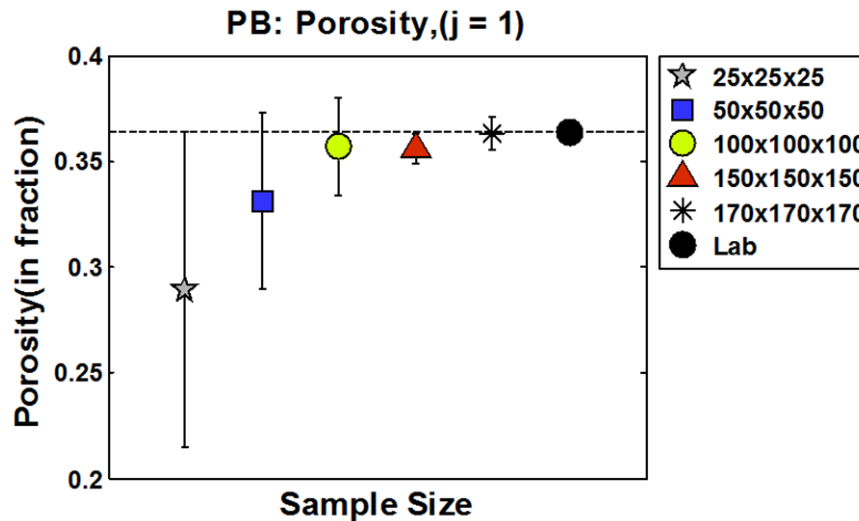
Figure 4.4. Porosity means and corresponding standard deviations (vertical bars) for five groups of the same-sized Pomponio Beach subsamples. The black circle on the far right is from laboratory measurement on the actual physical sample.
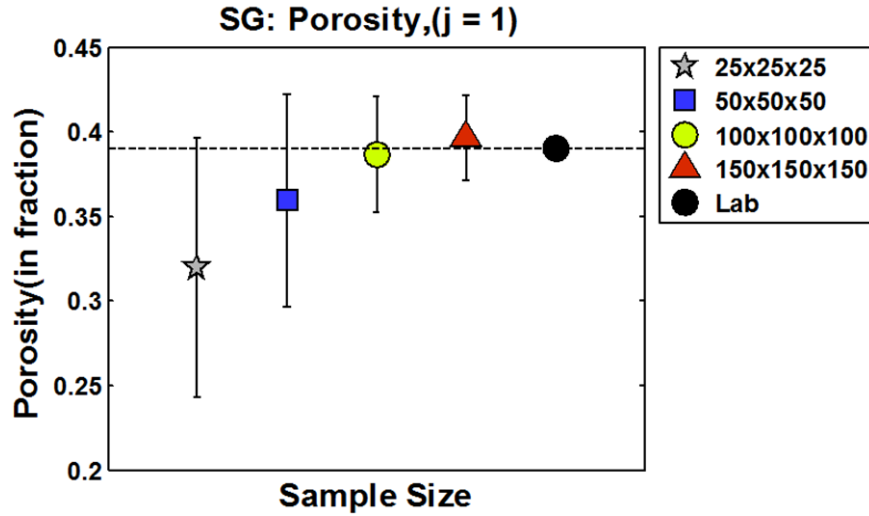
Figure 4.5. Porosity means and corresponding standard deviations (vertical bars) for four groups of the same-sized San Gregorio subsamples. The black circle on the far right is from laboratory measurement on the actual physical sample.

Permeability and formation factor are calculated using the simulations described in section 4.4, for all the subsamples. The mean permeability and formation factor are obtained using power averaging method as given by

$$\overline{X} = \left(\frac{\sum X_i^{j}}{N} \right)^{1/j},$$ (4.4)

where X can be k or F, N is total number of subsamples and j is the power averaging exponent. The means are calculated for six different values of j (1, -1, 0.5, -0.5, 2 and -2), as shown in Figures 4.6, 4.8, and 4.10 for absolute permeability and 4.7, 4.9, and 4.11 for formation factor for the three samples. The error bars in each case represent the standard deviation of the data around each mean. Note that when $j = 1$ the power average is equivalent to arithmetic average, while when $j = -1$ it is equivalent to harmonic average. We compare these power averages to the laboratory

measurements of the sample. However, we do not have a laboratory electrical measurement for the two artificial samples, so we do not have any criteria for evaluating the efficiency of any of the methods for formation factor for the two samples.
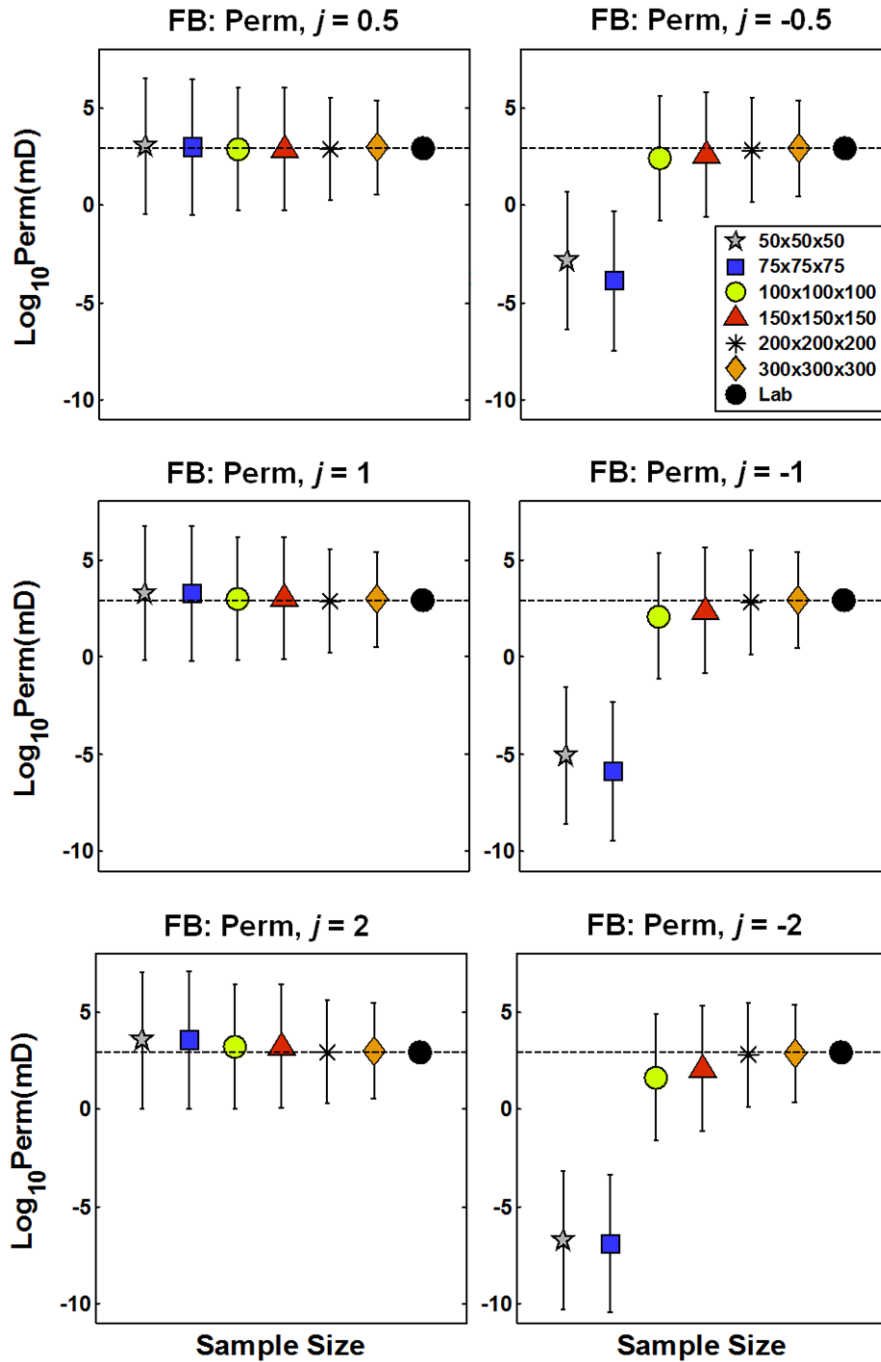
Figure 4.6. Permeability means and corresponding standard deviations (vertical bars) for six groups of the same-sized FB subsamples. The black circle is the laboratory measurement on the actual physical sample. The horizontal dashed line is drawn through the laboratory measured data.
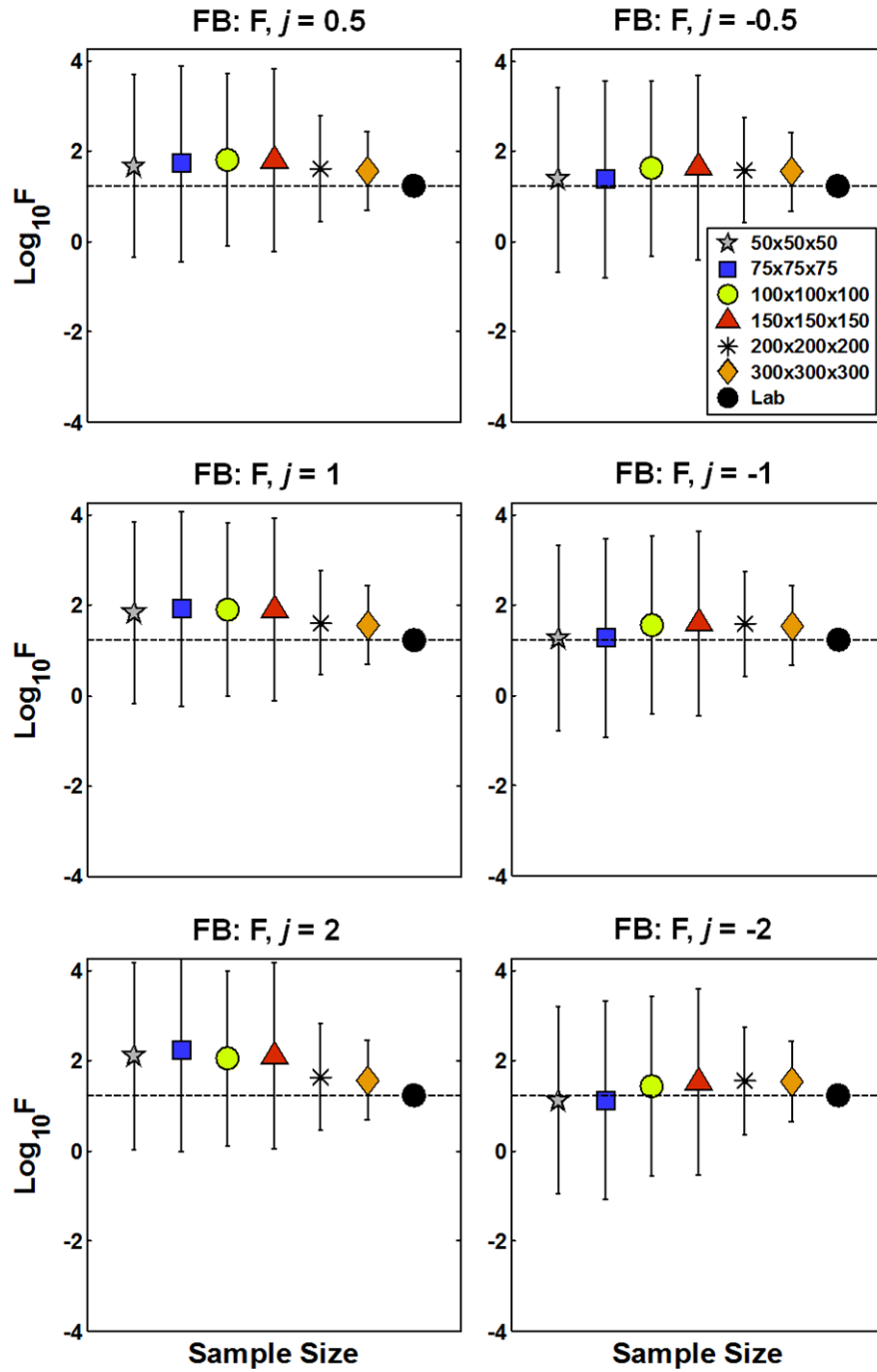
Figure 4.7. Formation factor means and corresponding standard deviations (vertical bars) for six groups of the same-sized FB subsamples. The black circle on the far right is from laboratory measurement on the actual physical sample. The horizontal dashed line is drawn through the laboratory measured data.
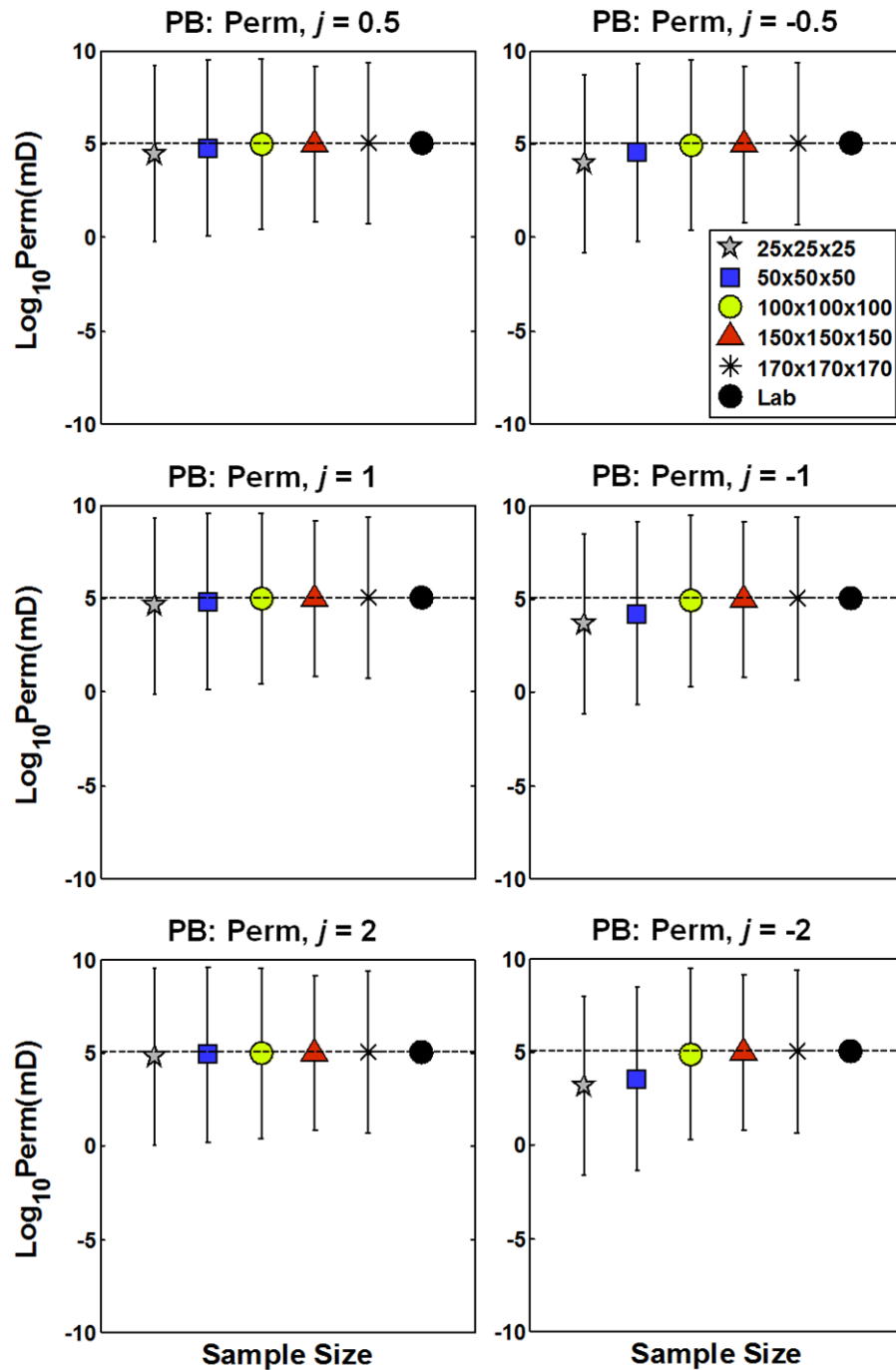
Figure 4.8. Permeability means and corresponding standard deviations (vertical bars) for five groups of the same-sized PB subsamples. The black circle on the far right is from laboratory measurement on the actual physical sample. The horizontal dashed line is drawn through the laboratory measured data.
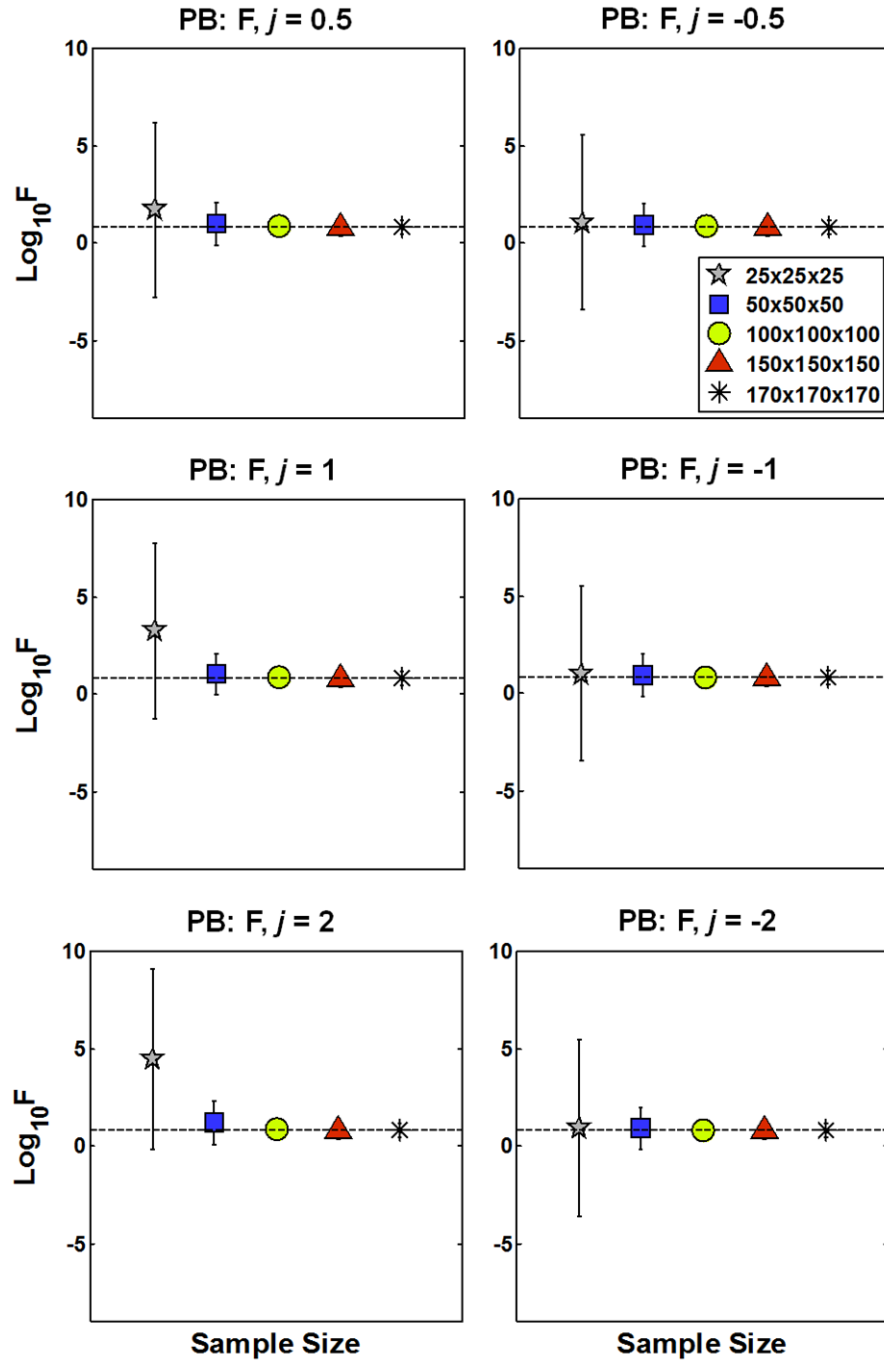
Figure 4.9. Formation factor means and corresponding standard deviations (vertical bars) for five groups of the same-sized PB subsamples. No laboratory data was available for the formation factor. The horizontal dashed line is drawn through the mean of the largest sized group.
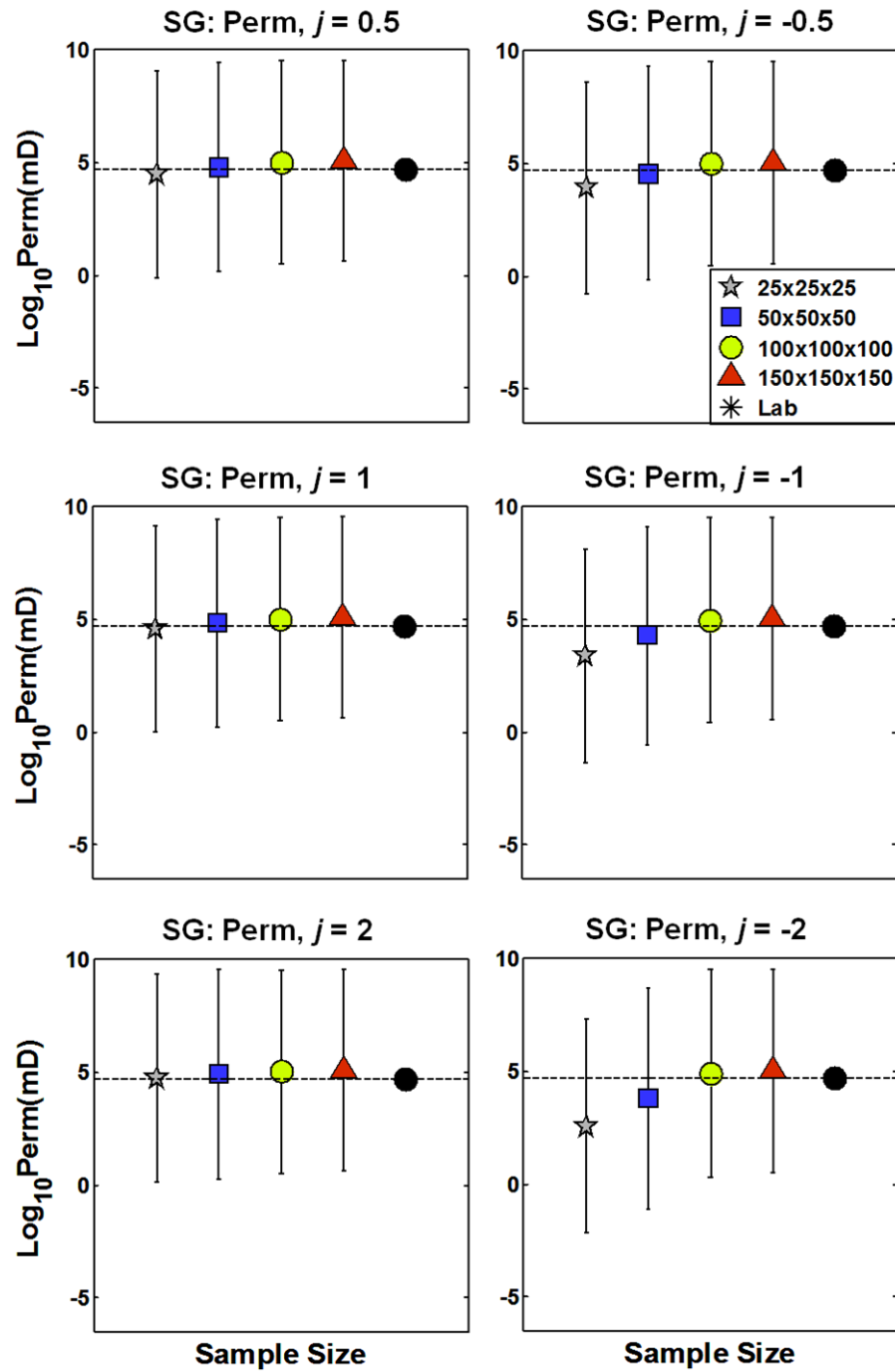
Figure 4.10. Permeability means and corresponding standard deviations (vertical bars) for four groups of the same-sized SG subsamples. The black circle on the far right is from laboratory measurement on the actual physical sample. The horizontal dashed line is drawn through the laboratory measured data.
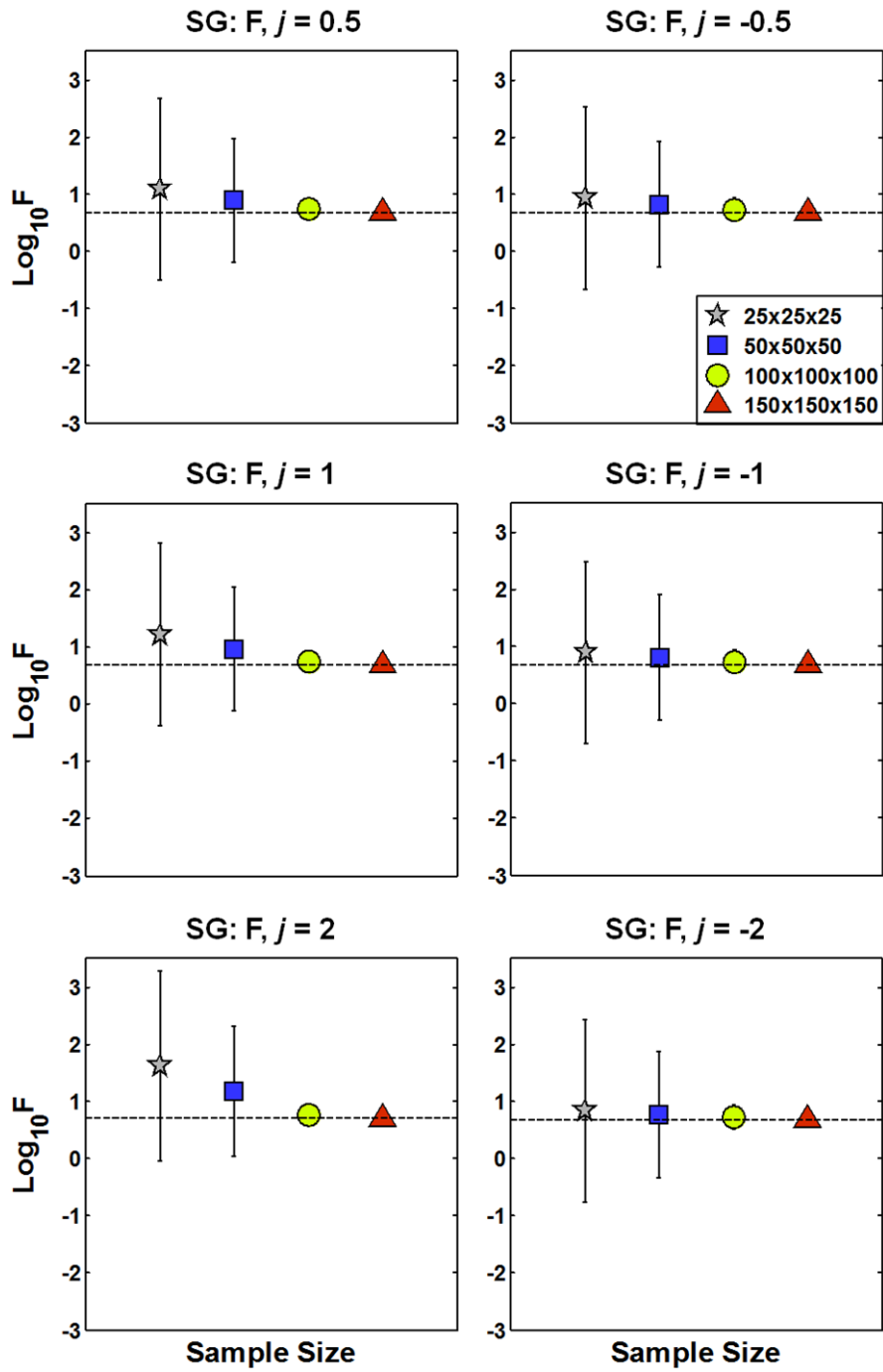
Figure 4.11. Formation factor means and corresponding standard deviations (vertical bars) for four groups of the same-sized SG subsamples. No laboratory data was available for the formation factor. The horizontal dashed line is drawn through the mean of the largest sized group.

Note that we have logarithmic scale in all these figures (Figures 4.7 to 4.11),

which means that the differences in the means of computed permeability and formation factor for different groups of same-sized samples and the laboratory measurement are not evident in these figures. Hence to compare these differences, we next calculate the relative errors of the means of each group of same-sized subsamples, with respect to their laboratory measurements. It is calculated as

$$Err = \frac{\left| \overline{X} - L \right|}{L}, \tag{4.5}$$

where $\overline{X}$ is the mean of a property (permeability or formation factor) of the group of same-sized subsamples, and L is the laboratory measured property value. Figure 4.12, 4.13, and 4.14 respectively show the relative errors for the Fontainebleau, Pomponio Beach, and San Gregorio samples.   As mentioned earlier, we have laboratory measured formation factor value only for the Fontainebleau samples. Hence, we cannot calculate the relative error associated with the formation factor of the Pomponio Beach and San Gregorio samples.
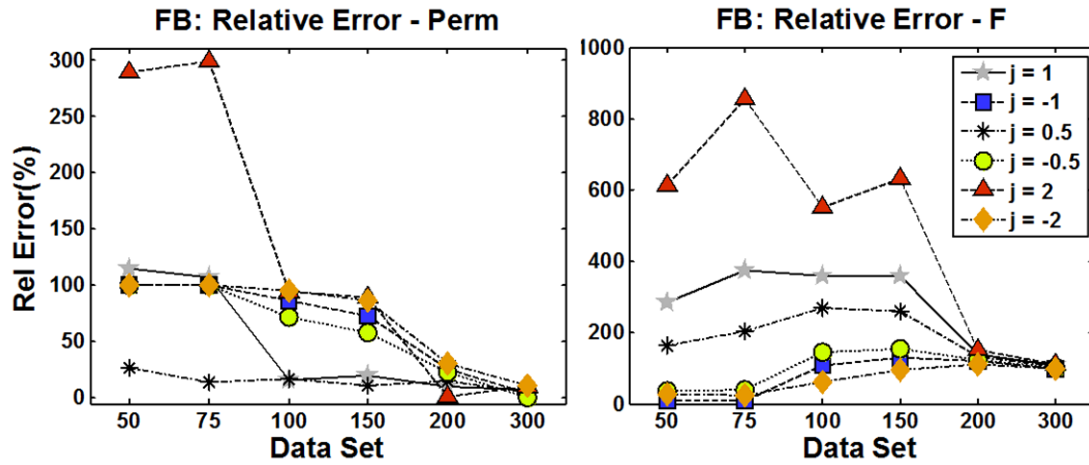
Figure 4.12. The relative error in the permeability and the formation factor estimation using different averaging methods for the Fontainebleau sample. The horizontal axis in all these plots is the size of the subsamples used, given in pixels.
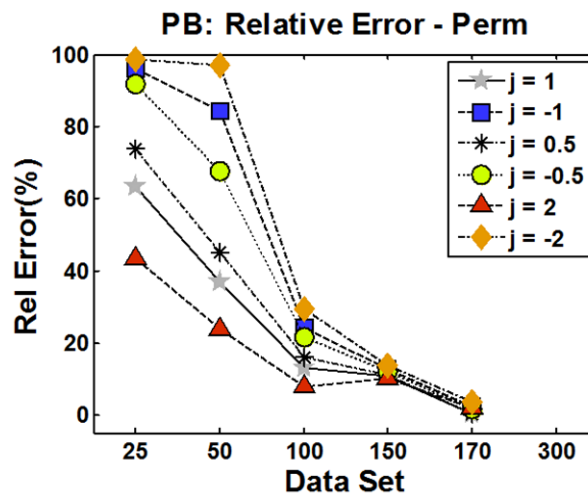
Figure 4.13. The relative error in permeability estimation using different averaging methods for the Pomponio Beach sample. The horizontal axis represents subsample sizes.
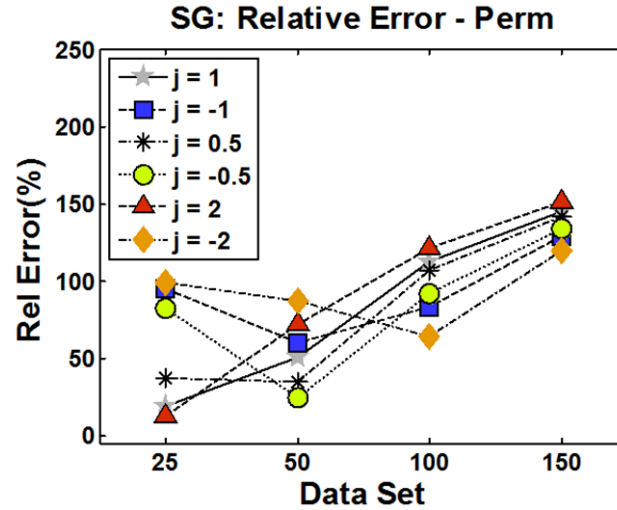
Figure 4.14. The relative error in permeability estimation using different averaging methods for the San Gregorio sample. The horizontal axis represents subsample sizes.

In these figures, we observe high relative errors for all of the samples, which indicates that none of these averaging methods give a mean closer to the laboratory measurement for any of the subsample sizes. This shows that we cannot use the subsamples at REV size or below to predict the permeability and formation factor at a larger scale. However, both these rock properties form trends if plotted versus porosity (Figure 4.15, 4.17, and 4. 19 for permeability; and Figures 4.16, 4.18, and 4.20 for formation factor). Note that in these figures we are plotting the computed porosity, permeability, and formation factor data for different subsample sizes and not their means or standard deviations.

We plot the experimental physical trends measured in the lab for the Fontainebleau sample (Figures 4.15 and 4.16) along with the computed data for various subsample sizes. We obtain similar trends for the Pomponio Beach and San Gregorio sands (Figures 4.17 to 4.20). For the Pomponio Beach and San Gregorio samples, however, we only have one measured value for porosity and permeability,

and no measured laboratory data for formation factor. Therefore, we cannot present a laboratory-measured trend for these samples. Instead, we display theoretical relations of Kozeny-Carman (Carman, 1937) and Archie (1942), respectively.

The Kozeny-Carman permeability is calculated using the following formula:

$$K = \frac{B \times d^2 \times \phi^3}{(1-\phi)^2},$$

(4.6)

where the permeability is in mD; B is the geometric factor (here we used $B = 5$ for both the samples); d is the grain size (microns); and ϕ is the porosity (fraction). The grain size of the PB and SG samples was measured by Kameda (2005) using sieve and laser particle size analysis (Table 3.2).

Archie's equation is

$$F = a\phi^{-m},$$

(4.7)

where a is a constant, m is the cementation constant, and ϕ is the porosity. Here, following Gomez (2009), we use $a = 1$, and three different values of $m = 1.6$, 1.8, and 2.0 for all the samples.

The computed subsample trends are qualitatively close to experimental physical trends measured in the laboratory for the Fontainebleau sample (Figures 4.15 and 4.16). For the Pomponio Beach and San Gregorio samples, on the other hand, we observe a qualitative consistency in the trends for different subsample sizes. Even though the range of the sampling scale in these two samples is not as large as in case of the Fontainebleau sandstone (from laboratory to micron scale), the relations between these physical properties across different subsample sizes are consistent.

This shows that computational rock physics can be used to create a physical trend between rock properties by moving below the REV. The key here is to focus on trends between values rather than on the values themselves.
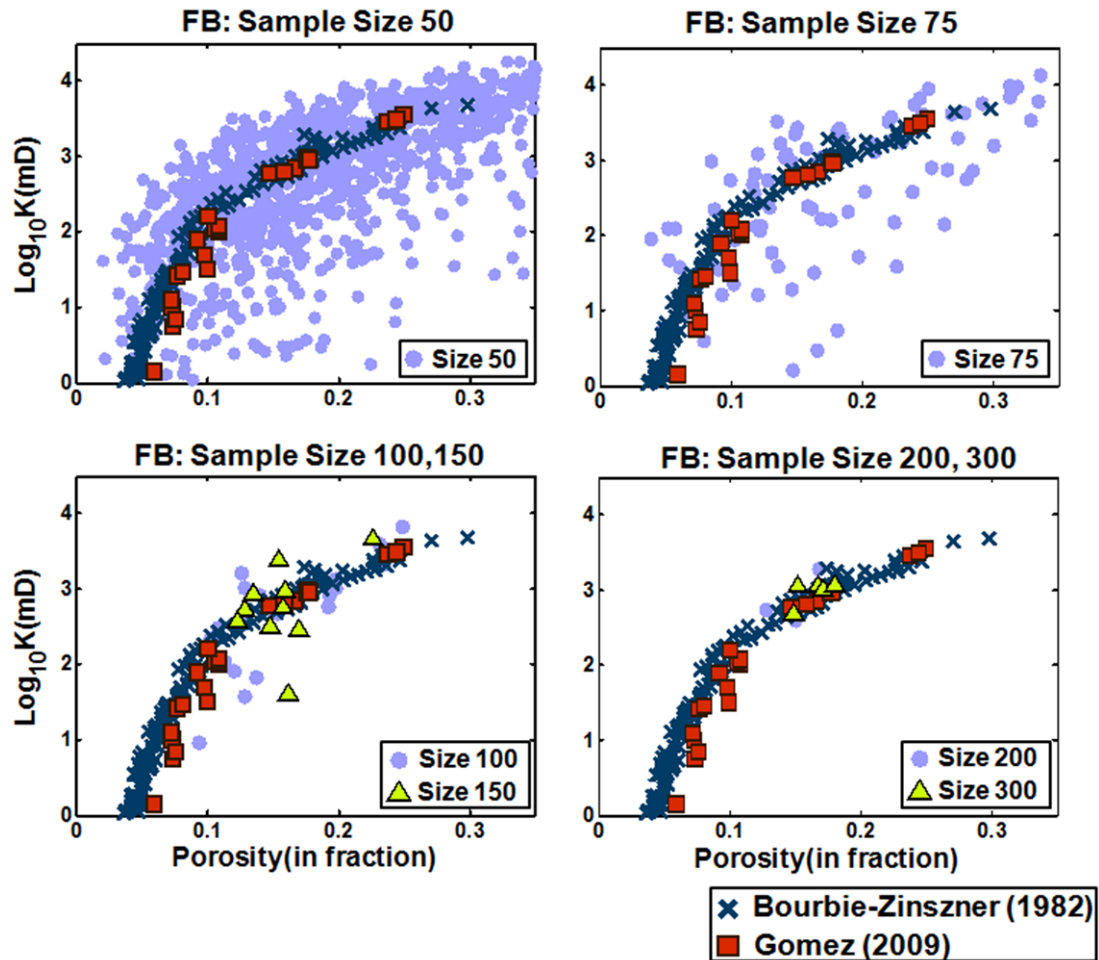
Figure 4.15. Permeability versus porosity for the Fontainebleau sandstone. Our computational results are plotted for a varying size of the subsamples. Blue crosses are from the classical dataset by Bourbie and Zinszner (1985) while red squares are from Gomez (2009).
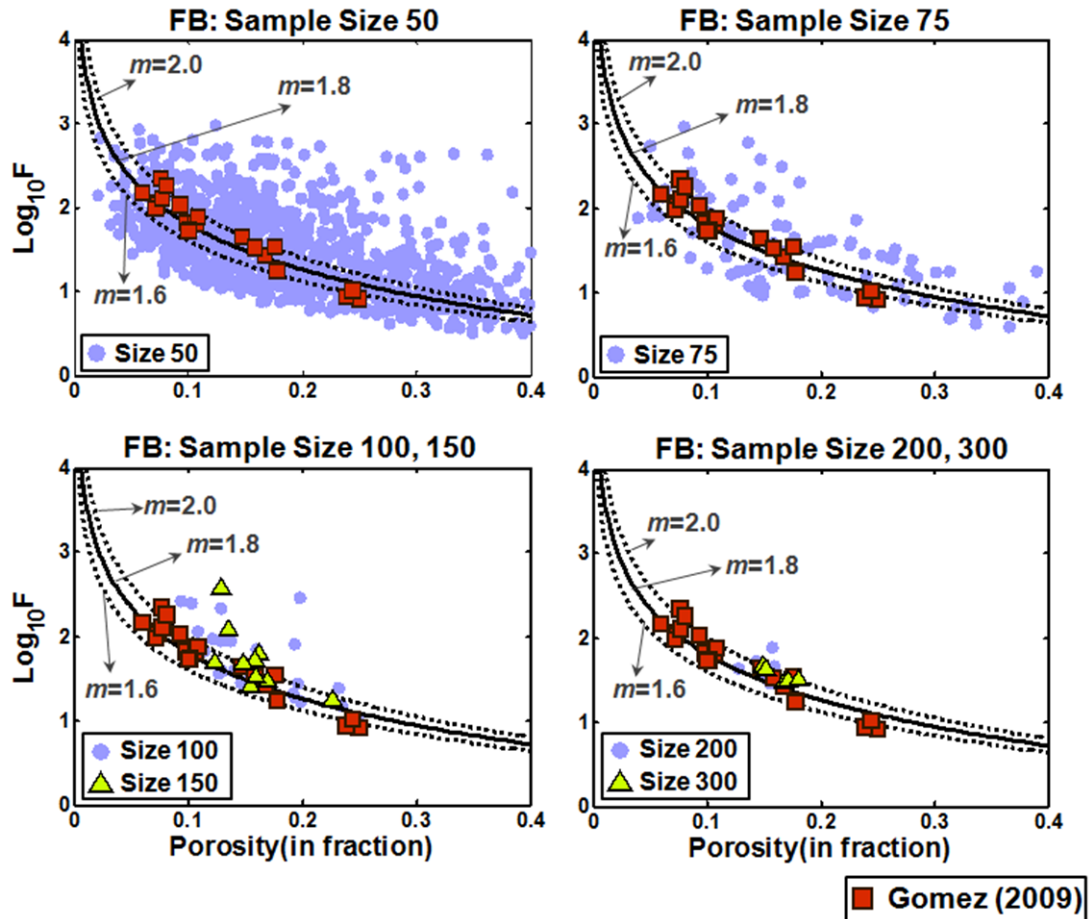
Figure 4.16. Formation factor versus porosity for the Fontainebleau sandstone. Our computational results are plotted for a varying size of the subsamples. Red squares are the data from Gomez (2009). The solid and dashed lines represent the Archie equation for $a = 1$, and varying $m = 1.6$, 1.8, and 2.0, as indicated.
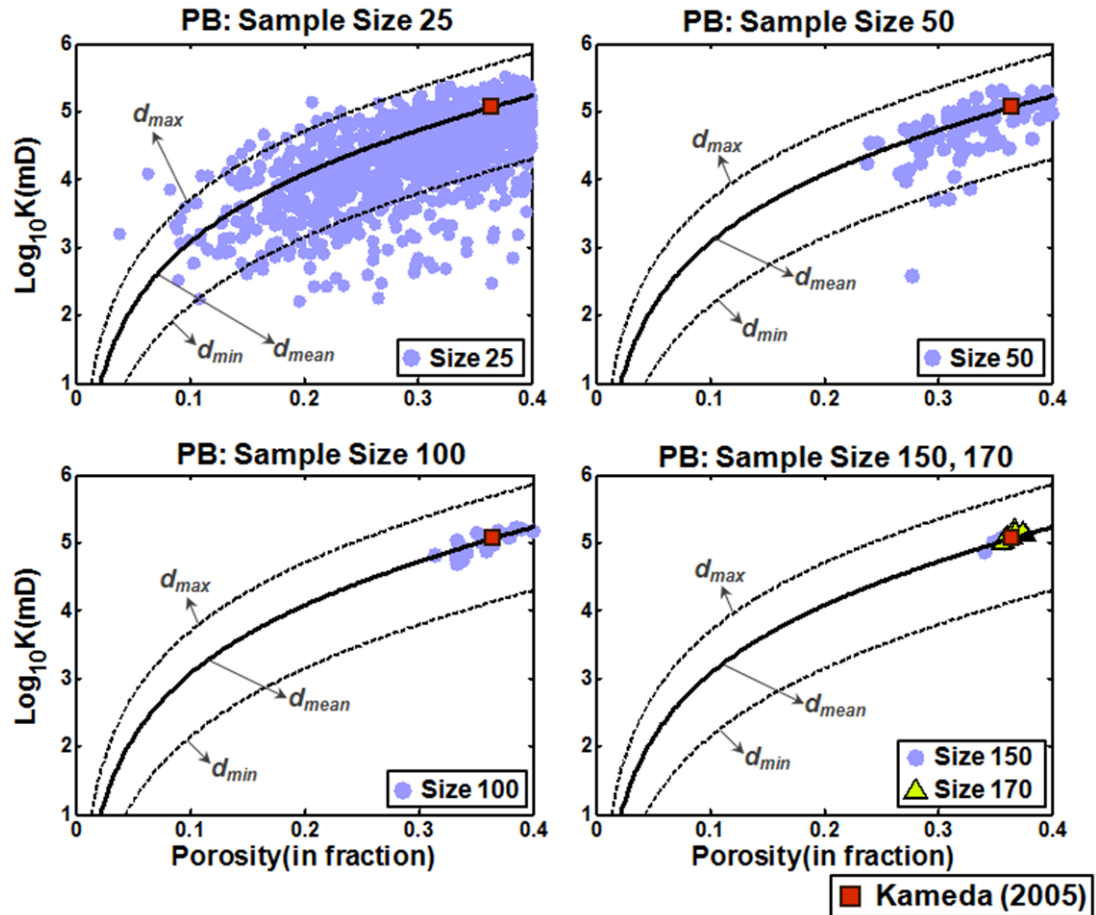
Figure 4.17. Permeability versus porosity for the Pomponio Beach sand. Our computational results are plotted for a varying size of the subsamples. The red square in each of the plot represents the laboratory measurement (Kameda, 2005). Kozeny-Carman trends are plotted for comparison. These permeability-porosity curves are calculated using Equation 4.6 for *B*=5, and three different grain sizes: mean grain size, *dmean* = 437 micron; minimum grain size, *dmin* = 150 micron; and maximum grain size, *dmax* = 900 micron, as reported by Kameda (2005).
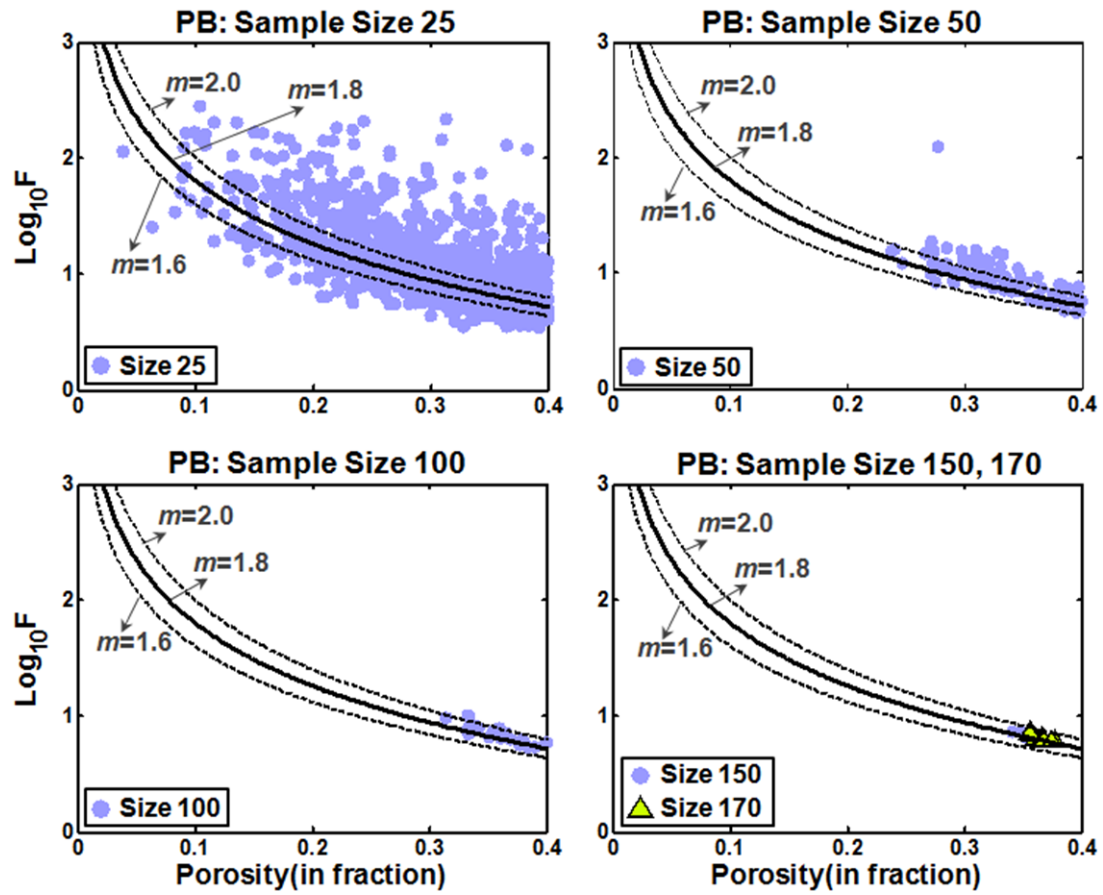
Figure 4.18. Formation factor versus porosity for the Pomponio Beach. Our computational results are plotted for a varying size of the subsamples. No laboratory measurement for the formation factor was available for this sample. Archie's relations for $a = 1$, and varying $m = 1.6$, 1.8, and 2.0 (as indicated) are plotted for comparison.
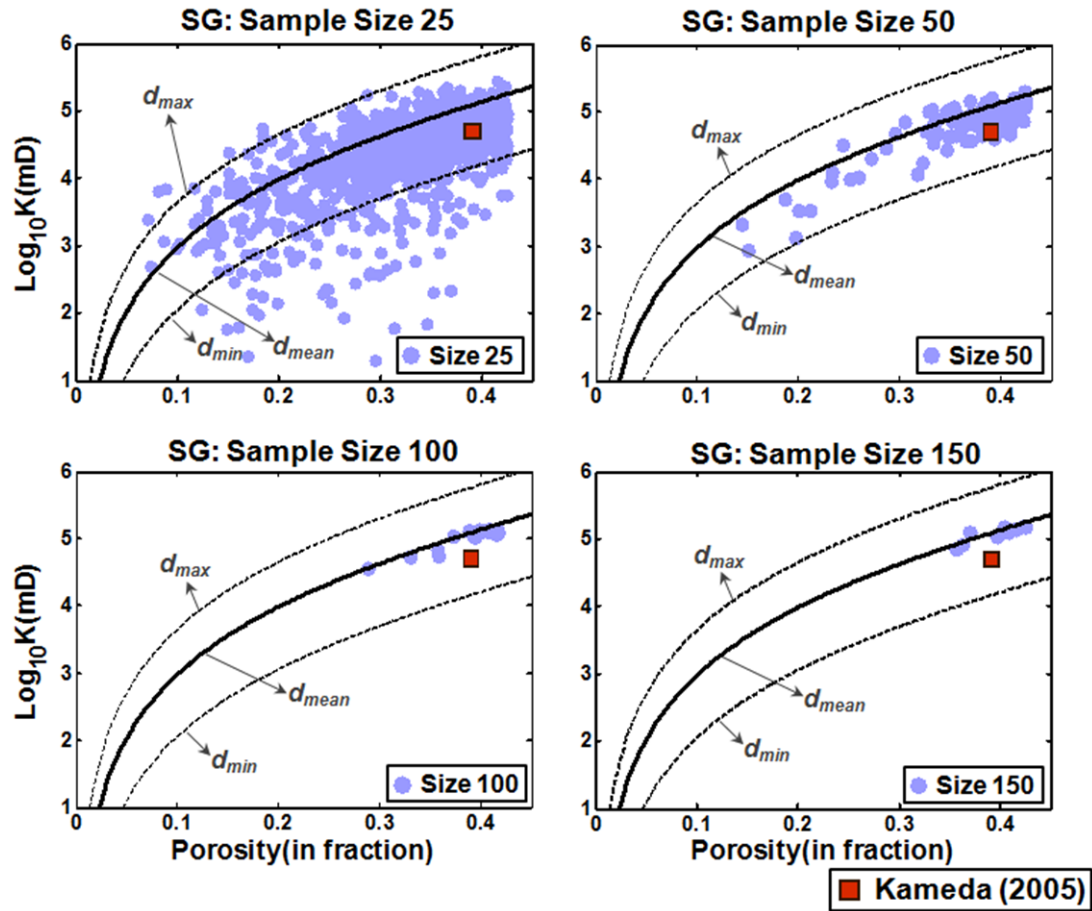
Figure 4.19. Permeability versus porosity for the San Gregorio sand. Our computational results are plotted for a varying size of the subsamples. The red square in each of the plot represents the laboratory measurement (Kameda, 2005). Kozeny-Carman trends are plotted for comparison. These permeability-porosity curves are calculated using Equation 4.6 for *B*=5, and three different grain sizes: mean grain size, *dmean* = 392 micron; minimum grain size, *dmin* = 135 micron; and maximum grain size, *dmax* = 850 micron, as reported by Kameda (2005).
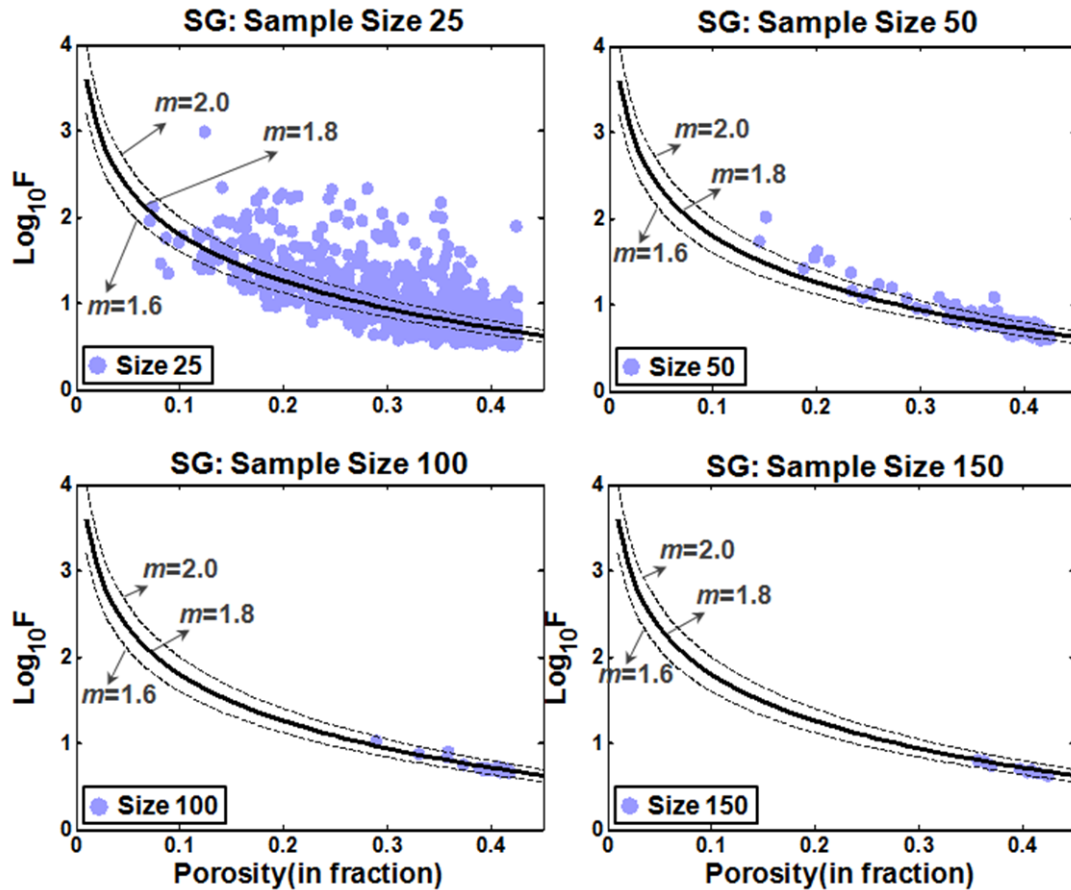
Figure 4.20. Formation factor versus porosity for the San Gregorio sand. Our computational results are plotted for a varying size of the subsamples. No laboratory measurement for the formation factor was available for this sample. Archie's relations for $a = 1$, and varying $m = 1.6$, 1.8, and 2.0 (as indicated) are plotted for comparison.

4.5 DISCUSSIONS

Although the computed subsample trends are close to either laboratory or theoretical trends, however the variance, which measures the scatter, in these trends increases as the sample size decreases. In other words, we observe large variances in permeability and formation factor at a fixed porosity value. This scatter is especially pronounced for the smallest subsample size which can make it difficult to discern a

unique trend. We reduce this large scatter by using moving porosity window power averaging method.

The porosity window power averaging method involves generating a small porosity window of fixed width, which is 0.003 or 0.3% here. We compute various power averages (Equation 4.4) for the permeability and formation factor of all the subsamples whose porosity fall into the window, and then plot it versus the arithmetic averaged porosity ($j = 1$) of the subsamples in the window. This window-based averaging produces a physically meaningful trend for permeability as well as for the formation factor from the smallest subsamples which are much smaller than the REV (Figures 4.21 to 4.27). The power averaging used here is in essence a data reduction method applied here to produce a reasonably tight trend.

We observe that among all the power averaging method explored here for the porosity-permeability trend, power averaging the permeability with $m = 1$ qualitatively gives the trend closest to the laboratory or theoretical trends amongst all the averaging techniques examined, while for porosity-formation factor trend, power averaging the formation factor with $j = -1$ qualitatively gives the closest results for all the samples. Note that while permeability is a measure of the fluid flow, the electrical formation factor is a measure of resistance to the electrical flow. This explains the inverse relation of the best averaging methods for the two properties.
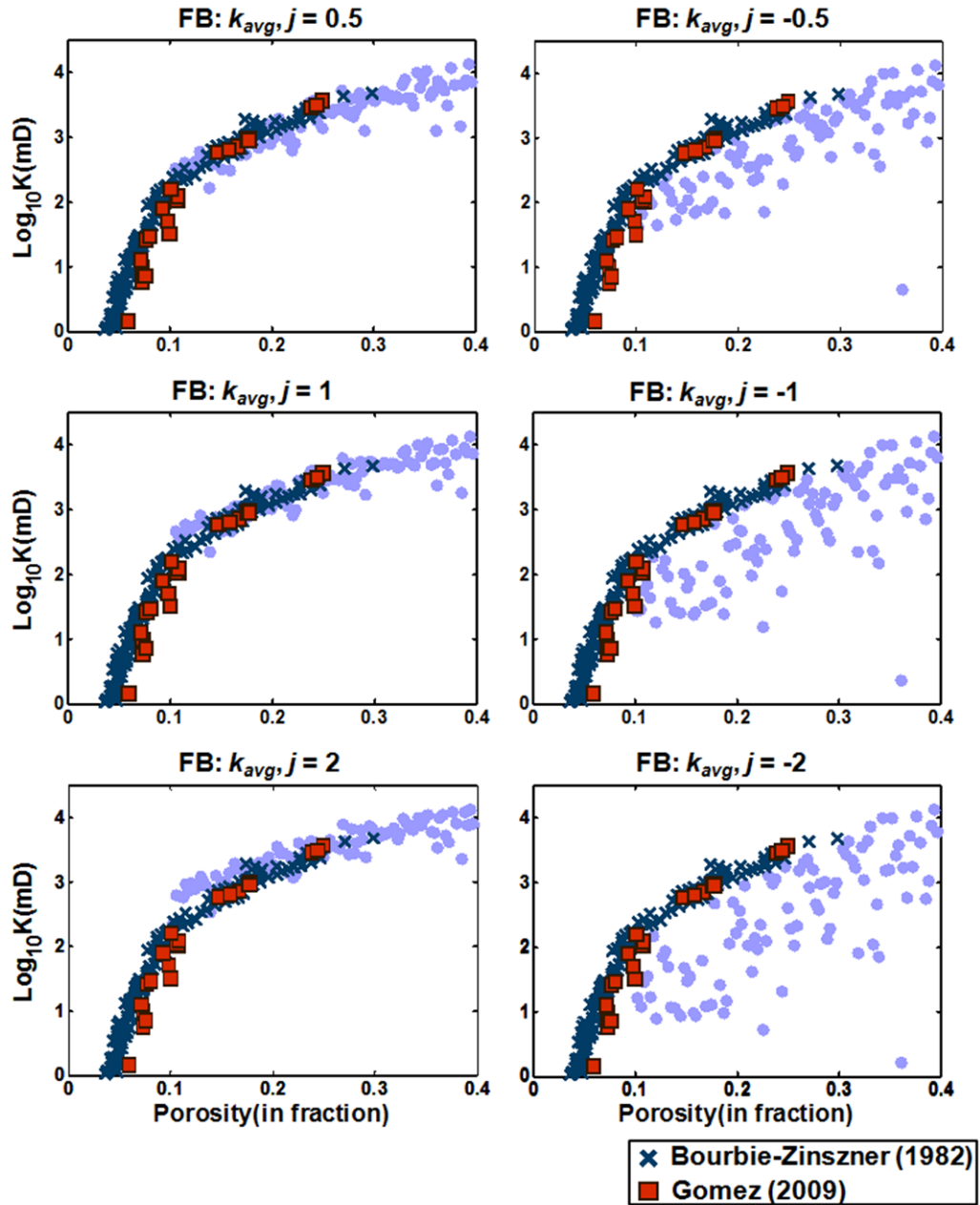
Figure 4.21. Permeability versus porosity for the Fontainebleau sandstone. The moving-window data reduction (described in the text) of permeability and porosity for one thousand 50×50×50 subsamples are plotted as light blue circles. Blue crosses are from the classical dataset by Bourbie and Zinszner (1985) while red squares are laboratory measurements by Gomez (2009).
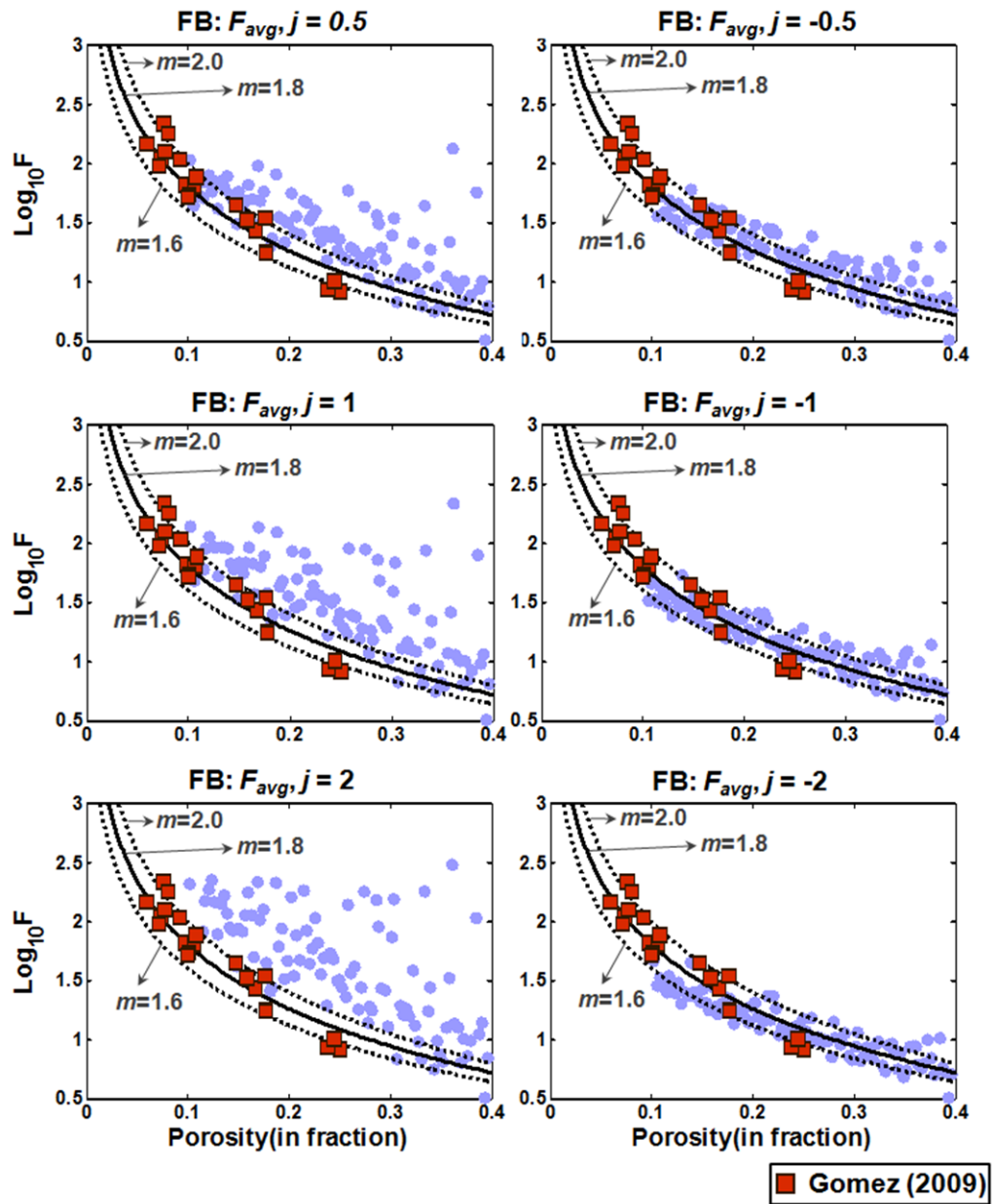
Figure 4.22. Formation factor versus porosity for the Fontainebleau sandstone. The moving average of formation factor and porosity for one thousand 50×50×50 subsamples are plotted as light blue circles. The solid and dashed lines represent the Archie equation for *a* =1, and varying *m* = 1.6, 1.8, and 2.0, as indicated.
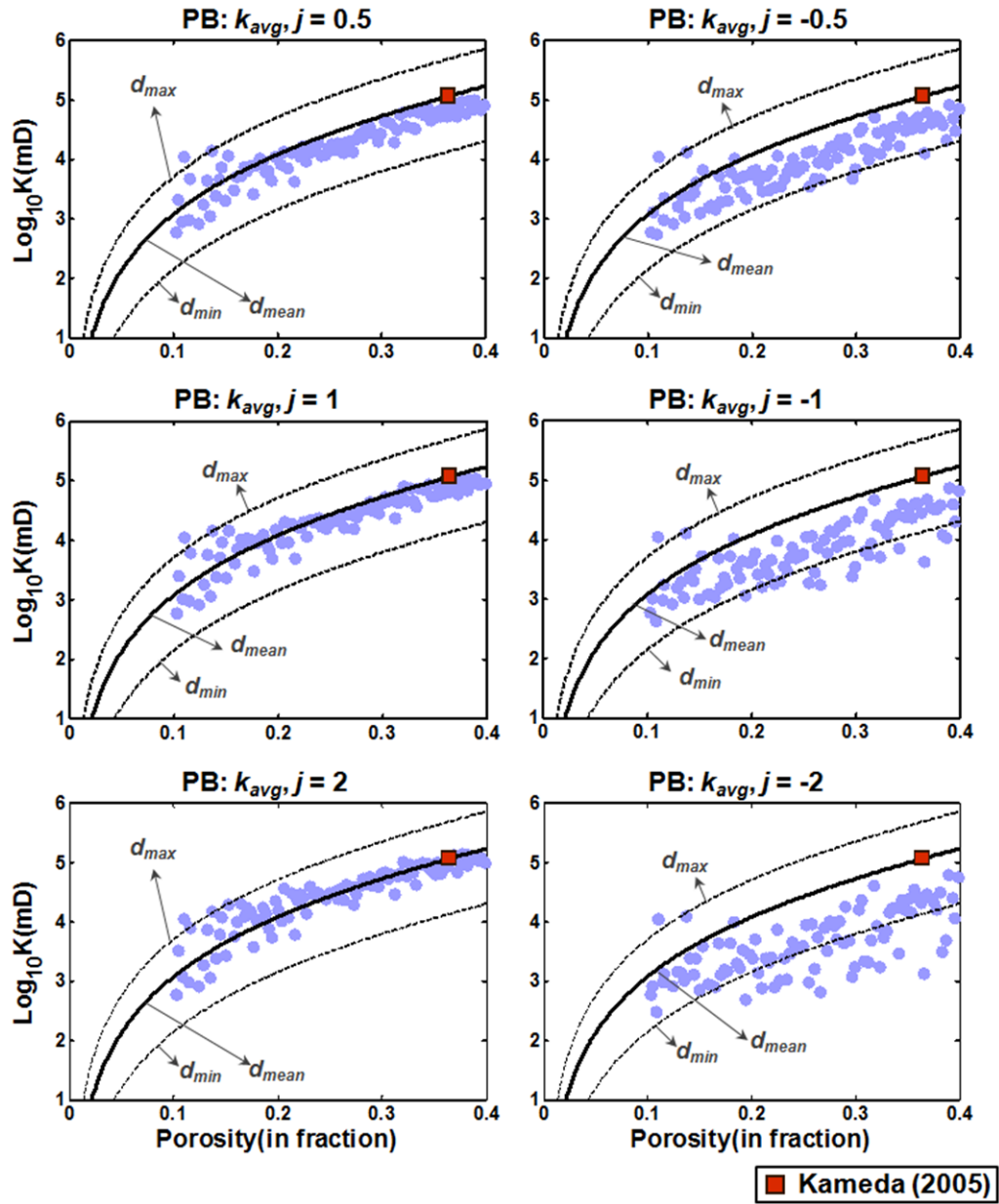
Figure 4.23. Permeability versus porosity for the Pomponio Beach sand. The moving average of permeability and porosity for one thousand 25×25×25 subsamples are plotted as blue circles. The red square is the laboratory measurement for the sample. The solid line and the dashed lines represent the Kozeny-Carman equation for different grain sizes (minimum, *dmin*; maximum, *dmax*; and mean, *dmean*) as indicated.
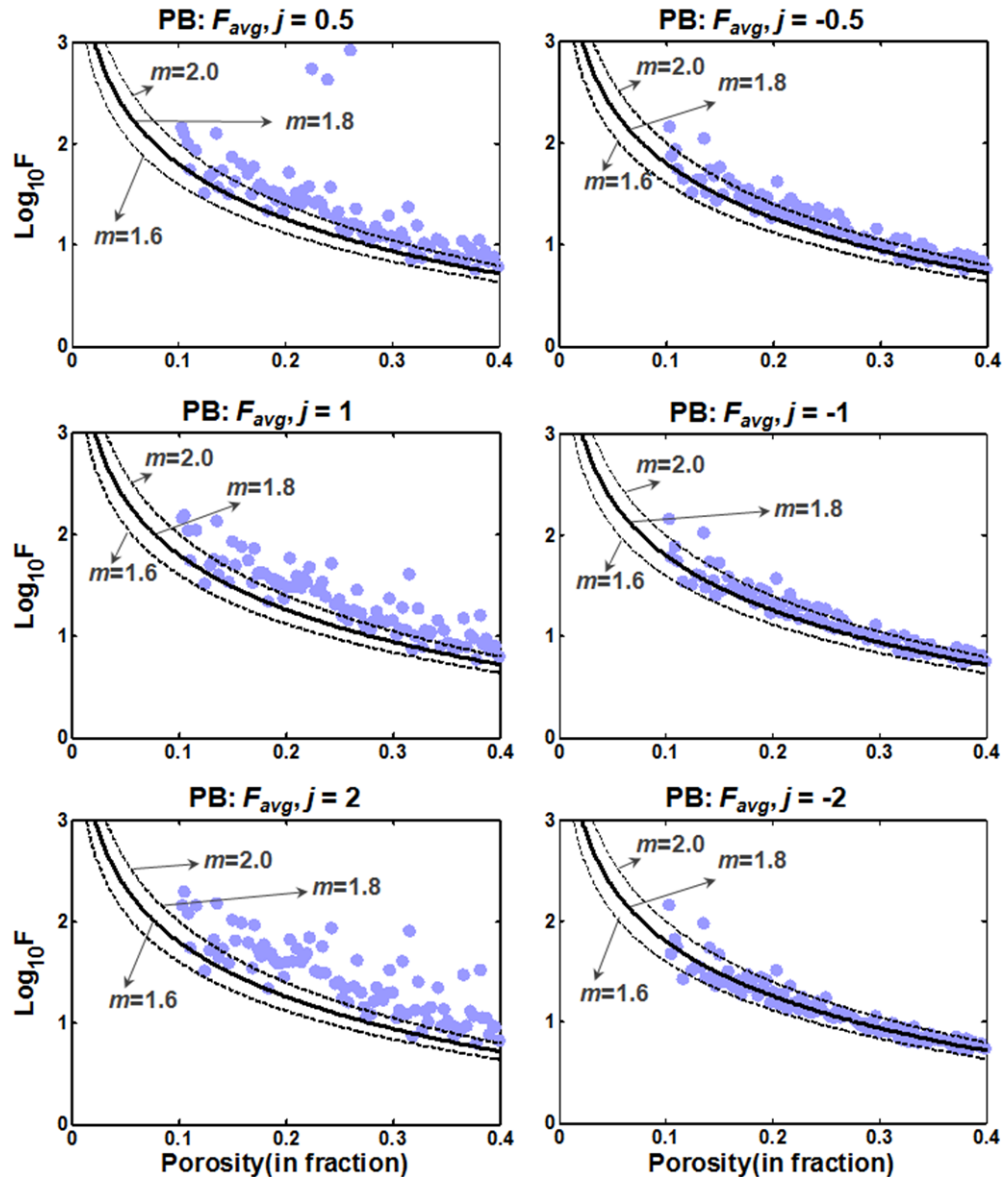
Figure 4.24. Formation factor versus porosity for the Pomponio Beach. The moving average of formation factor and porosity for one thousand $25\times25\times25$ subsamples are plotted as light blue circles. The solid and dashed lines represent the Archie equation for $a = 1$, and varying $m = 1.6$, 1.8, and 2.0, as indicated.
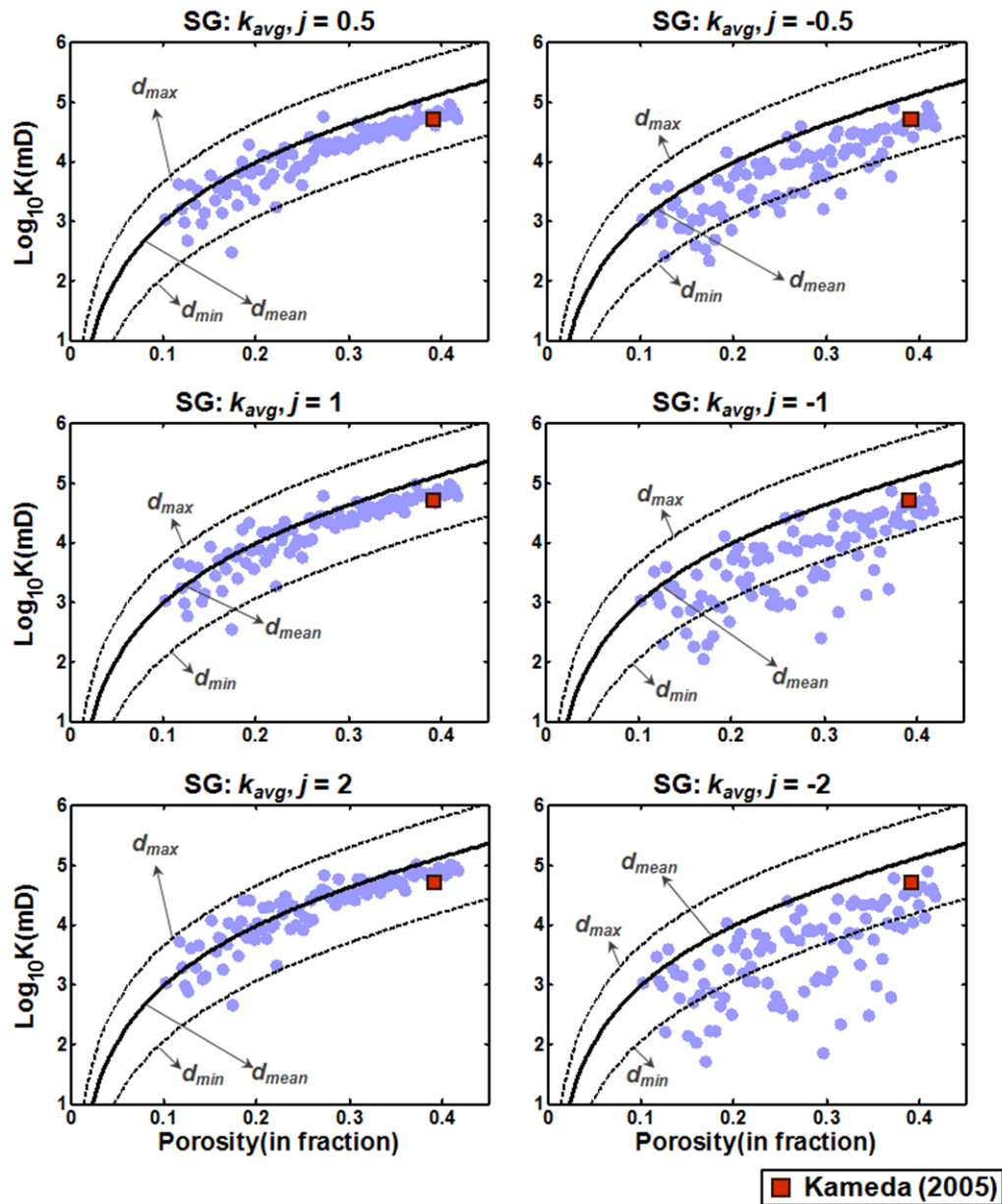
Figure 4.25. Permeability versus porosity for the San Gregorio sand. The moving average of permeability and porosity for one thousand 25×25×25 subsamples are plotted as blue circles. The red square is the laboratory measurement for the sample. The solid line and the dashed lines represent the Kozeny-Carman equation for different grain sizes (minimum, *dmin*; maximum, *dmax*; and mean, *dmean*) as indicated.
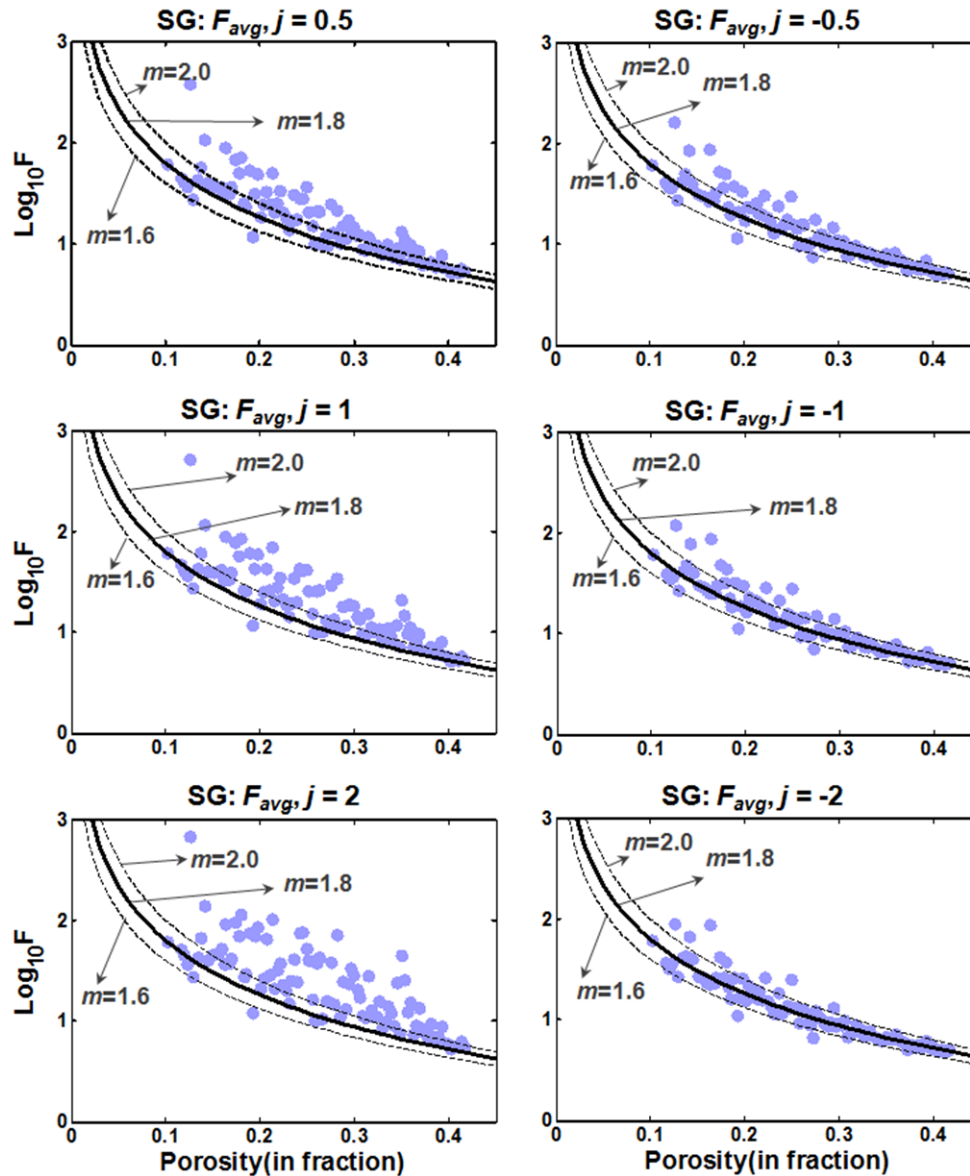
Figure 4.26. Formation factor versus porosity for the San Gregorio sand. The moving average of formation factor and porosity for one thousand 25×25×25 subsamples are plotted as light blue circles. The solid and dashed lines represent the Archie equation for $a = 1$, and varying $m = 1.6$, 1.8, and 2.0, as indicated.

4.6 CONCLUSIONS

We observe that even though the absolute values of porosity, permeability, and

formation factor vary as we decrease the sample size below the traditional REV size; the trends between porosity-permeability and porosity-electrical formation factor remain qualitatively consistent across the scale. The variance in the simulated measurements increases as we decrease the sample size, and hence obtaining a meaningful relation from the smallest subsample size becomes difficult. We overcome this problem by averaging these measurements using different power-averaging methods in a moving porosity window.

These results imply that, we can obtain physically meaningful trend from the samples below the traditional REV size. In fact, by using the small size samples we span a larger portion of the trend as compared to REV size sample, providing the Geophysicists a better trend to work with. Another advantage of using smaller size sample is that they are computationally inexpensive and hence, are faster to process.

Our analysis is not exhaustive. For example, our range of scale varies only from core scale to micro-pore structure scale. It will be interesting to explore scales beyond the core scale. Also, the samples used in this study are fairly homogeneous. Another interesting research path would involve testing this result for wider variety of rocks. However, these analyses are beyond the scope of this chapter.

Chapter 5

Threshold Sweeping and Transport Properties Trends

5.1 ABSTRACT

A new method for obtaining a range of porosity, permeability, and formation factor using a single 3D CT scan image is introduced. It involves systematically varying the threshold of the 3D gray scale image to obtain slightly different 3D binary cube, and hence a different set of porosity, permeability, and formation factor values each time. This is called threshold sweeping. We examine the effect of threshold sweeping on the transport properties (porosity, permeability, and formation factor) and their trends. We observe that although the absolute values of transport properties change with threshold, the trends among them remains stable. This implies that physically meaningful trends between rock properties can be obtained just from a single 3D CT-scan by simply moving the gray-scale threshold. Further analysis of these different binary cubes reveals that the change in thresholds mimics the quartz

cementation in sandstone.

5.2 INTRODUCTION

In Chapter 3 we compared different image classification methods for converting 2D gray scale CT-scan slices to 2D binary slices and identified Otsu's (1979) thresholding method as the best method among them, which is then used to threshold all the 2D slices in 3D CT-scan image to produce 3D binary cube. We compute porosity (φ), permeability (k), and electrical formation factor (F) on this optimally classified binary 3D image (Chapter 4, section 4.4). However, if we shift the threshold from its optimum value and thus re-classify the original intensity cube, we can obtain a binary cube with different porosity, permeability, and formation factor. We can repeat this exercise for different threshold values around the optimum value and obtain a range of porosity, permeability, and formation factor for these 3D binary cubes. We call this procedure of using different thresholds to obtain different 3D binary images as *threshold sweeping*.

In this chapter we explore how the threshold sweeping affects the transport properties, porosity, permeability, and formation factor, and the trends among them, specifically porosity-permeability and porosity-formation-factor trends. In this study we use two artificial samples, Pomponio Beach (PB) and San Gregorio (SG), and a Fontainebleau sandstone sample (FB) as described in Chapter 3, section 3.3.

We observe that although all the transport properties vary as we change the threshold, the trends formed by them are stable and physically justifiable. Furthermore, we observe that the change in the binary images with threshold is

similar to the quartz overgrowth observed in the rocks.

The rest of the chapter is structured as follows. In section 5.3, we discuss the threshold sweeping methodology. In section 5.4, we present the results of the threshold sweeping. In section 5.5, we compare the 2D binary slices with different thresholds to the thin-sections of sandstone samples with quartz overgrowth, as well as with other theoretical studies. Finally, in section 5.6 we present our conclusions.

5.3 THRESHOLD SWEEPING

A threshold divides the intensity histogram of a CT scan image into two parts: pores (lower intensity pixels) and grains (higher intensity pixels) (Figure 5.1). As discussed earlier in Chapter 3, section 3.3, the intensity in the CT-scan image corresponds to the density of the material. Hence, the denser material, grains have higher intensity while the void space or the pores have lower intensity.
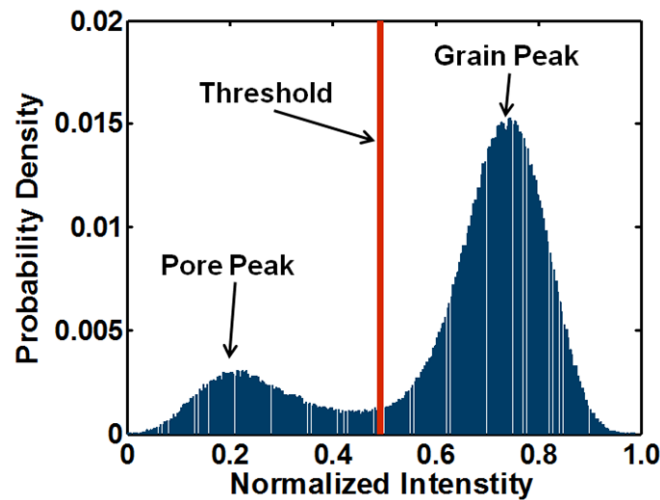
Figure 5.1. A typical intensity probability density function indicating the typical positions of grain and pore peaks.

In Chapter 3, we use Otsu's method to obtain an optimal threshold for each of the

2D slices in the 3D CT-scan images. This means that we have a different threshold for each slice in a sample. For each sandstone sample used in this study (FB, PB, and SG), we construct a histogram of these Otsu's thresholds for all the slices of the sample (Figure 5.2). These histograms show that the threshold values for different slices of a sample are very close to each other. For the Pomponio Beach (PB) and San Gregorio (SG) samples, in fact, thresholds for different slices converge to a single threshold value. The variation among the threshold values among individual slices is slightly more pronounced in the Fontainebleau (FB) case than in the other two cases. Still, even for the Fontainebleau, these thresholds fall with an interval of ten intensity units. Since the thresholds for different slices of a sample are so close to each other, instead of applying individual thresholds to 2D slices, we can apply a single threshold to all the slices to obtain the 3D binary image without changing the resultant 3D binary cube drastically, as long as this common single threshold is close to these individual threshold range. However, if we change this common single threshold value significantly, the resultant binary image will change considerably.
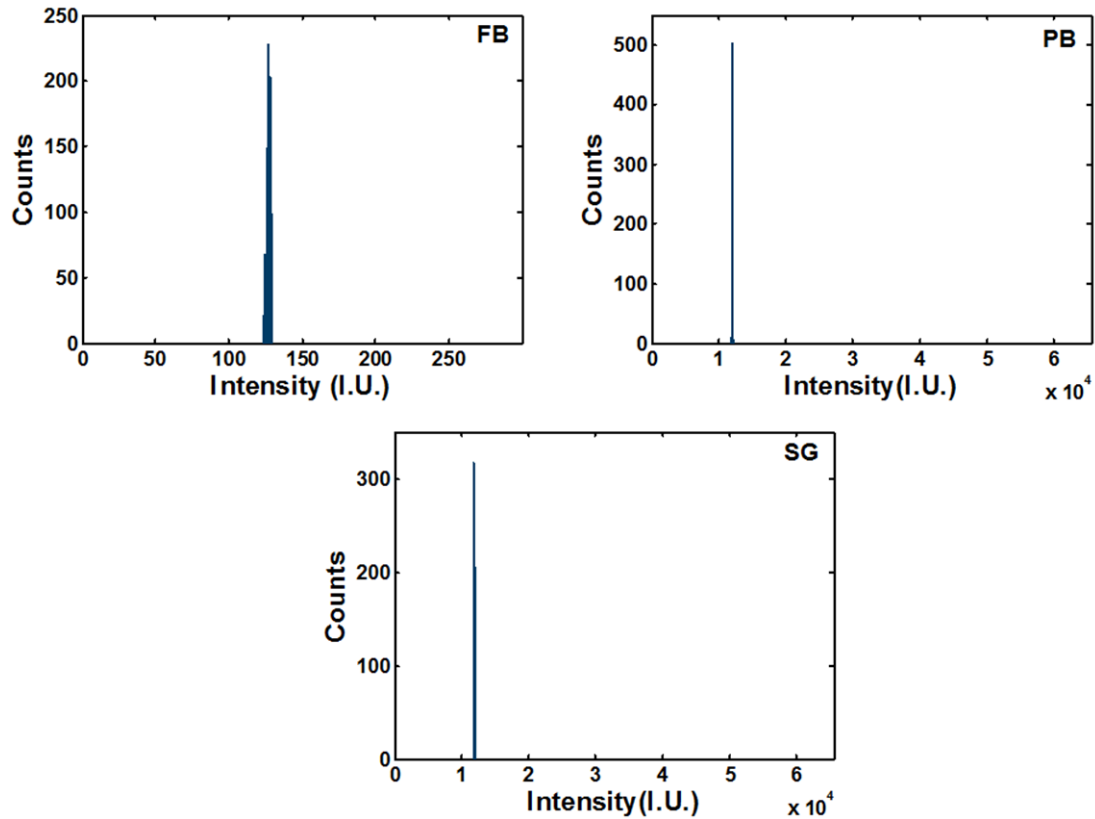
Figure 5.2. Histogram of threshold values of all the 2D slices for the three samples.

We utilize this concept to test the effect of change in threshold on different transport properties as well as their inter-relationship. This can be done by applying a constant threshold value to all the slices and obtaining a 3D binary image. From this binary 3D image, we randomly select ten REV sized samples (Chapter 4, section 4.3) and calculate their porosity, permeability, and formation factor as described in Chapter 4, section 4.4. We then change the threshold value to obtain a different 3D binary image and repeat all the other steps to obtain a new set of porosity, permeability, and formation factor. Throughout the exercise, the ten subsamples selected in the beginning are not changed. We call this method threshold sweeping.

We apply threshold sweeping to all the three samples (FB, PB, and SG). The

threshold values for which we obtain the 3D binary images are summarized in Table 5.1.

Table 5.1. List of threshold values for all the sample used in threshold sweeping to obtain different binary cubes. The mean Otsu's threshold for all the samples is also given for reference.

Samples	Mean Otsu's Threshold (I.U.)	Threshold values (I.U.)
FB	127	120, 130, 140, 150, 160, 170
PB	12078	10000, 10500, 11000, 11500, 12000, 12500
SG	11923	10000, 10500, 11000, 11500, 12000

5.4 RESULTS

For all the three samples, the variation of three computed transport properties with the threshold value is shown in Figure 5.3. Porosity and permeability increase with increasing threshold, whereas the formation factor decreases with increasing threshold. This is because as we increase the threshold, more pixels are classified as pores (low intensity pixels) than grains (high intensity pixels).
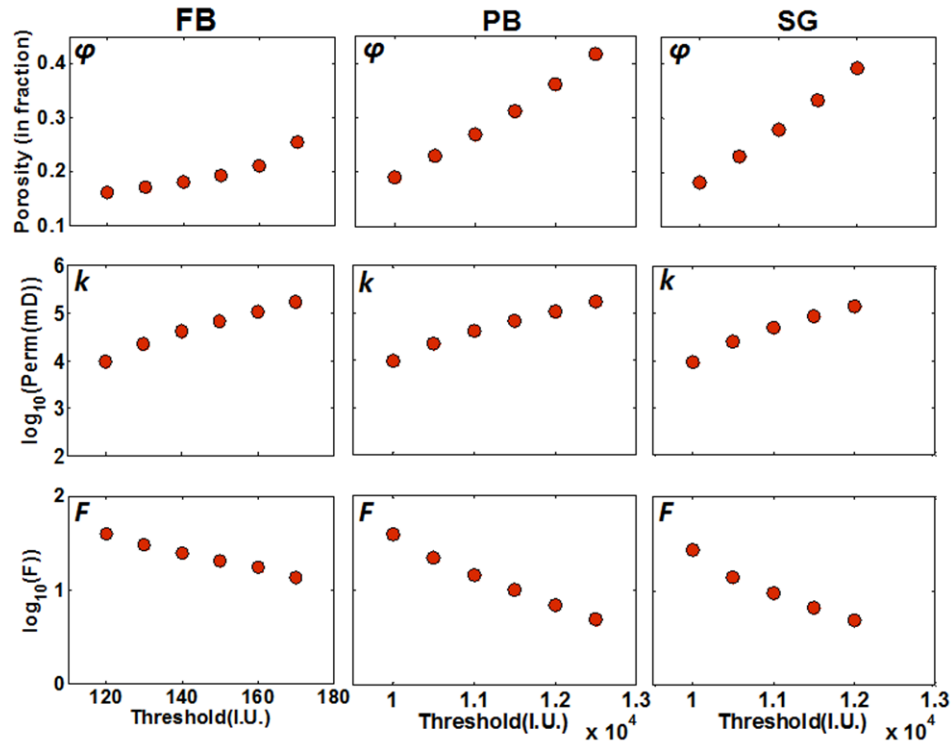
Figure 5.3. The change in transport properties observed with change in threshold. Top to bottom: porosity, permeability, and formation factor versus threshold. Left to right: FB, PB, and SG.

For all three samples, Figure 5.4 shows cross-plots of porosity and permeability, while Figure 5.5 shows cross-plots of porosity and formation factor of the computed data obtained by threshold sweeping. In addition, we also plot the laboratory measured porosity-permeability and porosity-formation factor trends for the Fontainebleau sample. As discussed in Chapter 4, we cannot produce a laboratory measured trend for these artificial samples since we have only one measurement for the Pomponio beach and San Gregorio samples. Therefore, for these samples we plot the theoretical relations of Kozeny-Carman (Carman, 1937) and Archie (1942), respectively, as described by Equations 4.6 and 4.7, respectively, in Chapter 4. We plot the Kozeny-Carman for three different grain sizes: mean grain size, minimum

grain size, and maximum grain size observed in the sample (Kameda, 2005) while we plot Archie's equation for three different values of cementation constant, m = 1.6, 1.8, and 2.0.
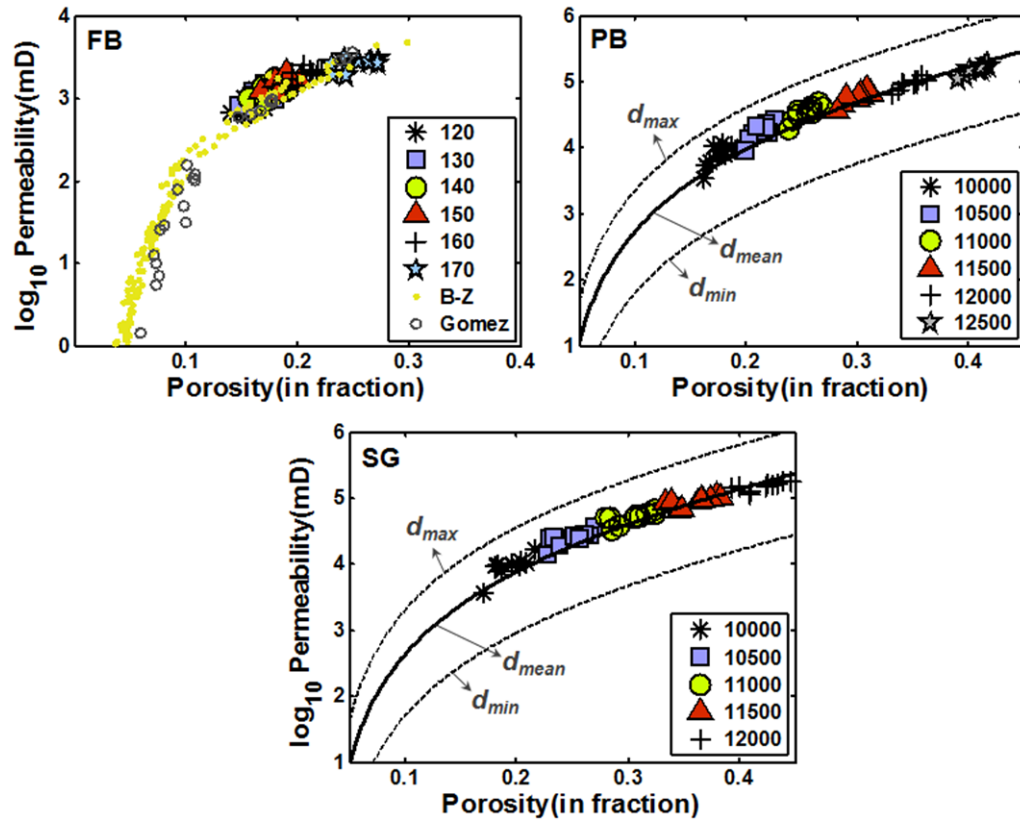
Figure 5.4. Porosity-permeability cross-plots for the FB, PB and SG sands obtained using threshold sweeping are plotted. For the FB, we also plot the laboratory data (Bourbie and Zinszner, 1985; Gomez, 2009) while for the PB and SG we plot Kozeny-Carman relations for different grain sizes: mean grain size, d_{mean}; minimum grain size, d_{min}; and maximum grain size, d_{max} (Kameda, 2005). The numbers in the legend show the threshold used for each group of digital samples.
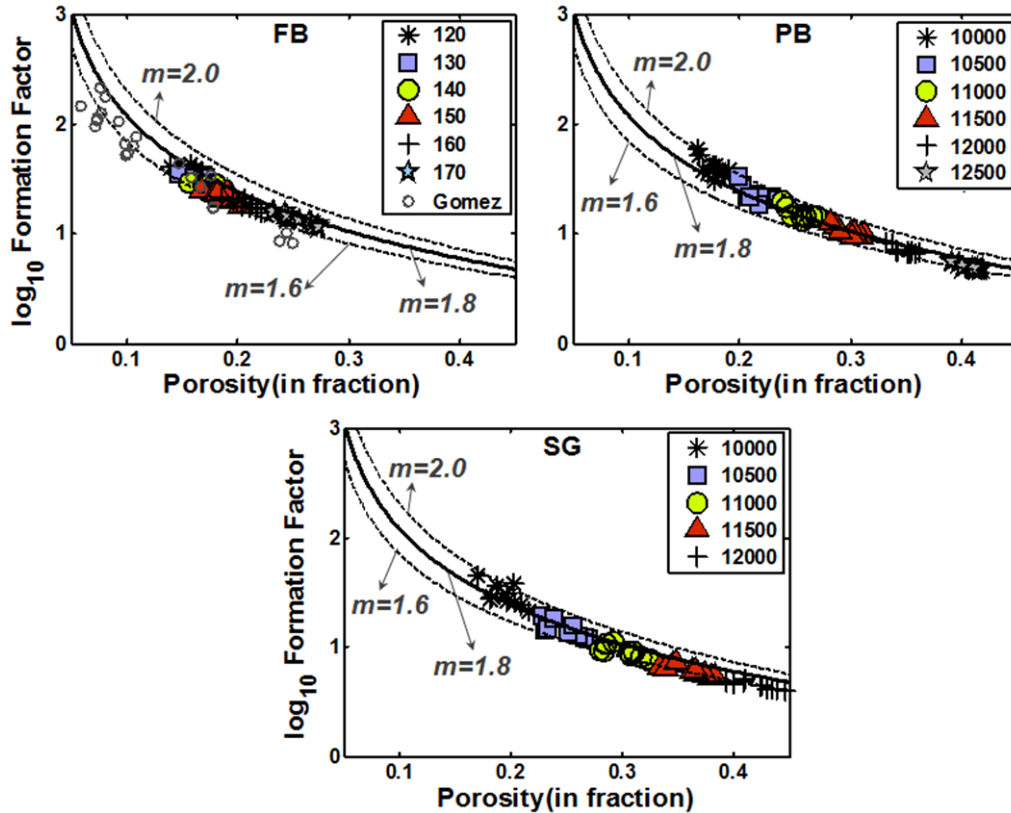
Figure 5.5. Porosity-formation factor cross-plots for the FB, PB, and SG samples. For the FB samples we also plot the laboratory data from Gomez (2009). The curves in each plot are Archie's relation for cementation factors, m = 1.6, 1.8, and 2.0 as indicated in the plots. The numbers in the legend show the threshold used for each group of digital samples.

For the FB sample, we observe a good qualitative fit between the computed data and laboratory data for both porosity-permeability and porosity-formation factor trends (Figure 5.4 and 5.5). For the PB and SG samples, Figure 5.4 shows a robust qualitative fit between the Kozeny-Carman curves calculated for these samples using the mean grain size, while Figure 5.5 shows a qualitative fit between calculated data and the Archie's equation. The computed data points for the PB and SG move along the theoretical curves, very much similar to what we observe in a collection of

different laboratory measured physical samples of the same rock type. However, the trends obtained here are from just one physical sample per sand. This means that by varying threshold, we can produce physically meaningful and justifiable porosity-permeability and porosity-formation factor trends.

We next plot porosity-permeability computed data trend for the three samples together along with laboratory measured data for the Fontainebleau sandstone from Bourbie and Zinszner (1985) and Gomez (2009) (Figure 5.6, left). Computational permeability-porosity trends for the PB and SG in Figure 5.6 are congruent with the experimental and computational FB trend. However, the latter is shifted vertically down from the former two trends due to the difference in the mean grain size which is about 250 microns in the FB sample (Bourbie and Zinszner, 1985) and, 392 and 437 microns in the SG and PB samples, respectively (Kameda, 2005). The grain size of the sample is directly proportional to the permeability of the sample (Kozeny-Carman, Equation 4.6).

The difference in the mean grain sizes between the PB and SG samples is not as large as difference between the FB and SG samples. Hence, while we observe a clear jump in the trends from the FB samples to the SG samples, the difference in the PB and SG trends is not as considerable.

Figure 5.6 also shows the porosity-permeability trend when the permeability (both computed and laboratory measured permeability) of all the samples are normalized by square of mean sample grain-size (Figure 5.6, right). We observe that the vertical shift between the trends is not as significant in the second plot. However since the slopes of the porosity-permeability trends for different samples (FB, PB, and SG) are

100

different, therefore we still observe some shift in the trends.
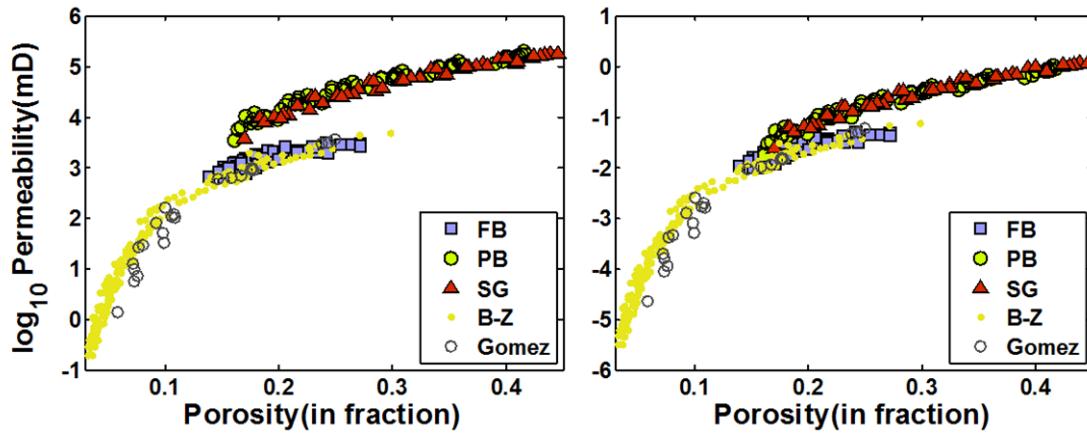
Figure 5.6. Left: Porosity-permeability cross-plot for computational data produced by threshold sweeping for the FB, PB, and SG, along with the laboratory Fontainebleau data from Bourbie and Zinszner, (1985) and Gomez (2009). Right: Porosity-normalized permeability cross-plot for computational data produced by threshold sweeping for the FB, PB, and SG along with the laboratory Fontainebleau data from Bourbie and Zinszner, (1985) and Gomez (2009). The computed permeability as well as laboratory measured permeability of each sample is normalized by square of mean grain size of that sample.

Similarly, we plot porosity-formation factor computed data trend for the three samples along with the Fontainebleau laboratory data (Gomez, 2009) and Archie's equation (Figure 5.7). The grain size of the sample does not affect the formation factor of the sample. Hence, all the three computed data trends lie close together.
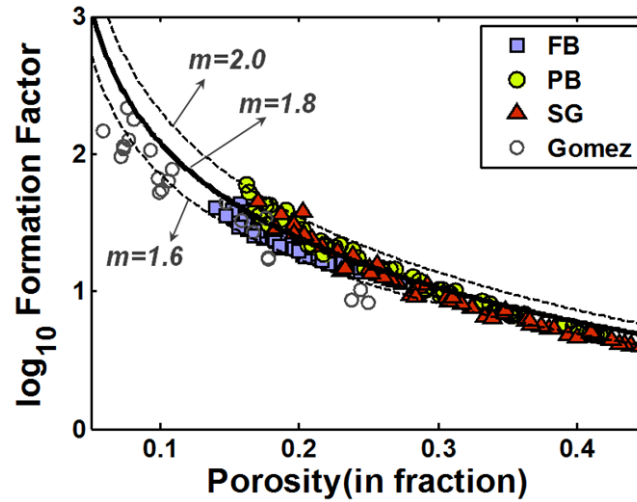
Figure 5.7. Porosity versus formation factor for computational data produced by threshold sweeping for the FB, PB, and SG, along with the laboratory Fontainebleau data from Gomez (2009). The curves are Archie's relation for three different cementation factor, m =1.6, 1.8, and 2.0 as indicated in the plot.

5.5 DISCUSSION

To understand the physics behind the property variations versus the change in threshold, we choose a small portion of randomly selected slices from all the samples and obtain three binary images by applying three different threshold values (Figure 5.8). We observe that the grains systematically grow into the pore space as the threshold increases, very much like diagenetic cement accumulating on the grains in real rock (Figure 5.9, from Avseth, 2000). As a result, both porosity and permeability decrease in a very systematic way observed, e.g., in the Fontainebleau sandstone (Bourbie and Zinszner, 1985). In essence, a mathematically imposed increase in threshold invokes a geometry that resembles a quartz overgrowth for these CT-scans. This correspondence becomes especially striking when we compare Figure 5.8 to Figure 5.10 where the growth of diagenetic cement is shown on a real sample of the

Fontainebleau sands (Haddad et al., 2006). The Fontainebleau formation, as discussed in Chapter 3, section 3.3.1, is a pure quartz formation with several laterally extensive quartz-cemented horizons due to quartz overgrowth (Cooper, 1994; Thiry et al., 1988).
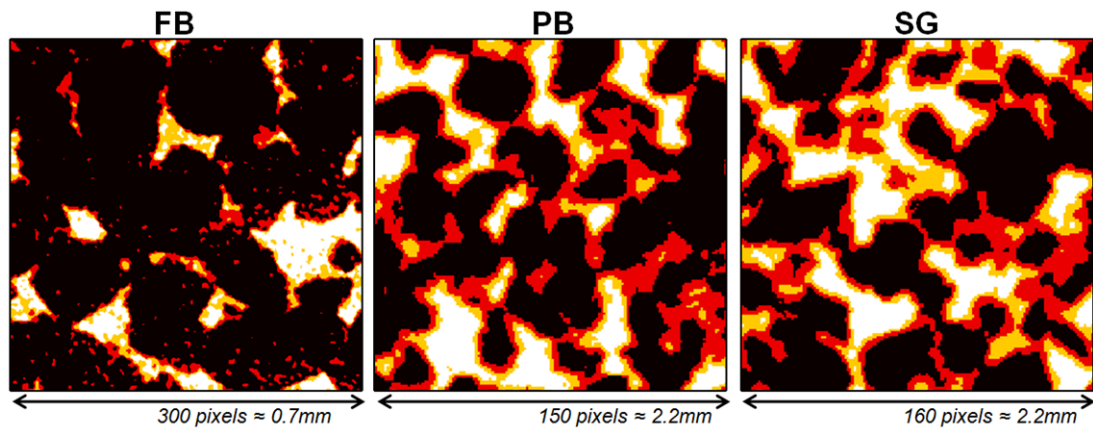
Figure 5.8. Image of randomly selected slices for three increasing threshold values for the three samples. The smallest threshold produces grains as black while the rest are pores (red, orange, and white). For the next threshold value, the grains are black and red while the pores are orange and white. Lastly, for maximum threshold used, the grains are black, red, and orange while the pores are white. The pore space systematically shrinks as the grains grow to include red and then orange areas.
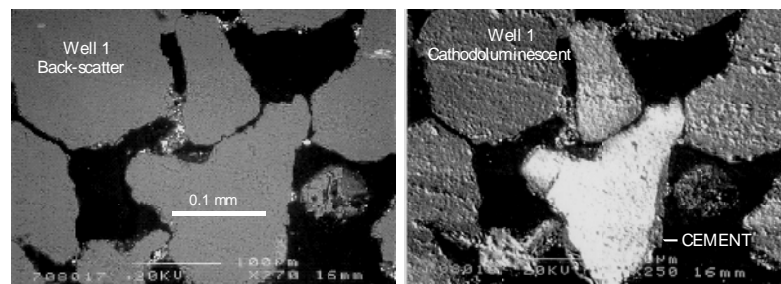
Figure 5.9. A thin section of a North Sea sandstone showing a diagenetic cement rim (dark gray) around a quartz grain (bright white). (From Avseth, 2000).
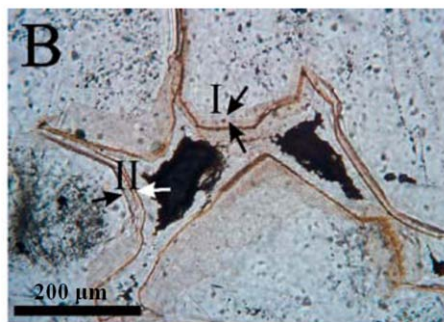
Figure 5.10. A Fontainebleau sandstone image in plane polarized light showing cement growth into the pore space from the originally deposited grains. Arrows I and II highlight thin, isopachous bands around the detrital grain and the overgrowth (From Haddad et al., 2006).

A similar effect was observed by Keehm (2003) when they computed the permeability of a random dense pack of identical spheres (the Finney pack) while systematically and uniformly increasing the radii of the grains to imitate progressive cementation. They also numerically simulated various diagenetic processes, in which the pore-filling mechanism (diagenesis) was controlled by flow rates. They classified the pore-filling mechanisms into four basic groups (Figure 5.11); the grain-pore-boundary–related mechanism (Group I), the low-flux–related mechanism (Group II), the high-flux mechanism (Group III), and random filling (Group IV). In their analysis using the synthetic pore geometry (a random dense pack of spheres) and the Fontainebleau sandstone, they found that the Group I diagenesis mechanism closely follows the Kozeny-Carman relation (Figure 5.12). Similarly for the porosity-formation factor trends, Archie's law is closest to the Group I diagenesis mechanism (Figure 5.13).

These observations support the idea that the grain-pore boundary diagenesis method, e.g. quartz overgrowth, is closely related to the theoretical relations as

Kozeny-Carman and Archie's relation, in corroboration with our earlier observations in this section.
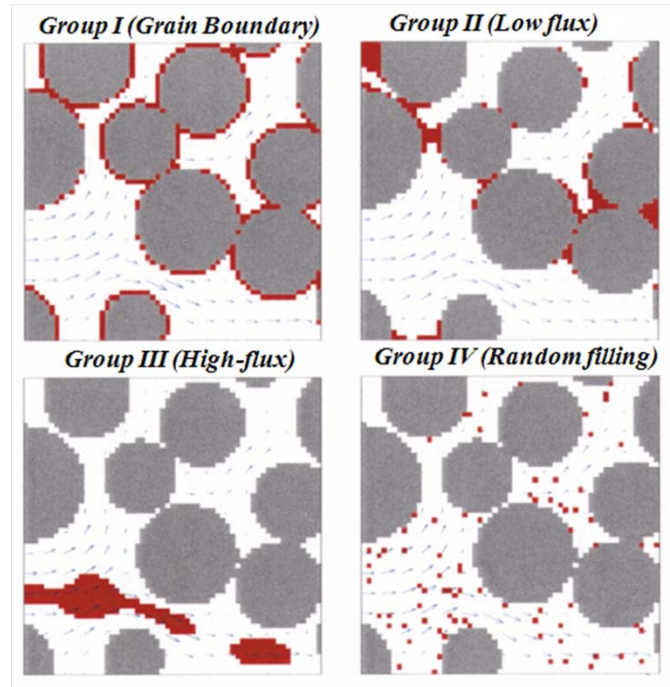
Figure 5.11. Cross-sectional view of fluid flux distribution (arrows) and filled pore nodes (red area) according to the different pore-filling mechanisms. The length of arrow denotes the magnitude of the flux. Gray areas are initial grains. (From: Keehm, 2003)
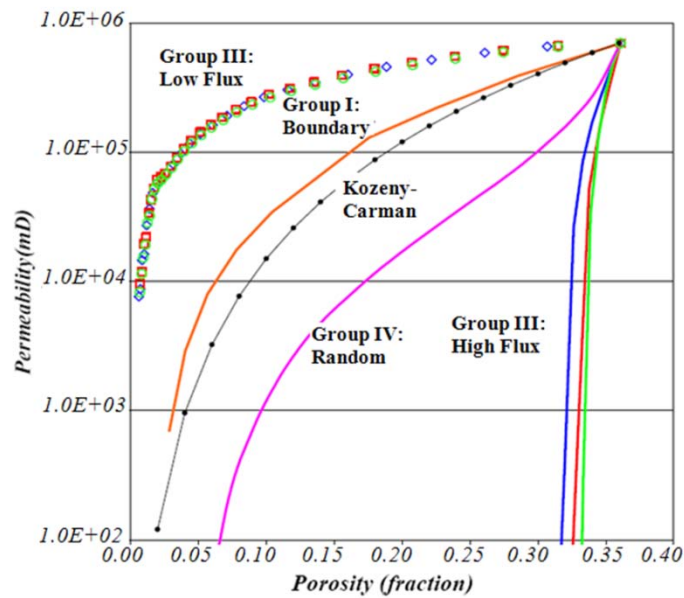
Figure 5.12. Porosity-permeability trends for different pore filling mechanisms. (From: Keehm., 2003).
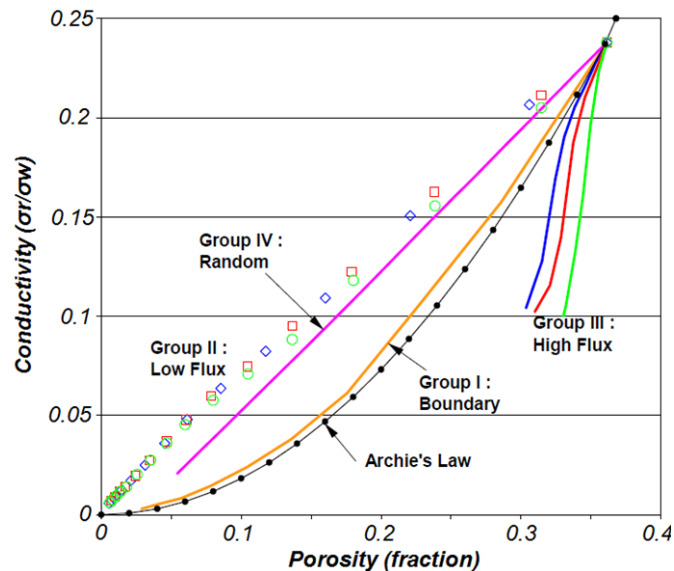
Figure 5.13. Porosity-conductivity trends for different pore filling mechanisms. (From: Keehm, 2003).

The effect of a progressively increasing threshold and the invoked binary geometry depends on the relative spatial distributions of low, intermediate, and high

pixel intensity values. The resemblance to a diagenetic pore filling mechanism occurs when there is a smooth gradation from low, through intermediate to high values. A different spatial scenario is one where the low intensity values are separated from the intermediate values by spatially intervening high intensity values. This for example might be the case of rims of high density (and high intensity) cement surrounding grains of intermediate intensity, with the pores being the lowest intensity. However, since any imaging (including CT scans) imposes a smoothing operation, the images will be the result of a convolution with the instruments point spread function. This smoothing effect will tend to create gradations from low, to high, through intermediate intensity values. This effect is shown in Figure 5.14. In Figure 5.14, top left shows a synthetically created random spatial field with low and intermediate intensities disconnected by high intensities, created using a standard geostatistical truncated Gaussian simulation. Bottom left shows the corresponding geometry invoked by an increasing threshold. Notice that unlike Figure 5.8, the red does not surround the black. However as soon as a small 3x3 smoothing filter is applied to the original gray scale image to obtain a smoothed image (top right), the increasing thresholded geometry shows resemblance to diagenetic cement growth with red surrounding black, followed by orange and white (bottom, right).
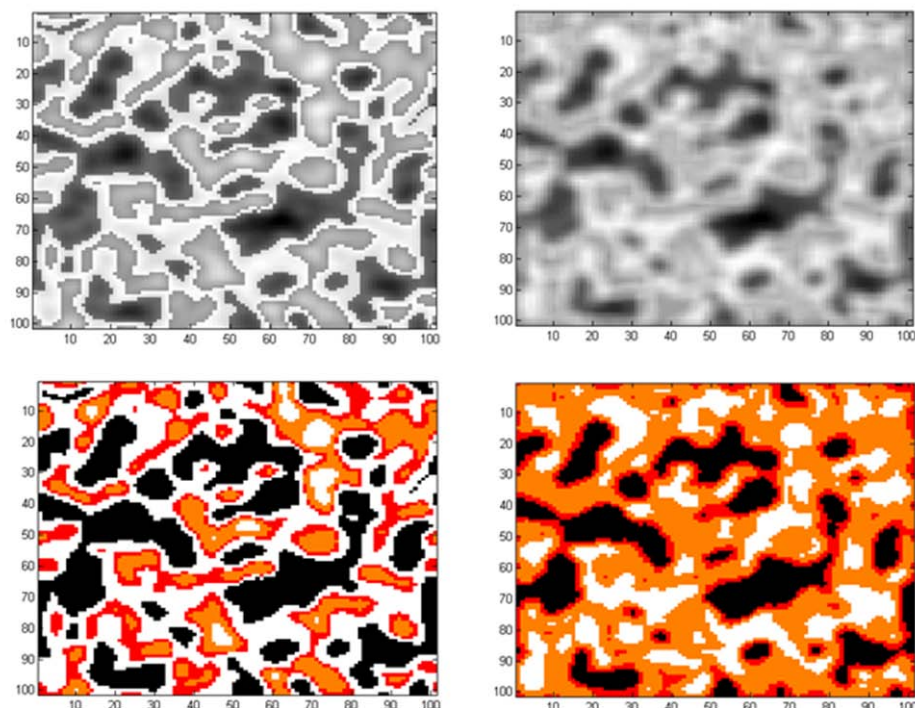
Figure 5.14. Effect of spatial distribution of grayscale and smoothing on the geometry invoked by increasing threshold. Top left: a synthetically created spatial field with low and intermediate intensities disconnected by high intensities. Bottom left shows the corresponding geometry invoked by an increasing threshold. Top right: smoothed grayscale image corresponding increasing thresholded geometry shows resemblance to diagenetic cement growth with red surrounding black,. Bottom right shows the corresponding geometry invoked by an increasing threshold.

5.6 CONCLUSION

We discovered that a trend between porosity and permeability, and between porosity and formation factor can be obtained from a single digital sample by simply classifying it by spanning a range of threshold values, a process that we refer to threshold sweeping, at least, for samples used in this study. This variation in threshold will change porosity as well as permeability and electrical conductivity. However, the data points thus produced fall into very systematic and relatively tight

porosity-permeability and porosity-formation factor trends.   These trends are consistent with laboratory measurements on samples whose pore space geometry is altered by quartz overgrowth.   This phenomenon is valid for the samples examined here and is likely to hold for clastic rock with quartz cementation.   The practical implication of this finding is important: just a few digital samples can be used to create a massive geologically plausible database.

Chapter 6

Resolution and Transport Properties Trends

6.1 ABSTRACT

Resolution of an image influences the details depicted by the image and hence may affect the porosity and pore connectivity of a 3D image. We analyze the change in transport properties -- porosity, permeability, and formation factor – and their interrelationships or trends, specifically porosity-permeability and porosity-formation factor, as the resolution is coarsened up to ten times of the finest resolution by linear interpolation.

As the resolution is coarsened, we observe a little change in porosity and formation factor while permeability increases. The coarsening of the resolution results in reduction in specific surface area (surface area divided by the volume) as the pores assume blocky shape and since permeability is the only property that depends on specific surface area, we observe a change in permeability only.

However, when the porosity-permeability trend for different resolutions are compared against laboratory and theoretical relationships, the increase in permeability lies with in the scatter of the data and hence, is acceptable.

This result implies that we can acquire the images at lower resolution and still obtain meaningful results.

6.2 INTRODUCTION

The resolution of an image is defined as the size of a single voxel in length units. The size of voxel in an image affects the details that can be depicted in the image, and hence it may also affect the porosity and pore-connectivity in 3D. In this chapter, we explore the change in porosity (φ), permeability (k), and the formation factor (F) as the resolution of the image is changed. We first image a porous rock fragment at the finest resolution available, and then coarsen this grid, and compute the transport properties of the digital object as a function of resolution for the three samples Fontainebleau (FB), Pomponio Beach (PB), and San Gregorio (SG), described in Chapter 3, section 3.3.

Specifically, the CT-scan images used to obtain the 3D binary rock images in previous chapters are scanned at a fixed resolution. We do not change that resolution by re-scanning the object as that is beyond the scope of this paper. Instead, we mathematically interpolate ten randomly selected REV-sized finest scale subsamples onto the coarser grid to imitate the effect of coarser resolution. Following this procedure, we re-compute the porosity, permeability, and formation factor for these coarse-grid 3D binary images using the computational rock physics methods

described in section 4.4 of Chapter 4. Throughout the exercise, the ten subsamples selected in the beginning are not changed.

As we coarsen the resolution of 3D image, the porosity of the 3D binary images remains essentially unchanged while the permeability increases slightly. This increase in permeability is due to decrease in specific surface area (surface area divided by the volume) as the resolution coarsens. However, when we compare the porosity-permeability trends for different resolution to the laboratory and theoretical relation, this increase in permeability with resolution lies within the scatter of the data. The change in resolution affects the formation factor very little. This might be due to change in cementation factor in Archie's relation with resolution. However, the change in formation factor is very small to deduct any relation definitely.

These results imply that we can obtain the CT-scan images at a coarser grid without affecting the rock physics trends. However, this study is not exhaustive, and hence we recommend testing the effect of change in resolution on rock physics properties and finding the best possible resolution.

6.3 METHODOLOGY

For the three samples, Fontainebleau (FB), Pomponio Beach (PB), and San Gregorio (SG), we randomly select ten REV-sized samples (Chapter 4) from the host sample. We then linearly interpolate these samples to make each voxel n-times the size of the original voxel, where n varies from two to ten. The methodology involves linearly interpolating the finest resolution digital rock samples onto a coarser grid. We employed linear interpolation technique for achieving this. The linear

interpolation technique calculates the intensity value at an unknown point x between the two known points x_0, x_1 that have intensity value y_0, y_1, respectively, by using

$$y = y_0 + (x - x_0)\frac{y_1 - y_0}{x_1 - x_0},$$

(6.1)

However, since we require the intensity value at the coarser grid, the interpolation technique simply picks the values at these coarser grid points from the finer grid, without using any interpolation. For example, if we interpolate the finest resolution sample to a resolution twice the voxel size of the finest, the algorithm will simply pick every other grid value of the finest resolution sample.

The various resolutions for all three samples in terms of their dimensions in voxels and their resolution in mm/voxel are shown in Table 6.1 to Table 6.3, respectively. For all these samples at various resolutions, we then calculate the porosity, permeability, and electrical formation factor as described in Chapter 4, section 4.4.

Note that the autocorrelation range in mm, remains unchanged as we change the resolution; hence the REV size in mm remains consistent as well. However, the number of pixels in REV size cube changes as we coarsen the resolution as less number of pixels is required to represent the same length.

Table 6.1. The resolution and equivalent REV size for the FB sample.

Resolution	Resolution (mm/voxel)	REV Size (voxels)
Original (1x) voxel size	0.00234	300
2x-voxel-size	0.00468	150
3x-voxel size	0.00702	100
4x-voxel size	0.00936	75
5x-voxel size	0.0117	60
6x-voxel size	0.01404	50
7x-voxel size	0.01638	43
8x-voxel size	0.01872	38
9x-voxel size	0.02106	34
10x-voxel size	0.0234	30

Table 6.2. The resolution and equivalent REV size for the PB sample

Resolution	Resolution (mm/voxel)	REV Size (voxels)
Original (1x) voxel size	0.01477	170
2x-voxel-size	0.02954	85
3x-voxel size	0.04431	57
4x-voxel size	0.05908	43
5x-voxel size	0.07385	34
6x-voxel size	0.08862	29
7x-voxel size	0.10339	25
8x-voxel size	0.11816	22
9x-voxel size	0.13293	19
10x-voxel size	0.1477	17

Table 6.3. The resolution and equivalent REV size for the SG sample.

Resolution	Resolution (mm/voxel)	REV Size (voxels)
Original (1x) voxel size	0.01477	150
2x-voxel-size	0.02954	75
3x-voxel size	0.04431	50
4x-voxel size	0.05908	38
5x-voxel size	0.07385	30
6x-voxel size	0.08862	25
7x-voxel size	0.10339	22
8x-voxel size	0.11816	19
9x-voxel size	0.13293	17
10x-voxel size	0.1477	15

6.4 RESULTS

The porosity, permeability, and formation factor for different resolutions are shown in Figures 6.1, 6.2, and 6.3, respectively.

For all three samples, the porosity is approximately the same at all the resolutions. The permeability, on the other hand, increases as resolution is coarsened. The formation factor shows very little change as the resolution is coarsened.
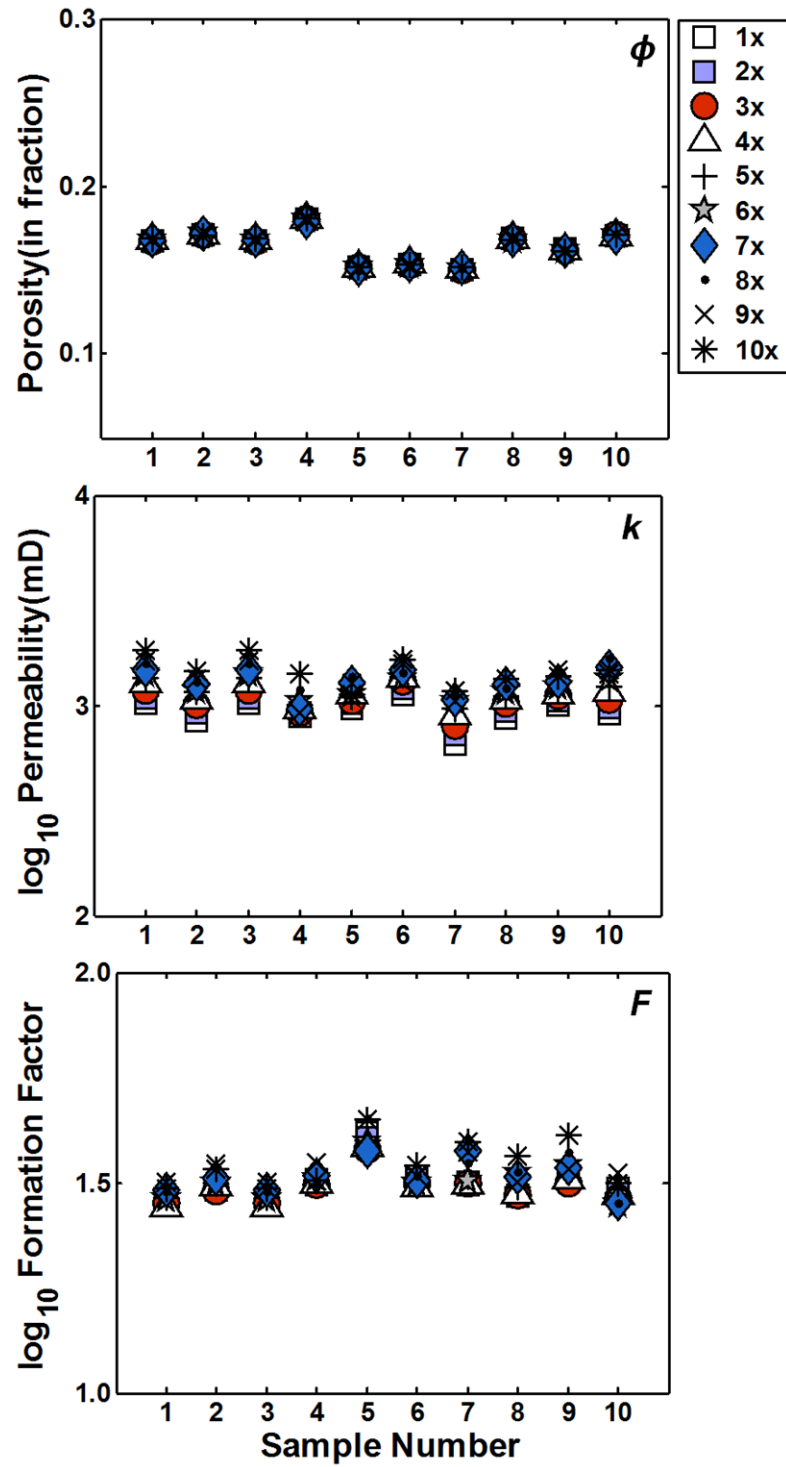
Figure 6.1. The porosity, permeability, and formation factor (top to bottom) at different resolutions for the Fontainebleau samples.
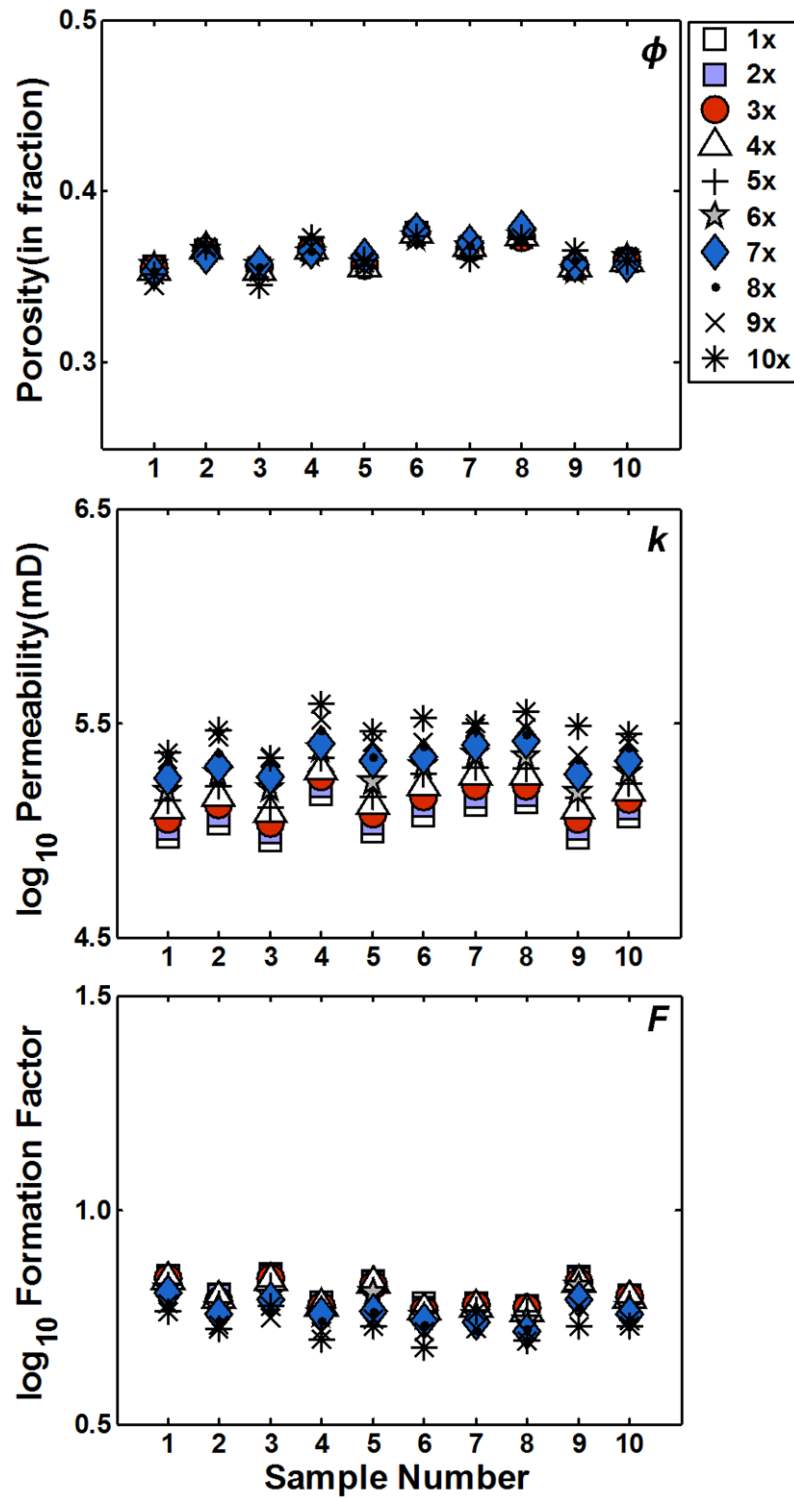
Figure 6.2. The porosity, permeability, and formation factor (top to bottom) at different resolutions for the Pomponio Beach samples.
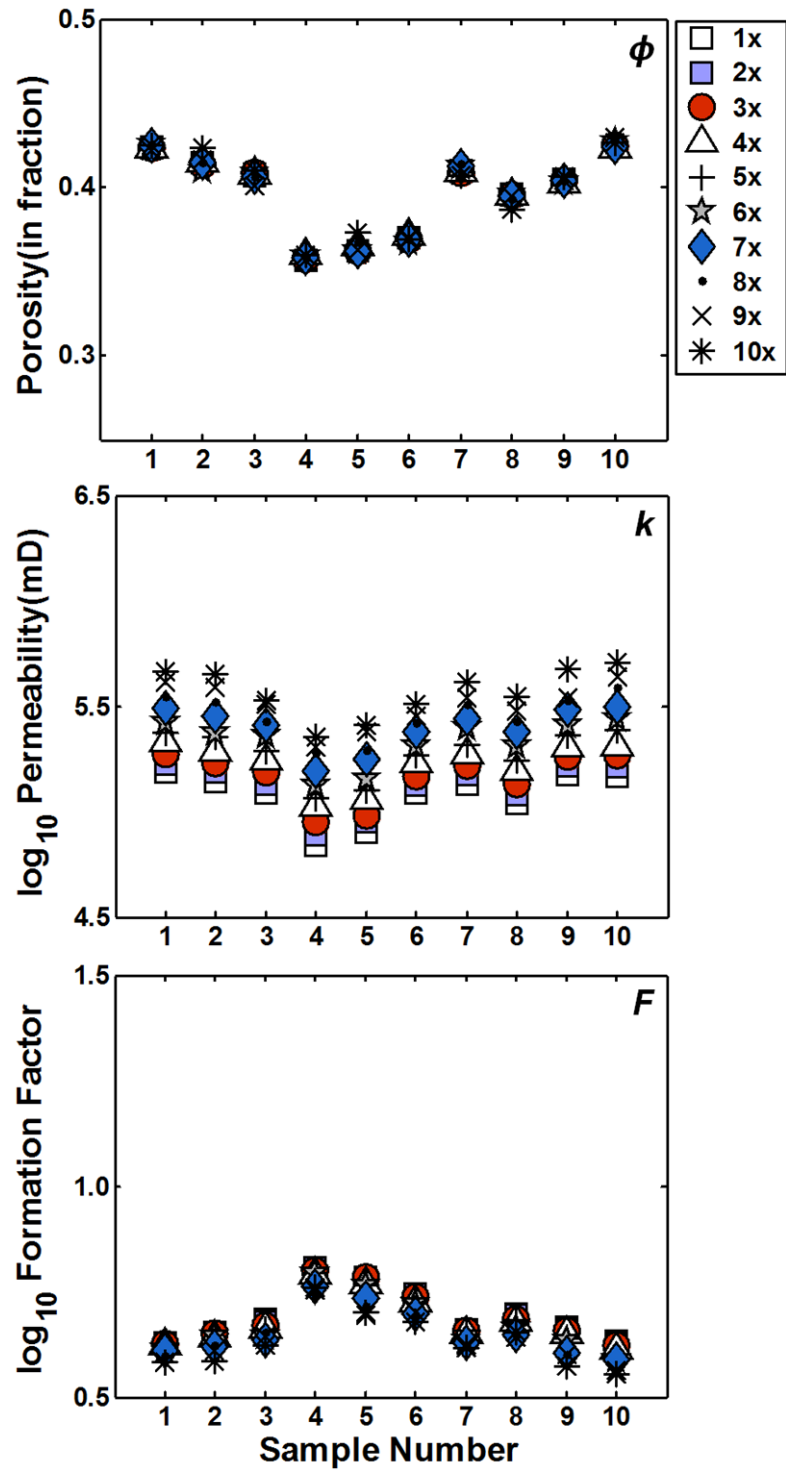
Figure 6.3. The porosity, permeability, and formation factor (top to bottom) at different resolutions for the San Gregorio samples.

For all the samples, we also plot porosity-permeability, and porosity-formation factor trends (Figures 6.4 and 6.5, respectively). We also plot the laboratory measured trend for porosity-permeability and porosity-formation factor trend for the Fontainebleau sample. As discussed in Chapter 4, because we have only one measurement for the Pomponio beach and San Gregorio samples, we cannot produce a laboratory measured trend for these artificial samples. We instead plot the theoretical relations of Kozeny-Carman (Carman, 1956) and Archie (1942), respectively, for these samples. The Kozeny-Carman and Archie's relations are described by Equations 4.6 and 4.7, respectively, in Chapter 4. We plot the Kozeny-Carman for three different grain sizes: mean grain size, minimum grain size, and maximum grain size observed in the sample while we plot Archie's equation for three different values of cementation constant, $m = 1.6$, 1.8, and 2.0.

The porosity-permeability trend shifts vertically as the resolution coarsens. This is consistent with the previous observation that the permeability increases slightly as we coarsen the resolution. However, this shift lies within the scatter of the laboratory data for the Fontainebleau sample and within the two Kozeny-Carman theoretical trends for minimum and maximum grain size distribution for the Pomponio Beach and San Gregorio samples.

The porosity-formation factor trend, on the other hand, shows little change with resolution.
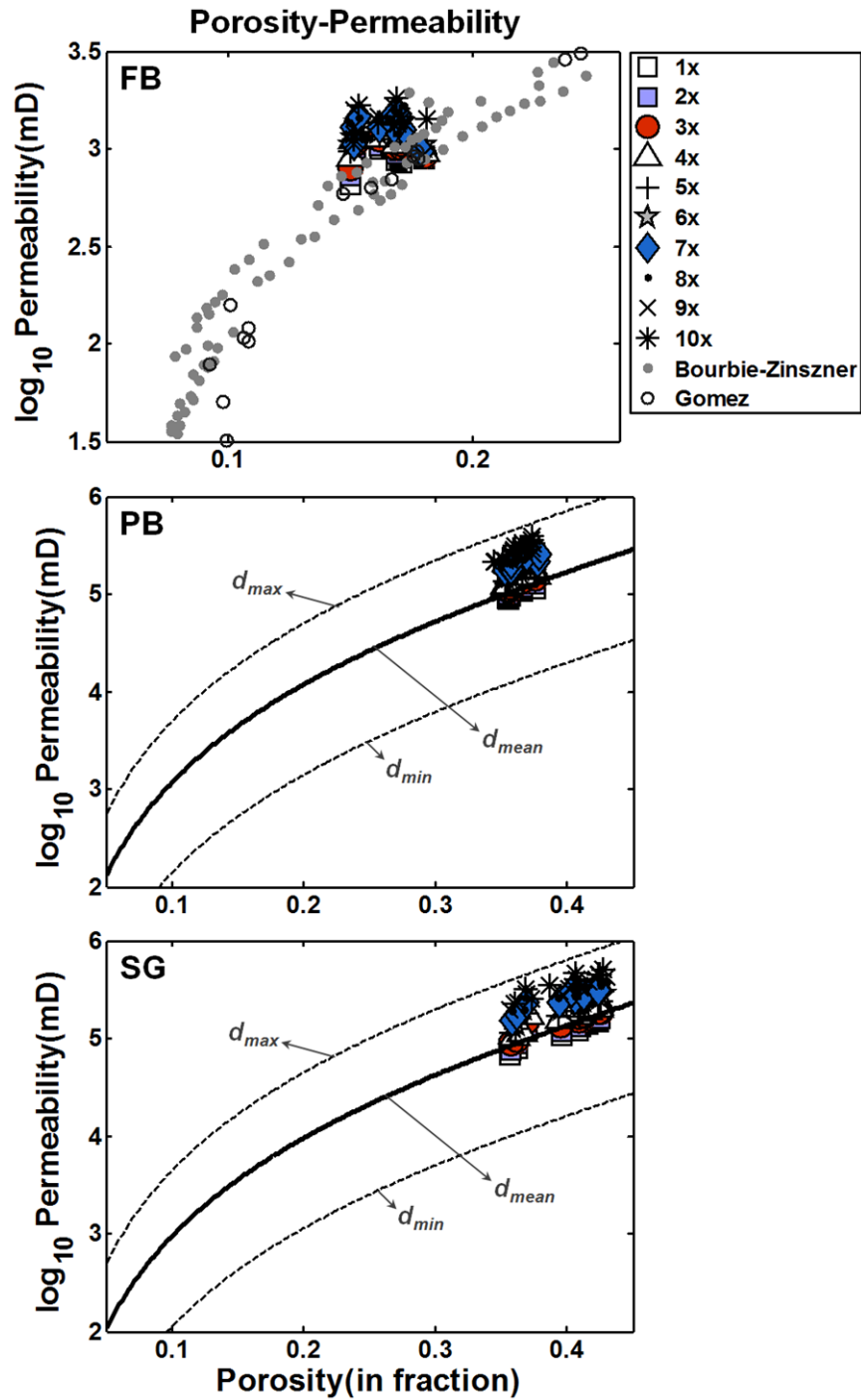
Figure 6.4. Permeability versus porosity for computed data produced by varying the resolution for all three samples. For the FB sample we also plot laboratory data (Bourbie and Zinszner, 1985; and Gomez, 2009) while for the PB and SG, we plot Kozeny-Carman trends for different grain sizes (*dmean*, *dmin*, and *dmax*).
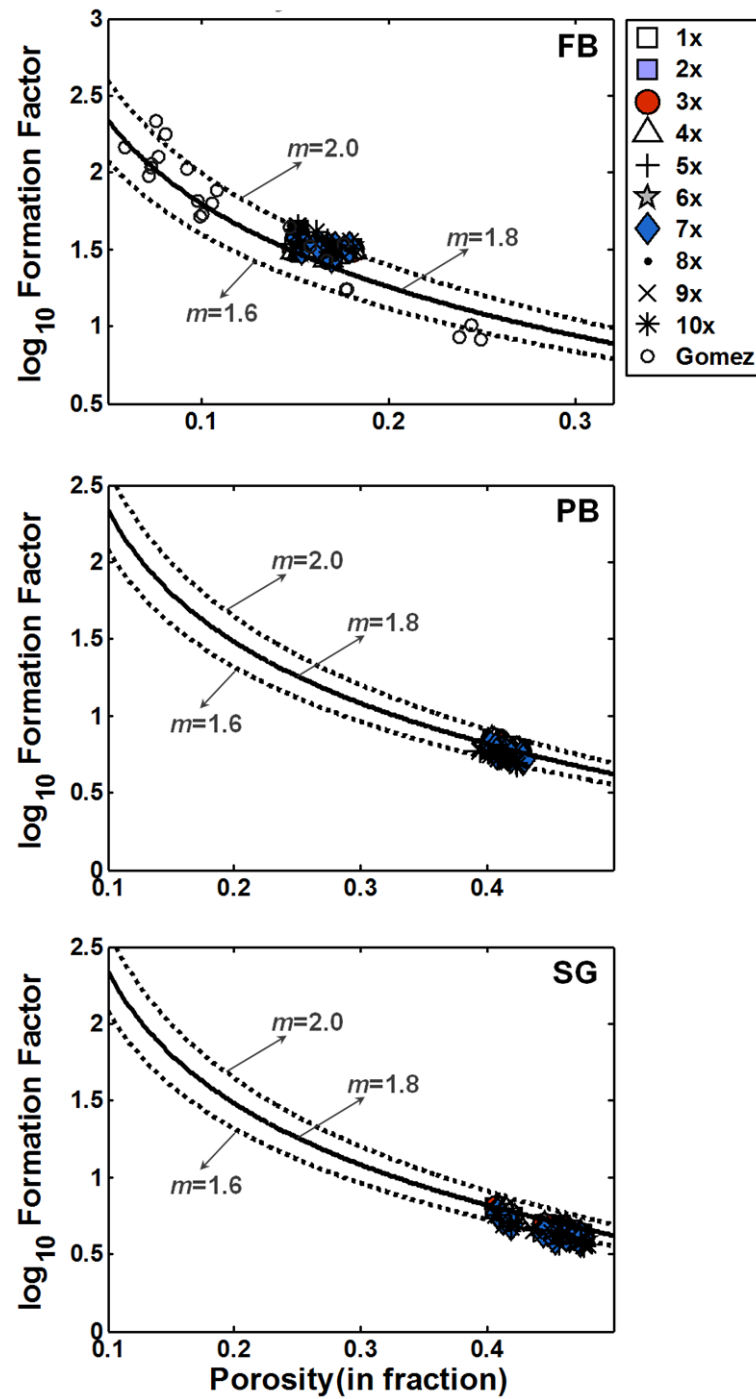
Figure 6.5. Formation factor versus porosity for computed data produced by varying the resolution for all three samples. Archie's relation is also plotted for comparison for different cementation factors, *m* =1.6, 1.8 and 2.0, as indicated.

6.5 DISCUSSION

3D rendering of the original as well as coarsened images of the samples under examination are displayed in Figure 6.6 (Fontainebleau), 6.7 (Pomponio Beach), and 6.8 (San Gregorio Beach). We observe that the pores in the coarsened images attain blocky shapes and, as a result, the pore specific surface area decreases (pore surface area divided by the total volume) as shown in Figure 6.9. This increases the permeability as the permeability is inversely proportional to the square of the specific surface area (Figure 6.10). The porosity, on the other hand, does not directly depend on the specific surface area (Figures 6.11). Hence, it remains practically unchanged. The formation factor change slightly with the resolution (Figure 6.12). This might be due to the change in cementation factor (*m* in Equation 4.7) with change in specific surface area. However, the change in formation factor is very small to determine any relation between the two factors.

2x   **3x**   **4x**

5x   **6x**   **7x**

8x   **9x**   **10x**
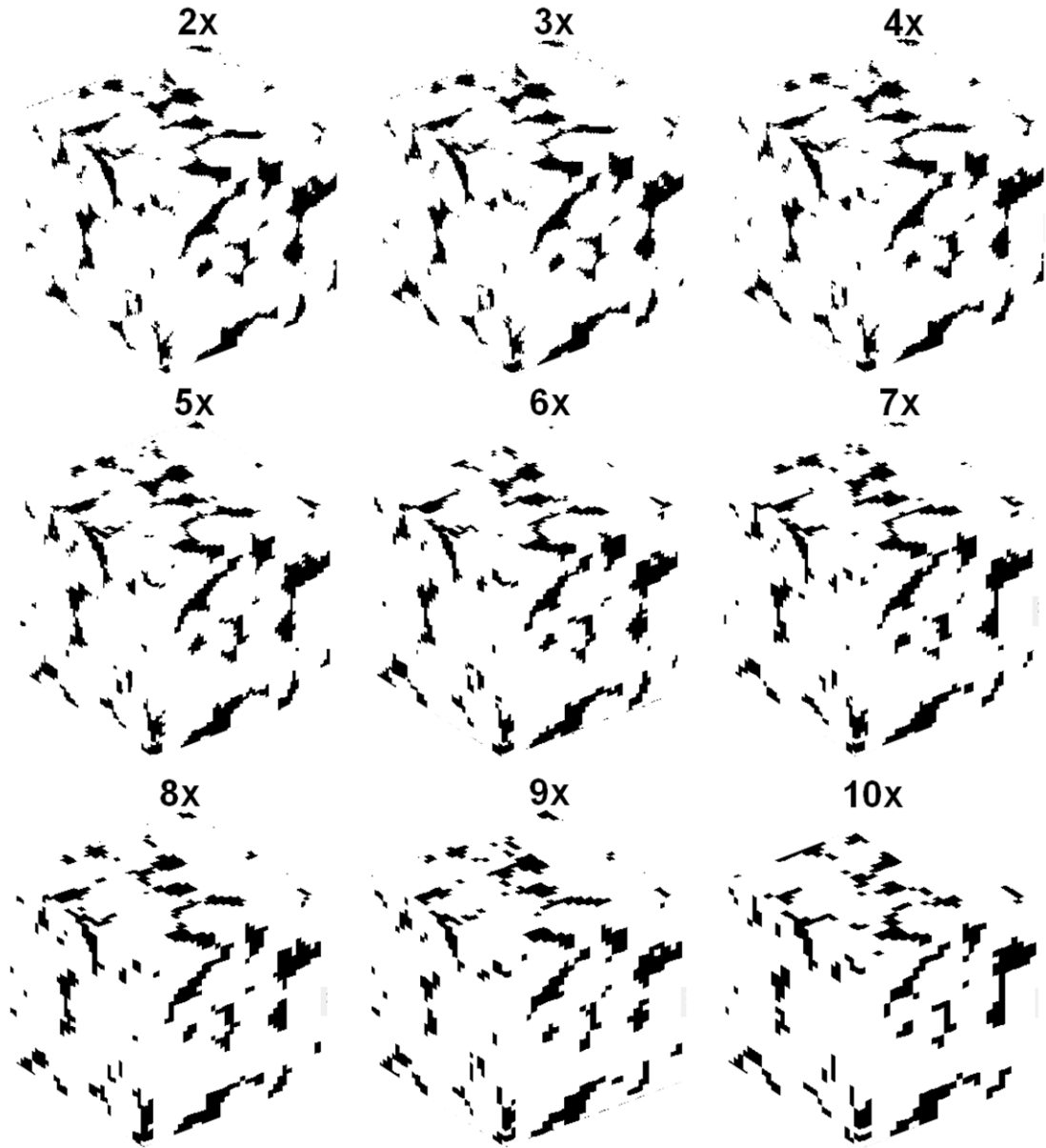
Figure 6.6. 3D rendering of the Fontainebleau sample the coarsened samples. The original image is very close to the 2x rendering shown in the figure.
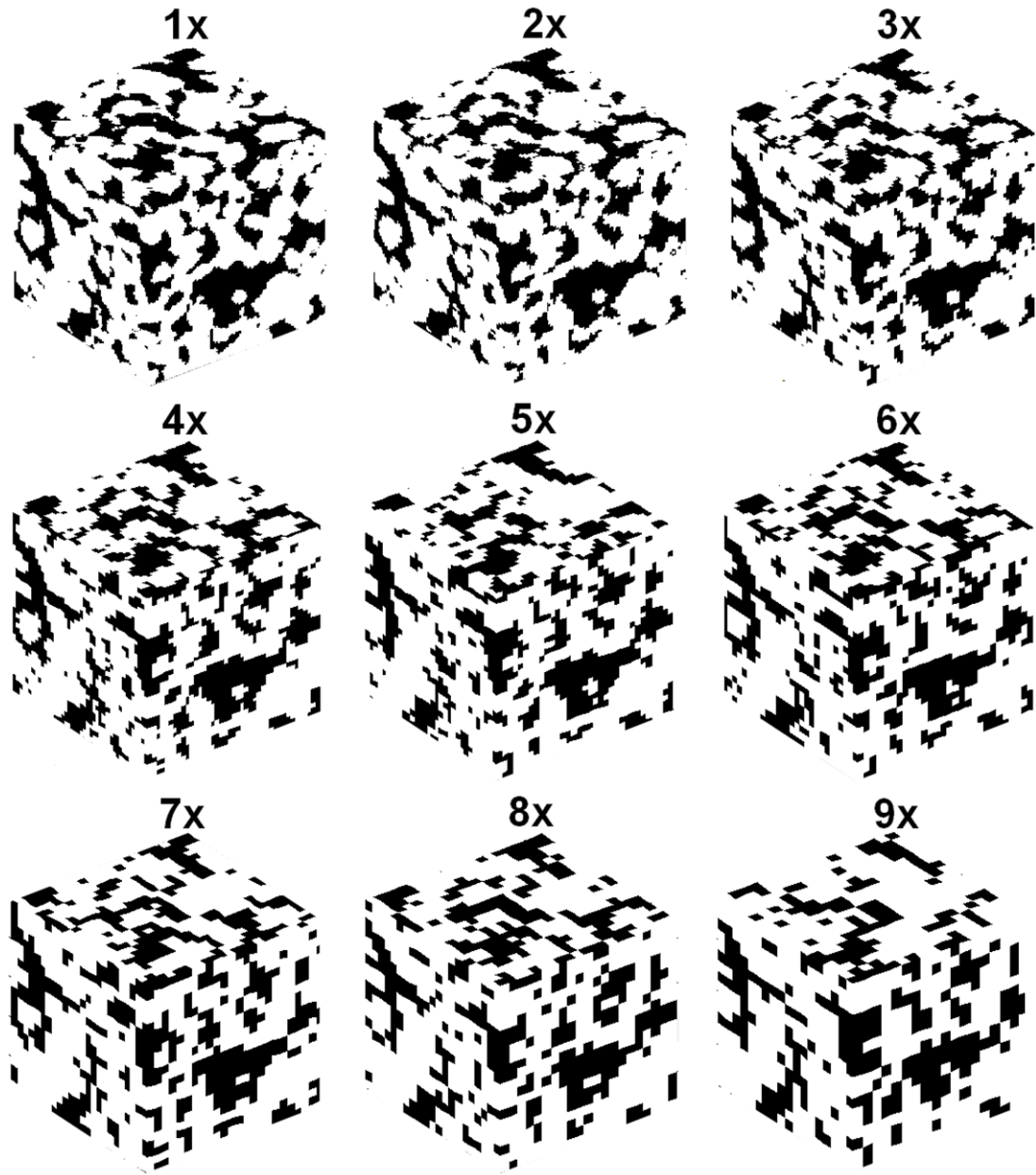
Figure 6.7. 3D rendering of the Pomponio Beach sample for the original as well as the coarsened samples. We do not show the 10x coarsened sample here; however, it is fairly close to the 9x coarsened sample.
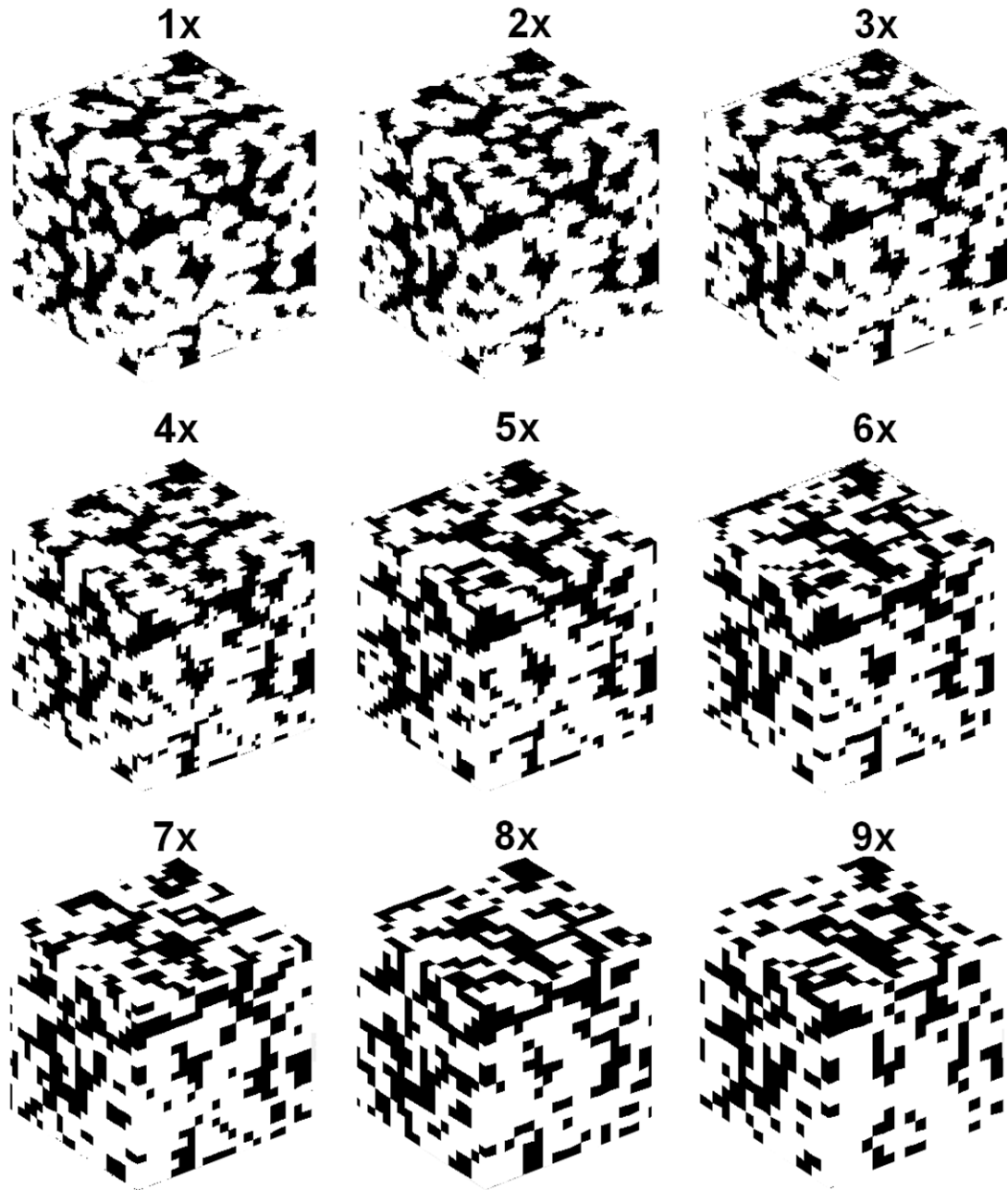
Figure 6.8. 3D rendering of the San Gregorio sample for the original as well as the coarsened samples. . We do not show the 10x coarsened sample here; however, it is fairly close to the 9x coarsened sample.
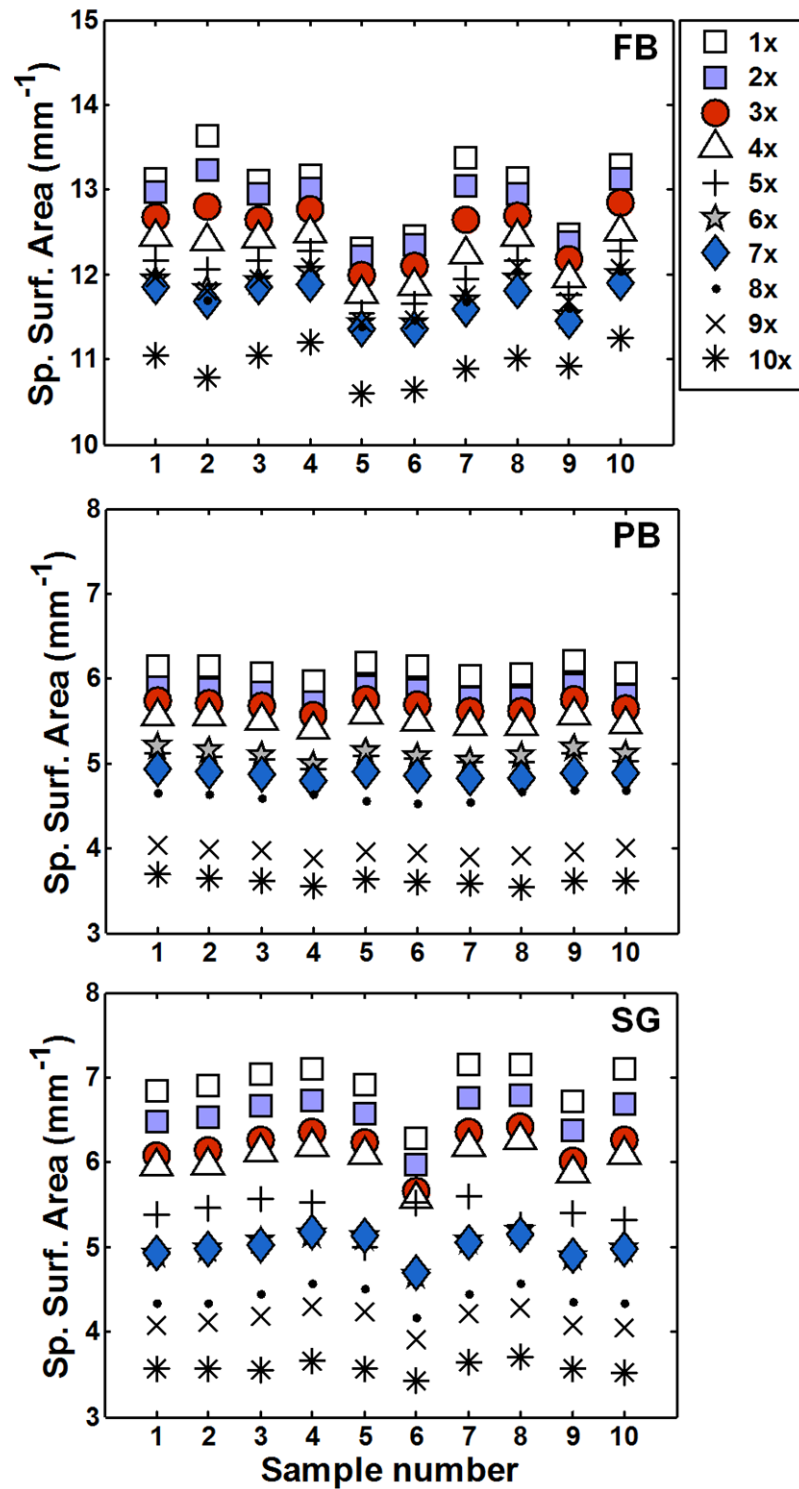
Figure 6.9. The specific surface area (mm^{-1}) of different samples as a function of resolution for all three samples.
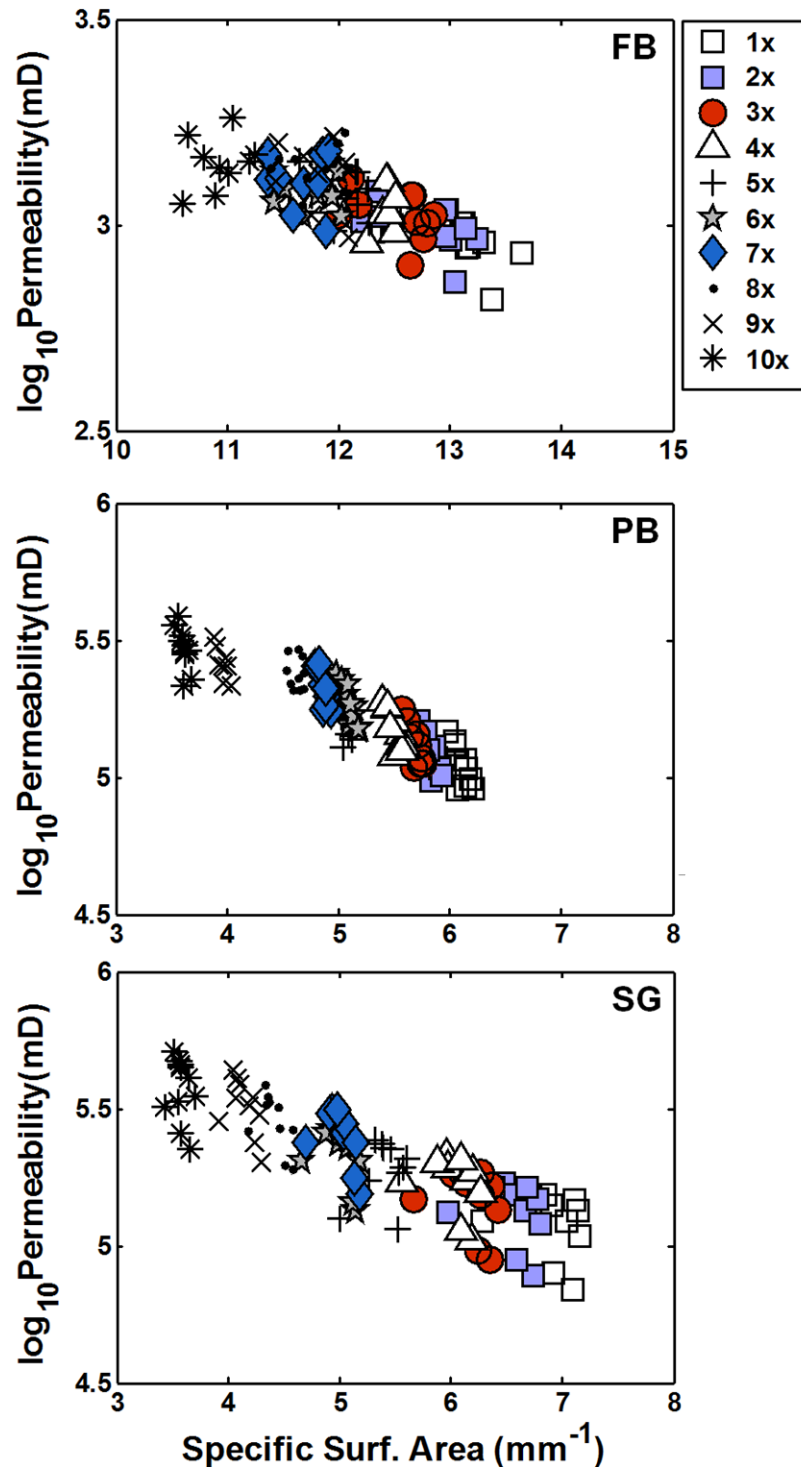
Figure 6.10. The specific surface area versus permeability as a function of resolution for all three samples. There is an inverse relation between permeability and surface area.
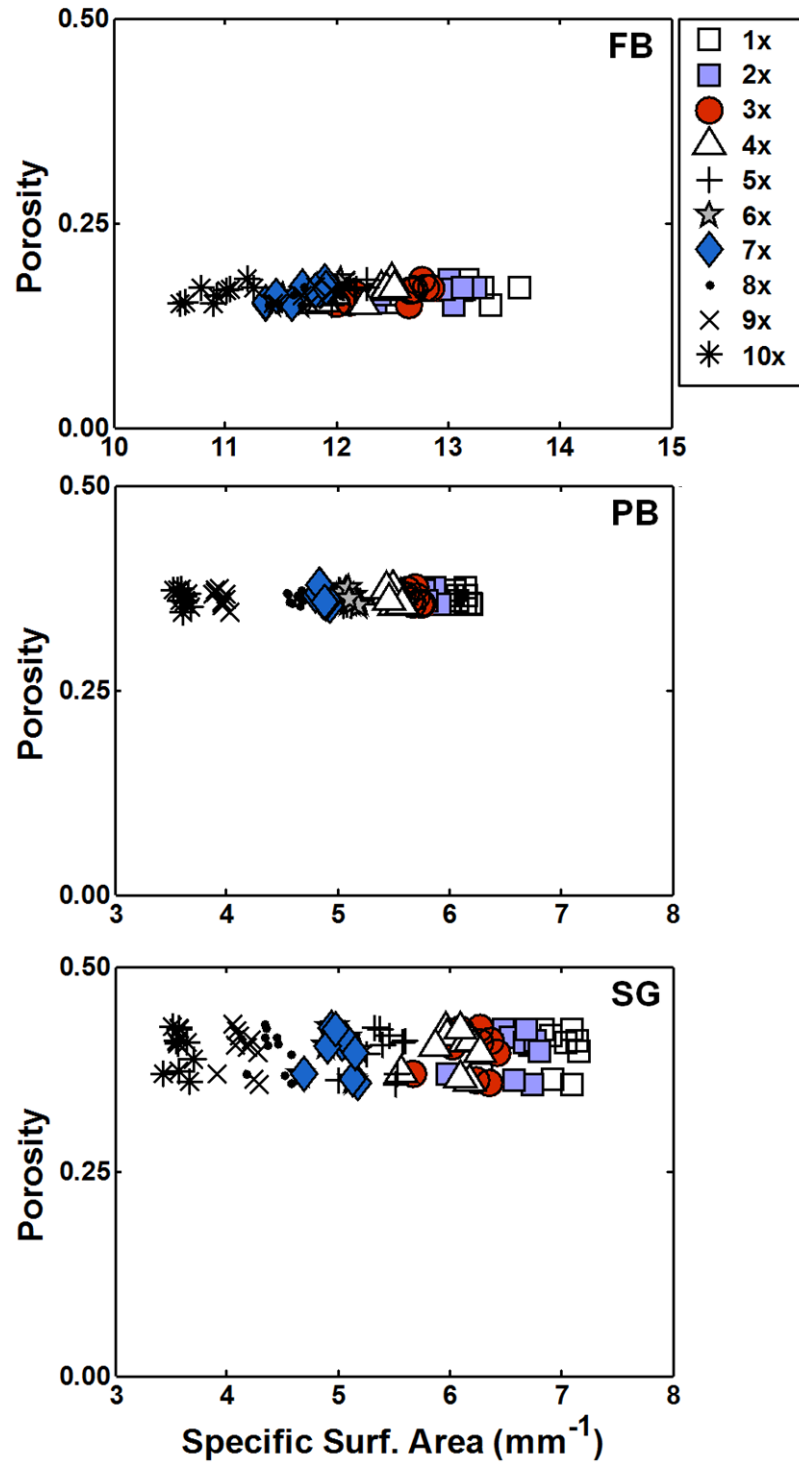
Figure 6.11. The specific surface area versus porosity as a function of resolution for all three

samples. There is no apparent relation between porosity and surface area.
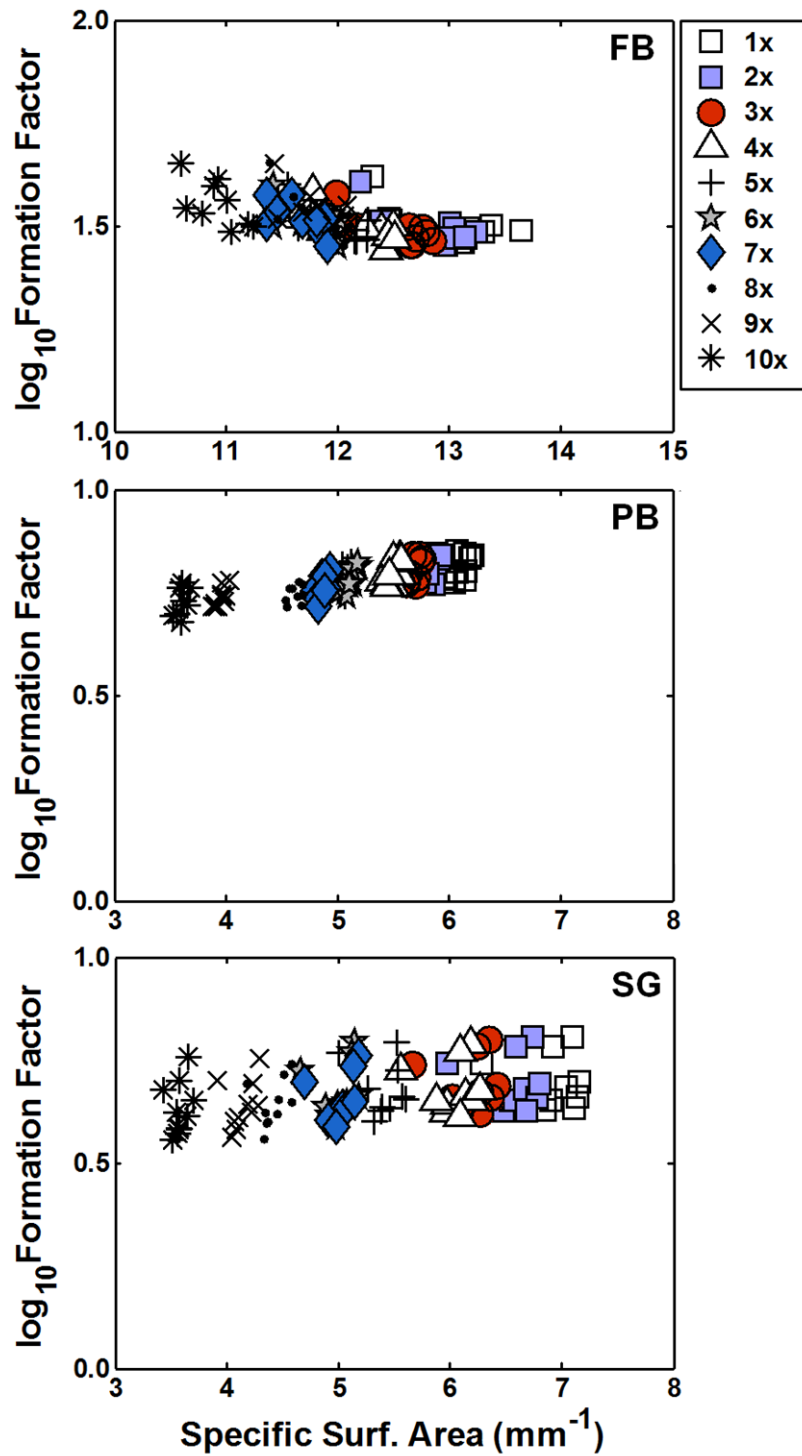
Figure 6.12.   The surface area versus formation factor as a function of resolution for all three samples.   There is a slight correspondence between the two properties; however, the change in the formation factor with surface area is fairly small.

6.6 CONCLUSION

We observe that, at least for the three samples examined here, the change in resolution have little effect on the porosity and electrical formation factor. It does affect the permeability but the change is within the scatter present in the laboratory Fontainebleau trend and the theoretical trends for Pomponio Beach and San Gregorio. Thus, it is not necessary to acquire an image with the finest technically attainable resolution. In many cases, coarser resolution is sufficient. In order to ascertain this, a workflow where one or two fine-scale images of a rock type under examination can be taken to explore how the coarsening of the images affects the desired rock properties. If the property remains within the scatter of data, then a coarser (and cheaper) imaging protocol can be implemented.

REFERENCES

Adler, P., Jacquin., C., and Quiblier, J.,1990, Flow in simulated porous media, International Journal of Multiphase Flow, 16, 691-712.

Ahmed, U., Carry, C., and Coates, G. 1991 Permeability estimation: the various sources and their interrelationships, Journal of Petroleum Technology, 43, 578-587.

Archie, G.E., 1942, The electrical resistivity log as an aid in determining some reservoir characteristics, Transactions in AIME, 146, 54-62.

Arns, C.H., Knackstedt, M.A. and Pinczewski, W.V., 2001, Accurate estimation of transport properties from microtomographic images, Geophysical research letters, 28(17), 3361-3364.

Auzerais, F. M., Dunsmuir, J., Ferreol, B.B., Martys, N., Olson, J., Ramakrishnan, T.S., Rothman, D.H., and Schwartz, L. M., 1996, Transport in sandstone: A study based on three dimensional microtomography: Geophysical. Research Letters, 23, 705–708.

Avseth, P., 2000, Combining rock physics and sedimentology for seismic reservoir characterization of North sea turbidite systems, Ph.D. dissertation, Stanford University.

Bakke, S., and Øren, P.E., 1997, 3-D pore-scale modeling of sandstones and flow simulations in the pore networks. SPE Journal 2, 136– 149.

Baptist, O.C., and Sweeney, S.A., 1954, the effect of clays on the permeability of reservoir sands to waters of different saline content, Clays and Clays Minerals, 3, 505-515.

Barber, C. B., Dobkin, D.P., and Huhdanpaa, H.T.,1996, The Quick hull Algorithm for Convex Hulls, ACM Transactions on Mathematical Software, 22, 469-483.

Bear, J, 1988, Dynamics of fluids in porous media, Dover publications, New York.

Beard, D., and Weyl, P., 1973, Influences of texture on porosity of unconsolidated sand, AAPG Bulletin, 57, 349-369.

Berg, R., 1970, Method of determining permeability from reservoir rock properties, Gulf Coast Association of Geologic Society Transactions, 20, 303-317.

Berryman, J.G. and Blair, S.C., 1986, Use of digital image analysis to estimate fluid permeability of porous materials- Application of two point correlation functions, Journal of Applied Physics, 60, 1930-1938.

Bishop, C. M., 1995, Neural networks for pattern recognition: Oxford University Press.

Bloch, S., 1991, Empirical prediction of porosity and permeability in sandstone, AAPG Bulletin, 75, 1145-1160.

Bourbie, T. and Zinszner, B., 1985, Hydraulic and acoustic properties as a function of porosity in Fontainebleau sandstone, Journal of Geophysical Research, 90, 11,524-11,532.

Carman, P., 1937, Fluid flow through granular beds, Institute of Chemical Engineering Transactions, 15, 150-166.

Chang, C., Sommerfeldt, T.G., Carefoot, J.M., and Schaalje, G.B., 1983, Relationships of electrical conductivity with total dissolved salts and cation concentration of sulfate-dominant soil extracts, Canadian Journal of Soil Science, 63, 79−86.

Chilinger, G., 1964, Relationship between porosity, permeability, and grain size distribution of sands and sandstones, in L. van Straaten, ed., Deltaic and shallow marine deposits, Elsevier, New York, 71-75.

Clesceri, L. S., Greenberg, A. E. and Eaton, A. D., 1998, Standard Methods for the Examination of Water and Wastewater, 20th ed., American Public Health Association, Washington, D.C., 2-47.

Clavier, C., Coates, G., and Dumanoir, J., 1977, The theoretical and experimental bases for the "dual water" model for interpretation of shaly sands: Ann. Mtg., Sot. Petr. Eng., SPE paper no. 6859.

Coker, D.A., Torquato, S., and Dunsmuir, J.H., 1996, Morphology and physical properties of Fontainebleau sandstone via a tomographic analysis, Journal of Geophysical Research-Solid Earth, **101**, 17497–17506.

Constantinides, G., and Payatakes, A., 1989, A three-dimensional network model for consolidated porous media. Basic studies, Chemical Engineering Communications, 81, 55-81.

Cooper, M.R., 1994, Diagenetic evolution and implications for the reservoir properties of selected shallow marine and aeolian sandstones, Ph.D. Dissertation, University of Liverpool, UK, 184.

Cundall, P. A. and Strack, O. D. L., 1979, A discrete numerical model for granular assemblies: Geotechnique, 29, 47–65.

Doyen,P., 1988; Permeability, conductivity and pore geometry of sandstone, Journal of Geophysical Research, 93, 7729-7740.

Dullien, F., 1979, Porous media, fluid transport and pore structure, Academic Press, New York, 42-65.

Dunsmuir, J.H., Ferguson, S.R., D'Amico, K.L. and Stokes, J.P., 1991, X-ray Micro Tomography. A New Tool for the Characterization of Porous Media, SPE 22860, Proceedings of the 1991 SPE Annual Technical Conference and Exhibition (1991).

Dvorkin, J., 2009, Digital rock physics bridges scales of measurement, Hart's E & P, 82, 9, 31-35.

Dvorkin, J., and Nur, A., 2009, Scale of experiment and rock physics trends, The Leading Edge, 28, 110-115.

Dvorkin, J., Derzhi, N., Fang, Q., Nur, A., Nur, B., Grader, A., Baldwin, C., Tono, H., and Diaz, E., 2009, From micro to reservoir scale: Permeability from digital experiments, The Leading Edge, 28, 1446-1453.

Frost, V.S., Stiles, J.A., Shanmugam, K.S., Holtzman, J.C., and Smith, S.A., 1981, An adaptive filter for smoothing noisy radar images, Proceedings of IEEE, 69, 133-136.

Galehouse, J., 1971. Point counting. In: Carver, R. (Ed.), Procedures in Sedimentary Petrology. Wiley Interscience, New York.

Gomez, C., 2009, Reservoir characterization combining elastic velocities and electrical resistivity measurements, Ph.D. Dissertation, Stanford University.

Gonzalez, R.C. and Woods, R.E., 1992, Digital image processing: Addison-Wesley Publication.

Haddad, S.C., Worden, R.H., Prior, D., J., And Smalley, P.C., 2006, Journal of sedimentary research, 76, 244-256.

Halley, R.B., 1978, Estimating pore and cement volume in thin section, Journal of Sedimentary Research, 48, 642-650.

Hastie, T., 2001, The elements of statistical learning: data mining, inference, and prediction, Springer.

Hem, J. D., 1985, Study and Interpretation of the Chemical Characteristics of Natural Water, 3rd ed., U.S. Geological Survey Water-Supply Paper 2254, 64-65.

Iverson, W., and Satchwell, R., 1989, Permeability: an elusive goal of production geophysics, Society of Exploration Geophysicist International Meeting: Expanded Technical Program Abstracts and Biographies, 1, 576-598.

Jain, A.K., 1989, Fundamentals of digital image processing: Prentice-Hall International

Jin, G., Patzek, P.W., and Silin, D.B., 2004, Direct Prediction of the Absolute Permeability of Unconsolidated and Consolidated Reservoir Rock, SPE paper 90084.

Johnson, D., Koplik, J., snad Dashen, R., 1987, Theory of dynamic permeability and tortuosity in fluid-saturated porous media, Journal of Fluid Mechanics, 176, 379-402.

Kameda, A., 2005, Permeability evolution in sandstone: Digital rock approach, Ph.D. Dissertation, Stanford University.

Kameda, A., Dvorkin, J., Keehm, Y., Nur, A., and Bosl, B., 2006, Permeability-porosity transforms from small sandstone fragments, Geophysics, 71, 11-19.

Katz, A., and Thompson, A., 1986, Quantitative prediction of permeability in porous rock, Physical Review B, 34, 8179-8181.

Keehm, Y., 2003, Computational rock physics: Transport properties in porous media and applications, Ph.D. Dissertation, Stanford University.

Keller, G.V., 1966, In Handbook of Physical Constants, Geological Society of America Memoir 97, Washington D.C., 533-577

Keller, G. V. and Frischknecht, F. C., 1966, Electrical Methods in Geophysical Prospecting, Pergamon Press, Oxford, 31-32.

Ketcham, R.A. and Carlson, W.D., 2001, Acquisition, optimization and interpretation of X-ray computed tomographic imagery: Applications to the geosciences, Computers and Geosciences, 27, 381-400.

Kong, M. , Bhattacharya, R.N., James, C., and Basu, A., 2005, A statistical approach to estimate the 3D size distribution of spheres from 2D size distributions, GSA Bulletin, 117, 244-299.

Koplik, J., Lin, C. and Vermette, M., 1984, Conductivity and permeability from microgeometry: Journal of Applied Physics, 56, 3127-3131.

Krumbein, W. and Monk, G., 1942, Permeability as a function of the size parameters of unconsolidated sands, AIME Petroleum Transactions, 151, 153-163

Krzanowski, W.J., 1988, Principles of multivariate analysis: a user's perspective, Oxford University Press.

Kuan, D.T., Alexander, A.S., Timothy, C.S. and Chavel, P., 1987, Adaptive restoration of images with speckle, IEEE Transactions on Acoustic, Speech and Signal Processing, ASSP-35, 373-383.

Livingood, P.C. and Cordell, A.S., 2009, Point counter point: the accuracy and feasibility of digital image techniques in the analysis of ceramic thin sections, Journal of Archaeological Science, 36, 867-872.

Marion, A., 1991, An Introduction to Image Processing, Chapman and Hall, London, 274.

Marion, D., Nur, A., and Alabert, F,. 1989, Modelling the relationships between sonic velocity, porosity, permeability and shaliness in sand, shale and shaly sand, SPWLA Thirtieth Annual Logging Symposium Proceedings, paper G, 1-22.

Martys, N.S. and Garboczi, E.J., 1992, Length scales relating the fluid permeability and electrical conductivity in random two-dimensional model porous media: Physical Review B, 46, 6080-6090.

Matthess, G., 1982, The Properties of Groundwater, John Wiley & Sons, New York, 71-72.

McCresh, C., Etris, E., Brumfield, D., and Ehrlich, R., 1988, Relating thin sections to permeability, mercury porosimetry, formation factor and tortuosity, AAPG Bulletin, 72, 221-222.

O'Connor, R. M., and Friedrich, J., 1999, Microscale flow modeling in geologic materials, Physics and Chemistry of Earth, 24, 611–616.

O'Rourke, J., 1994, Computational Geometry in C, Cambridge University Press, Cambridge, England.

Otsu, N., 1979, A threshold selection method from gray level histograms, IEEE Transactions on Systems, Man and Cybernetics, SMC-9, 62-66.

Payatakes, A., Tien, C., and Turian, R., 1973, A new model for granular porous media : part I. Model formulation, AIChE Journal, 19, 58-67.

Prager, S., 1961; Viscous flow through media, The Physics of Fluids, 4, 1477-1482.

Revil, A., and Glover, P.W.J., 1998, Nature of surface electrical conductivity in natural sands, sandstones, and clays, Geophysical Research Letter, 25, 691-694.

Riddler, T.W. and Calvard, S., 1978, Picture thresholding using an iterative selection method, IEEE Transactions on Systems, Man and Cybernetics, SMC-8, 630-632.

Rojas, R., 1996, Neural network – A systematic introduction, Springer-Verlag, Berlin, New-York.

Rosenfeld, A. and Torre, P., 1983, Histogram concavity analysis as an aid in threshold selection, IEEE Transactions on Systems, Man and Cybernetics, SMC-13, 231-235.

Rubinstein, J., and Torquato, S., 1989;Flow in random porous media: mathematical formulation, variational principles and rigorous bounds, Journal of Fluid Mechanics, 206, 25-46.

Schwartz, L., and Banvar, J. 1989, Transport properties of disordered continuum systems, Physics Review B, 39, 11965-11970.

Seber, G.A.F., 1984, Multivariate Observations, Wiley.

Sen, P. N., and Goode, P. A., 1988, Shaly sand conductivity at low and high salinities, Paper F, TRANS. 29th Annual Symposium of Society of Professional Well Log Analysts.

Sheng, P., and Zhou, M.Y., 1988; Dynamic permeability in porous media, Physical Review Letters, 61, 1591-1594.

Solomon, M., 1963, Counting and sampling errors in modal analysis by point counter, Journal of Petrology, 4, 367-382.

Sorensen, J. A. and Glass, G. E., 1987, 'Ion and temperature dependence of electrical conductance for natural waters', Analytical Chemistry, 59, 1594−1597.

Spanne, P., Thovert, J.F., Jacquin, C.J., Lindquist, W.B., Jones, K.W. and Adler, P.M., 1994, Synchrotron computed microtomography of porous-media-topology and transports, Physics Review Letter, **73**,. 2001–2004.

Sudha, S., Suresh, G.R., and Sukanesh, R., 2009, Comparative study on speckle noise suppression techniques for ultrasound images, International Journal of Engineering and Technology, 1, 57-62.

Swanson, B., 1981, A simple correlation between permeabilities and mercury capillary pressures, Journal of Petroleum Technology, 33, 2498-2504.

Thiry, M., Bertrand-Aryault, M. and Grisoni, J.C., 1988, Ground water silicification and leaching in sands: Example of the Fontainebleau Sand (Oligocene) in the Paris Basin, Geological Society of America Bulletin, 100, 1283–1290.

Thomeer,J., 1983, Air permeability as a function of three pore network parameters, Journal of Petroleum Technology, 35, 809-814.

van Baaren, J., 1979, Quick look permeability estimates using sidewall samples and porosity logs, SPWLA Sixth European Symposium Transactions, 1-10.

Van der Plas, L. and Tobi, A.C., 1965, A chart for judging the reliability of point counting results, American Journal of Science, 263, 87-90.

Waxman. M. H.. and Smits. L. J. M.. 1968. Electrical conduction in oil bearing shaly sands, Society. Petroleum Enggineering. J., 8, 107-122.

Wernert, V., Bouchet, R. and Denoyel, R., 2010 Influence of Molecule Size on Its Transport Properties through a Porous Medium, Analytical Chemistry, 82, 2668-2679.